

Study of photophysical processes in organic light-emitting diodes based on light-emission profile reconstruction

Citation for published version (APA):

Carvelli, M. (2012). *Study of photophysical processes in organic light-emitting diodes based on light-emission profile reconstruction*. [Phd Thesis 1 (Research TU/e / Graduation TU/e), Applied Physics and Science Education]. Technische Universiteit Eindhoven. <https://doi.org/10.6100/IR724532>

DOI:

[10.6100/IR724532](https://doi.org/10.6100/IR724532)

Document status and date:

Published: 01/01/2012

Document Version:

Publisher's PDF, also known as Version of Record (includes final page, issue and volume numbers)

Please check the document version of this publication:

- A submitted manuscript is the version of the article upon submission and before peer-review. There can be important differences between the submitted version and the official published version of record. People interested in the research are advised to contact the author for the final version of the publication, or visit the DOI to the publisher's website.
- The final author version and the galley proof are versions of the publication after peer review.
- The final published version features the final layout of the paper including the volume, issue and page numbers.

[Link to publication](#)

General rights

Copyright and moral rights for the publications made accessible in the public portal are retained by the authors and/or other copyright owners and it is a condition of accessing publications that users recognise and abide by the legal requirements associated with these rights.

- Users may download and print one copy of any publication from the public portal for the purpose of private study or research.
- You may not further distribute the material or use it for any profit-making activity or commercial gain
- You may freely distribute the URL identifying the publication in the public portal.

If the publication is distributed under the terms of Article 25fa of the Dutch Copyright Act, indicated by the "Taverne" license above, please follow below link for the End User Agreement:

www.tue.nl/taverne

Take down policy

If you believe that this document breaches copyright please contact us at:

openaccess@tue.nl

providing details and we will investigate your claim.

Study of photophysical processes in organic light-emitting diodes based on light-emission profile reconstruction

PROEFSCHRIFT

ter verkrijging van de graad van doctor aan de
Technische Universiteit Eindhoven, op gezag van de
rector magnificus, prof.dr.ir. C.J. van Duijn, voor een
commissie aangewezen door het College voor
Promoties in het openbaar te verdedigen
op donderdag 9 februari 2012 om 16.00 uur

door

Marco Carvelli

geboren te Rho (MI), Italië

Dit proefschrift is goedgekeurd door de promotoren:

prof.dr. R. Coehoorn

en

prof.dr.ir. R.A.J. Janssen

Cover design: M. Carvelli, C. Sallustro (www.sallustrodesign.com)
and N. Debernardi (www.dobermaniprod.biz)

Printed by: Universiteitsdrukkerij Technische Universiteit Eindhoven.

A catalogue record is available from the Eindhoven University of Technology Library.
ISBN: 978-90-386-3086-1



This research forms part of the research programme of the Dutch Polymer Institute (DPI), project #518.

Copyright © 2012, M. Carvelli.

Preface

In the past five years, organic light-emitting diodes (OLEDs) have emerged as a promising option for energy-efficient, flexible light sources. Luminous efficacies of more than 60 lm/W, already exceeding the efficiency of compact fluorescent (“energy-saving”) lamps, are obtained to date using multilayer structures of evaporation-deposited small-molecule organic semiconductors. Flexible OLEDs are presently usually based on a single active polymer layer deposited by spin-coating or ink-jet printing. Within both technologies, a key factor that needs to be measured and controlled is the shape of the emission profile, i.e. the spatial distribution of the emitting excitons across the active layer thickness. Being able to accurately measure the emission profile makes it possible to understand the fundamental (photo)physical processes involved in the device operation, providing a basis for further improving the efficiency. In order to investigate state-of-the-art devices, containing 10-20 nm thick emitting layers, emission profile measurements should provide nanometer-scale resolution.

In this thesis we present a method which, for the first time, makes it possible to reconstruct the light-emission profile with a nanometer-scale resolution. We first demonstrate the potential of the approach on single-layer monochrome devices. Subsequently, a detailed analysis is provided which indicates that the method may also be applied to multilayer devices, while keeping the resolution in the 1-10 nm range.

Three applications of the light-emission profile reconstruction method are presented. First, the method is used to determine the singlet exciton fraction in OLEDs. From standard statistical physics considerations a value of 25% is expected. Since in fluorescent materials only singlet excitons can decay radiatively, this fraction limits the maximum achievable efficiency of fluorescent OLEDs. In recent years several studies have indicated that deviations from this value may occur, in particular for polymers. The development of an accurate method for determining the singlet exciton fraction has thus become a topic of intensive discussion and great interest in the literature. We have extended a method presented by Segal *et al.* (2003) by exploiting the possibility to reconstruct the light-emission profile in OLEDs, and show that for the specific case of intensively studied polyfluorene-based copolymers and for a polyphenylene-vinylene-based

polymer the singlet fraction is only 8 – 25%. From our studies we could then conclude that the maximum attainable internal quantum efficiency of polymer OLEDs based on the materials analyzed is thus severely limited by the unfavorable spin-statistics of the exciton formation process.

A second application involves the study of the emission profile in more complex double-layer small-molecule-based fluorescent OLEDs. In this case we show that the method provides novel insights in the photophysical processes near organic-organic interfaces. Increasing the thickness of one of the two layers is found to give rise to an emission profile shift from one side of the interface to the other, and to the occurrence of charge-transfer exciton emission. A delicate balance is shown to govern the exciton emission at both sides of the interface and the charge-transfer exciton emission from the interface itself. Since the corresponding three emission spectra are different, controlling the light-emission profile by varying one of the layer thicknesses results in the possibility to tune the emission color.

As a final application, an analysis is presented of the emission profile in a multilayer white-emitting OLED, investigated within the framework of the European project AEVIOM. The light-emission profile obtained provides a measure of the balance between the generation of excitons in the three emissive layers (red, green and blue). It furthermore enables making an accurate assessment of the validity of the charge transport and recombination models developed in the project, and it is shown to provide deeper insight in the exciton diffusion physics through the emissive layers.

The method presented in this thesis is expected to be a fundamental tool for the experimental validation of device models and for designing OLEDs with increased efficiency. The results presented are not only important for OLEDs, but can also be applied to other organic light-emitting devices, such as light-emitting electrochemical cells and light-emitting field-effect transistors. A detailed analysis about future research directions enabled by our method is presented in the outlook chapter of this thesis.

Marco Carvelli, Eindhoven, December 2011

A Tiziana e Francesco

Contents

1	Introduction	1
1.1	Organic light-emitting diodes for lighting	1
1.2	External quantum efficiency and luminous efficacy	5
1.3	State-of-the-art OLED structures	9
1.4	Scope of this thesis	14
1.5	References	17
2	Light-emission profile reconstruction method	19
2.1	Introduction	20
2.2	Solving the inverse outcoupling problem	21
2.3	Emission profiles for PF-TAA and NRS-PPV based OLEDs	25
2.4	Internal consistency and accuracy limits	26
2.5	Conclusions	29
2.6	Appendix A	30
2.7	Appendix B	31
2.8	References	38
3	Spatial resolution	41
3.1	Introduction	42
3.2	Theoretical methods	43
3.3	Spatial resolution - four case studies	46
3.3.1	Emission at one interface: delta-function shaped profile	46
3.3.2	Broad emission profile	48
3.3.3	Emission at two interfaces	50
3.3.4	Uniform emission in between two interfaces: rectangular profile	51
3.4	Conclusions	53
3.5	Appendix	54
3.6	References	58

4	Determination of the exciton singlet : triplet ratio	61
4.1	Determination of the exciton singlet : triplet ratio	62
4.2	Light-emitting polymer and experimental methods	65
4.3	Experimental results and analysis	67
4.4	Discussion - PF-7.5%TAA	69
4.5	Polyfluorene-based devices with 0.5 mol% copolymerized TAA	74
4.6	Poly(phenylene vinylene)-based devices	79
4.7	Conclusions	85
4.8	References	87
5	Light emission near organic-organic interfaces	91
5.1	Introduction	92
5.2	Energy level structure, optical properties and emission color	95
5.2.1	Molecular energy levels and orbital shape	95
5.2.2	Time-resolved photoluminescence measurements	96
5.2.3	Current density and color-point variation with BA1q layer thickness	97
5.3	Light-emission profiles and external quantum efficiency	100
5.3.1	Method	100
5.3.2	Reconstructed light-emission profiles	101
5.3.3	External quantum efficiency	104
5.4	Comparison with results from a charge recombination model	105
5.5	Conclusions	111
5.6	Appendix A	113
5.7	Appendix B	114
5.8	References	115
6	Hybrid white-light emitting OLEDs	117
6.1	Introduction	117
6.2	Emission color point and external quantum efficiency	121
6.3	Light-emission profile reconstruction	122
6.4	Conclusions	128
6.5	Appendix A	129
6.6	Appendix B	130
6.7	References	131
7	Outlook	133
7.1	Introduction	133
7.2	Experimental validation of electron-hole recombination models	134
7.3	Sandwich-type light-emitting electrochemical cells	135
7.4	High-efficiency organic light-emitting transistors	137
7.5	Towards electrically-pumped organic organic laser diodes	139
7.6	Conclusions	140
7.7	References	141
	Summary	142

Samenvatting	145
List of publications	147
Curriculum vitae	148
Acknowledgements	150

1

Introduction

Light generation in organic light-emitting diodes (OLEDs) is due to the recombination of electrons and holes within amorphous organic layers. Being able to measure with high accuracy the light generation profile within OLEDs would provide essential information concerning the charge transport physics, recombination physics and photophysics of OLEDs. Such a method was so far missing in the field. The development and application of this tool is the main subject of this thesis. The first part of this chapter aims at introducing the fundamentals of OLED device physics, with a particular focus on state-of-the-art stack design strategies for fabricating efficient white emitting OLEDs. The second part of the chapter introduces the light-emission profile reconstruction method which will be developed and applied throughout the thesis, with a focus on the photophysical information that such a method could in principle provide, and contains an overview of the scope of the thesis.

1.1 Organic light-emitting diodes for lighting

Starting with the development of the first thin-film heterojunction diodes based on organic small-molecules and polymeric materials in the late 1980s and early 1990s,^{1,2} Organic Light Emitting Diode (OLED) technology has presently grown to the level of having the first commercial products available on the market, both for lighting and for display applications.

OLEDs basically consist of an organic semiconductor placed between electrodes. By applying a voltage between the electrodes, electrons and holes are injected into the organic semiconductor, where they will meet. As a result of radiative recombination light is generated. In figure 1.1 the schematic structure of a state-of-the-art multilayer small-molecule OLED is presented (a), together with the associated energy diagram (b). When the applied bias voltage approaches the built-in voltage (defined as the difference between the anode and cathode work functions), holes and electrons are injected from the anode and the cathode,

respectively. A series of injection and transport layers assures that the charge carriers are transported from the electrodes to the emitting layers (EML in the figure) with low energy losses. Electron (hole) blocking layers are present to prevent electrons (holes) from escaping the central emitting region of the device. The energy diagram in figure 1.1(b) helps to understand the picture just sketched.

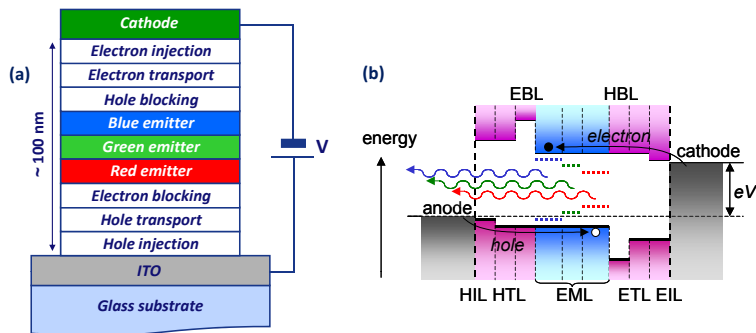


Figure 1.1: (a) Schematic structure of a state-of-the-art multilayer small molecule OLED and (b) schematic energy diagram indicating the energy level of the hole-injection layer (HIL), hole-transport layer (HTL), electron-blocking layer (EBL), red, green and blue emitting layers (EML), hole-blocking layer (HBL), electron-transport layer (ETL) and electron-injection layer (EIL)

It has been drawn at so-called flat-band condition, i.e. when the minimum voltage is applied in order to have carrier drift through the device. If carriers had to be injected directly into the central emitting region a large energy barrier must in general be overcome, leading to inefficient charge injection. The use of charge injection and transport layers (ETL, EIL, HTL, HIL in the figure) decreases the energy barrier and thus facilitates charge injection and transport from the electrodes to the EML region. Blocking layers surround the EML region and prevent charges from escaping the emitting layers, due to the high energy barrier to be overcome. The central emitting region is generally composed of several layers. In the case of white light emitting devices, as those employed for lighting applications, typically two or three emitting layers are present: white light can be obtained as a combination of blue and yellow emission (two layers) or red, blue and green emission (three layers). In practice, each emitting layer is generally composed of an organic matrix doped with a luminescent organic guest. The use of host-guest systems makes it possible to separately optimize the charge transport/injection properties and the photophysical properties of the layer. After recombination, bound excited states are generated, called excitons. Excitons will quickly be transferred to guest molecules, which are characterized by a lower energy gap compared to the matrix molecules. The guest is chosen for its photophysical properties, e.g. the emission spectrum and the radiative decay quantum efficiency. The use of guest emitting species dispersed in a host matrix also allows one to reduce the chance of exciton-exciton quenching, compared to a layer composed of purely the guest molecules. Each exciton has a finite probability

to relax to the ground state via photon emission. By tuning the exciton population within the different emitting layers, the emission color can be adjusted to vary from warm white (with a relatively large red spectral component) to cold white (with a relatively large blue spectral component).

Given the growing demand for energy worldwide and the slow deployment of renewable energy sources, it is imperative to exploit the available energy sources in the most efficient way. General illumination requires $\simeq 19\%$ of the total electricity consumption,³ which is why in recent years a large attention has been paid to the development of high-efficiency lamps to substitute the common low-efficiency incandescent light bulbs. Within this framework light emitting diodes (both organic and inorganic) are a valuable candidate for next-generation lighting, due to their high efficiency. In figure 1.2 the progress of the energy efficiency of white organic and inorganic LEDs is presented, as compared to commercial incandescent and tubular fluorescent lamps. Compact fluorescent lamps (“energy saving” lamps), CFL, have typically an energy efficiency of 60 lm/W. The energy efficiency is expressed as luminous efficacy, in lumen per Watt [lm/W], described in detail in the next section. As may be noticed, OLEDs are approaching the efficiency of fluorescent lamps. The full circles refer to laboratory results, not commercially available. The three highest data-points refer to results from: Konica Minolta, 64 lm/W OLEDs with a lifetime of 10000 hours at 1000 cd/m²⁴; Universal Display Technology (UDC), 102 lm/W OLEDs at 1000 cd/m², no information on the lifetime available⁵; Institut für Angewandte Photophysik (IAPP), Technische Universität Dresden, 124 lm/W OLEDs with a lifetime of 1-2 hours at 1000 cd/m².⁶ The lifetime is defined as the time at which the emission at a constant voltage drops to half of the initial light intensity. In the device from Konica Minolta an optical outcoupling foil was employed to enhance the light outcoupling. In the latter two examples optical macroextractors (i.e. glass hemisphere or patterned glass surface) are used for the same purpose. Light outcoupling foils are suitable for large area sources, while macroextractors are not. The empty circles refer to commercially available OLEDs for lighting applications. The lowest data point refers to the first OLED for lighting ever commercialized, while the highest refers to the most efficient OLED for lighting commercialized at the moment this thesis was written. They are produced by Royal Philips Electronics⁷ and the highest value, result of a partnership between Philips and Konica Minolta,⁴ refers to a 45 lm/W OLED with a lifetime of 10000 hours at 1000 cd/m². Other OLED manufacturers presently commercializing the first products for lighting include Osram, Lumiotec and Kaneka. The empty stars on the graph refer to declared target efficiencies as presented by Universal Display Technology.⁵

Although the efficiency of organic LEDs lags behind that of inorganic LEDs, the two technologies can be exploited for complementary applications. While LEDs are seen as a preferred technology for high brightness, point-like light sources, OLEDs represent a revolutionary light source that allows for unprecedented applications, such as transparent and flexible light-emitting “plastic” foils. The first OLED for lighting applications have been made available from Philips in 2009 under the commercial name Lumiblade.⁷ In figure 1.3(a) an example of a Philips Lumiblade OLED is shown, together with a flexible prototype OLED.

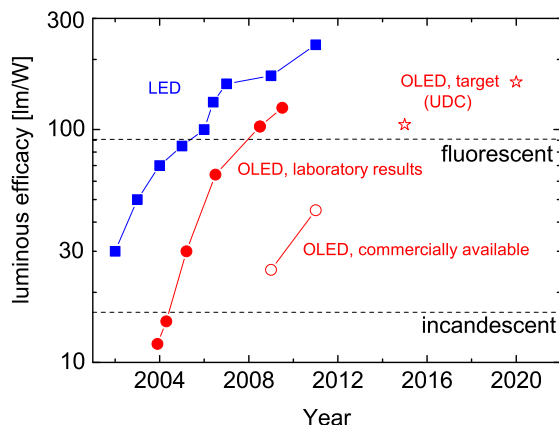


Figure 1.2: Progress of the luminous efficacy of white organic (red symbols) and inorganic (full blue squares) LEDs as compared to commercial incandescent and fluorescent light sources (dashed lines). Full circles refer to laboratory results for OLEDs, as specified in part in the main text, not commercially available. Empty circles refer to commercially available OLEDs for lighting. The lowest data point refers to the first OLED for lighting ever commercialized, while the highest refers to the most efficient⁷ OLED for lighting commercialized at the moment this thesis was written. Empty stars refer to declared target efficiencies from Universal Display Corporation.⁵

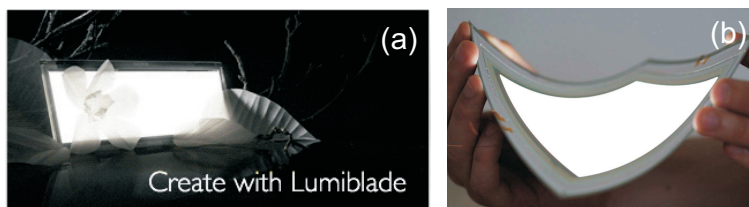


Figure 1.3: (a) Philips Lumiblade OLED, www.lumiblade.com, (b) Flexible white OLED (source: HolstCentre)

1.2 External quantum efficiency and luminous efficacy

The external quantum efficiency (EQE, η_{EQE}) of OLEDs is defined as the ratio between the number of photons observed in air from the device surface (emitted per m^2 and per second) and the number of charges injected per m^2 and per second. For a fluorescent device the EQE is given by a product of four factors:

$$\eta_{\text{EQE}} = \eta_{\text{rec}} \cdot \eta_{\text{S}} \cdot \eta_{\text{rad}} \cdot \eta_{\text{out}}, \quad (1.1)$$

where η_{rec} is the electron-hole recombination efficiency, η_{S} is the exciton singlet fraction, η_{rad} is the radiative decay probability and η_{out} is the light outcoupling efficiency. The product $\eta_{\text{rec}} \cdot \eta_{\text{S}} \cdot \eta_{\text{rad}}$ is defined as the internal quantum efficiency (IQE). Let us analyze each of these terms separately.

After electrons and holes are injected they are driven towards opposite electrodes by the applied electric field and have a finite chance to meet each other. One can define as electron-hole recombination efficiency the probability that opposite carriers will recombine before reaching the opposite electrode, thus being lost. In a simple OLED stack composed of an organic emitting layer sandwiched between electrodes, the recombination efficiency is mainly determined by the injection conditions from the electrodes. In the absence of injection barriers, charge diffusion from the electrodes into the organic layer will assure that all charges will eventually recombine before reaching the opposite electrode. In the presence of large injection barriers, the region close to the electrodes is scarcely filled with diffused carriers, thus the chances for a charge to reach the opposite electrode without recombining increase. In multilayer devices in practice the use of charge blocking layers (described in the previous section) allows one to have 100% recombination efficiency, even in presence of injection barriers.

Once an exciton is generated, in a fluorescent material only singlet excitons can radiatively decay to the ground state, being characterized by a zero net magnetic moment, while radiative decay for triplets is spin-forbidden. Standard statistical considerations⁸ predict a singlet fraction (defined as the number of singlet excitons over the total number of generated excitons) of 25%. In recent years, several experimental studies have indicated that the singlet exciton formation yield in OLEDs can significantly exceed the quantum statistical value of 25%, in particular for polymers.^{9–18} However, the issue of the singlet fraction in polymers is still a matter of debate, based on experimental results showing that it is only around 20% for the archetype poly(phenylene vinylene) (PPV)-based polymer MEH-PPV,¹⁵ on more general considerations of the observed external quantum efficiency of fluorescent polymer OLEDs,¹⁵ and on an experimental study which suggests that in a relevant polymer no singlet-triplet interconversion takes place in the exciton precursor (bound polaron pair) states.¹⁹ The occurrence of such interconversion processes is regarded as a crucial condition for obtaining an enhanced singlet fraction.^{20–23} In phosphorescent materials the high spin-orbit interaction gives rise to quantum-mechanical mixing of singlet and triplet states, leading to a finite

probability to have radiative decay also from states which are predominantly of triplet character. Examples of phosphorescent molecules typically employed as green and red emitters in state-of-the-art OLEDs are shown in figure 1.4. The presence of a heavy transition metal atom (iridium) enhances the spin-orbit interaction. In the same figure an example of a fluorescent blue emitting molecule, 4P-NPD, is also given.

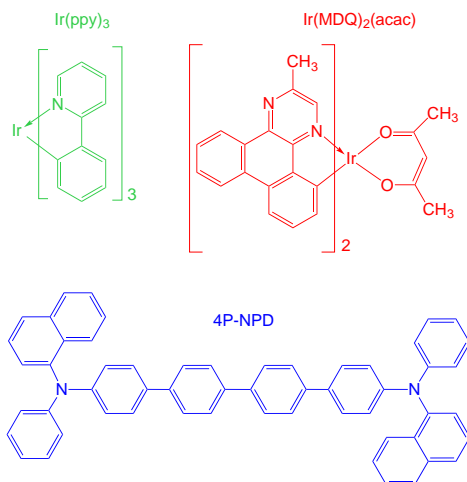


Figure 1.4: Examples of green and red phosphorescent emitters and a blue fluorescent emitter typically used in OLEDs. The molecule names refer to fac-tris(2-phenylpyridine) iridium, $\text{Ir}(\text{ppy})_3$, (acetylacetonate)bis(2-methyldibenzo[f,h]quinoxinalate)iridium, $\text{Ir}(\text{MDQ})_2(\text{acac})$, and N,N'-di-1-naphthalenyl-N,N'-diphenyl-[1,1':4',1'':4'',1''':4''']-4,4'''-diamine, 4P-NPD.

In principle, for a full-phosphorescent OLED the internal quantum efficiency can therefore be equal to 100%, if $\eta_{\text{rad}} = 1$. In practice, even if radiative decay is allowed, the exciton relaxation to the ground state is characterized by the competition between radiative decay and non-radiative decay channels, such as thermal relaxation. This implies that the radiative decay probability η_{rad} is finite. The radiative decay probability is often assumed to be equal to the photoluminescence quantum yield as measured in a thin film, i.e. the ratio between the number of emitted photons and the number of absorbed photons in a photoluminescence experiment. However, it should be noticed that the radiative decay probability is enhanced in case an exciton is generated within a microcavity.^{24,25} Optical models have been developed to properly take this effect into account.²⁶ Excitons are thus characterized by a specific lifetime before they relax to ground state. Typical lifetime values are on the order of nanoseconds for singlets and microseconds for triplets in Ir-based phosphorescent emitters. Before decaying to the ground state excitons can diffuse within the emitting layer. Typical diffusion lengths are on the order of 5-10 nm for singlets.²⁷ Triplet exciton diffusion lengths as large as ~ 87 nm have been demonstrated,²⁸ e.g. for α -NPD. Exciton

diffusion occurs via two mechanisms: Förster energy transfer and Dexter energy transfer.⁸ The former involves energy exchange between oscillating dipoles and it is characterized by a rate which decays over the distance, R , between dipoles as R^{-6} . The latter involves the exchange of electrons between adjacent molecules and requires molecular overlap between the orbitals of the interacting molecules; its strength decays over distance as $\exp(-\beta R)$, where β is the relevant inverse wavefunction decay length. In multilayer OLEDs, due to exciton diffusion there is a finite chance that excitons are converted into less energetic species, such as charge-transfer (CT) states or exciplexes at organic-organic interfaces, or such as lower energy excitons within neighboring layers. CT states (or exciplexes) are defined as states where electrons and holes reside on two distinct molecules of different type. When the nature of the complex is mainly ionic this is called a charge-transfer state, while it is called an exciplex when its nature is mainly covalent.²⁹ They are usually characterized by a lower energy and longer lifetime. Light emission from a double-layer OLED can thus in general originate from a superposition of the pure exciton emission from the bulk of the layers at both sides of the interface and emission from CT states. The balance of these three components can strongly affect the device efficiency and emission spectrum. A second consequence of exciton diffusion is the possibility for excitons to meet each other and annihilate (a process known as exciton-exciton quenching) or to meet a charge and annihilate (exciton-polaron quenching). Due to the above mentioned processes, one should make a distinction between the electron-hole pair formation profile, which is the spatial exciton distribution as they are generated, and the light-emission profile, which describes the spatial distribution of the excitons at the moment of radiative recombination.

Once a photon is generated, the probability of observing it outside the device, i.e. without being absorbed or waveguided to the device edges, is defined as the light-outcoupling efficiency, η_{out} . For OLEDs a typical value for the outcoupling efficiency is 20%. In order to enhance the light-outcoupling efficiency, two strategies are typically implemented⁶: (i) a high refractive index, rough, patterned scattering substrate (extractor) is used to enhance the extraction of microcavity modes which would otherwise be waveguided, and (ii) a properly chosen electron transport layer thickness may be employed which acts as a spacer from the light-quenching cathode. It is of interested to consider an example, in figure 1.5, where the microcavity effect on the outcoupled light in OLEDs is elucidated.

A simple layer stack is assumed: glass (1 mm) / anode (indium tin oxide, 120 nm) / organic emitting layer (Alq_3) / cathode (aluminum, 100 nm). No assumption is made on the dipole characteristic (“source”) emission spectrum, i.e. a flat emission spectrum is assumed in the visible range. In figure 1.5(a) the normalized outcoupled light intensity as a function of the distance of the dipole from the cathode is presented. The assumed thickness of the organic layer is 100 nm in this case. Light is clearly optimally outcoupled at a distance of approximately 60 nm from the metallic cathode. In figure 1.5(b) a similar analysis is performed for emission at two distinct wavelength values, 450 nm (blue) and 600 nm (red), for a 200 nm-thick device. In this case the presence of a second outcoupling maximum can be observed for emission at 450 nm, as well as phase

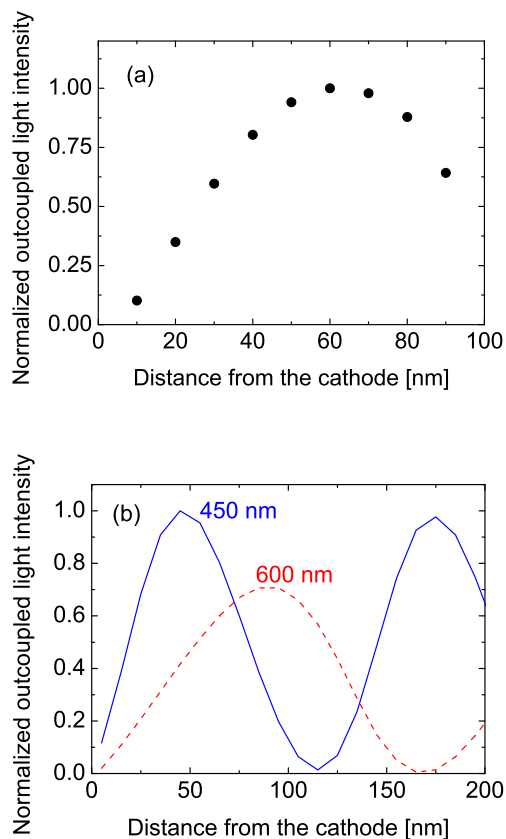


Figure 1.5: (a) Normalized outcoupled light intensity as a function of the position of the exciton within the organic layer. (b) Normalized outcoupled light as a function of the position of the dipole within the organic layer, for two different emission wavelengths, 450 nm (blue, solid line) and 600 nm (red, dashed line). In both cases a flat “source” emission spectrum is assumed.

shift of the position for optimal outcoupling at 600 nm compared to 450 nm. As a consequence, for white-emitting OLEDs the blue emitting layer is often positioned closer to the cathode compared to the red one, to ensure good light-outcoupling efficiency at both wavelength-ranges. Such a strong microcavity effect leads to a strong dipole-position dependence of the calculated emission spectra as a function of the wavelength, angle and polarization (examples of that will be given throughout the thesis). This is a crucial ingredient which allowed us to reconstruct the light-emission profile with nanometer-scale resolution.

Within the lighting community, the efficiency of a light-emitting device is expressed in terms of luminous efficacy [lm/W], i.e. the luminous flux per unit of electrical power. The luminous flux, expressed in the unit lumen [lm], is the amount of visible light emitted by a source per second, taken the wavelength-dependence of the eye-sensitivity into account (shown in figure 1.6). Green emission centered at 555.17 nm is best detected by the human eye. The maximum efficiency for a source at this wavelength would be 683 lm/W . For white light, it can be at best $\sim 350 \text{ lm/W}$.

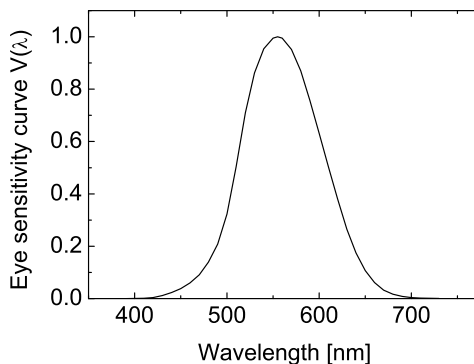


Figure 1.6: Photopic eye sensitivity as a function of the wavelength emitted by a source.

1.3 State-of-the-art OLED structures

Analyzing the different factors which determine the OLED efficiency, the main challenges for developing power-efficient light sources can be summarized as follows⁶: the internal electroluminescence quantum efficiency must be close to one (high internal quantum efficiency), a high fraction of the internally created photons must escape to the forward hemisphere (high outcoupling efficiency) and the energy loss before electron-photon conversion should be small (low operating voltage). Hereafter a brief overview is presented of state-of-the-art device architectures, selected from the recent literature, aiming at addressing the three challenges mentioned. A full description of the materials employed in each stack can be found in the studies from which the examples are taken; here we will solely discuss the role of each layer within the device stack. In all cases, a combination of red, green and blue emitters is exploited in order to generate white-light emission. As already mentioned, a combination of blue and yellow emitters can also be exploited to generate white light. However, this kind of layer stack is characterized by an intrinsically lower white-light quality (color rendering index). The color

rendering index (CRI) is the “effect of an illuminant on the color appearance of objects by conscious or subconscious comparison with their color appearance under a reference illuminant”.³⁰ It is a quantitative measure of the ability of a light source to reproduce the colors of various objects faithfully in comparison with an ideal or natural light source. The reference emitter is a black body radiator at a temperature which corresponds to the color temperature of the light source. The color point can be calculated giving a proper weight³⁰ of the spectral components in the emission and it is defined by two coordinates in the CIE chromaticity diagram shown below, as defined by the *Commission internationale de l’Eclairage*³⁰ in 1931. Two sources can be characterized by the same color coordinates but different CRI.

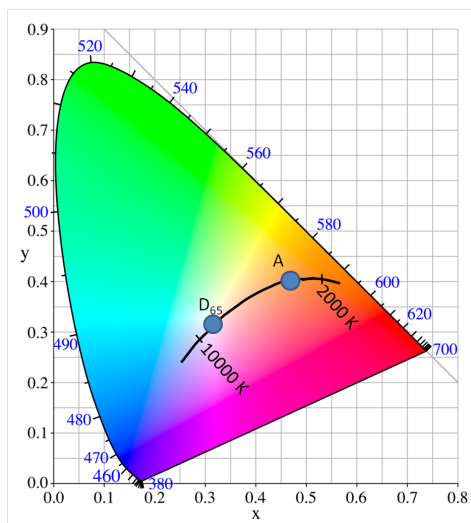


Figure 1.7: CIE 1931 chromaticity diagram. The black line indicates the black body radiation line as a function of the temperature, point A indicates the emission from a tungsten incandescent lamp, at 2856 K, and point D₆₅ refers to daylight, \sim 6770 K.

As mentioned in the previous section, if charge blocking layers are employed the recombination efficiency is approximately one. The internal quantum efficiency of OLEDs is then limited by the percentage of excitons which can radiatively decay to the ground state and the material-specific radiative decay probability. By exploiting phosphorescent materials, all excitons can potentially radiatively decay to the ground state. An example of a fully phosphorescent device is given in figure 1.8 (a), as published by Reineke *et al.*, ref. 6. In the figure the highest occupied molecular orbital (HOMO) energy level and lowest unoccupied molecular orbital (LUMO) energy level are shown for each material composing the layer stack. Silver and Indium Tin Oxide (ITO) are employed as cathode and anode, respectively. Holes are injected without facing any energy barrier from α -NPD (also called NPB, hole-transport layer) to the TCTA:Ir(MDQ)₂(acac) layer. This layer is composed of a TCTA host matrix where the red-emitting phosphores-

cent $\text{Ir}(\text{MDQ})_2(\text{acac})$ molecule (already shown in figure 1.4) is dispersed. Electron injection is also ohmic from TPBi (electron transport layer) to the TPBi: $\text{Ir}(\text{ppy})_3$ layer (TPBi host and $\text{Ir}(\text{ppy})_3$ green phosphorescent guest, shown in figure 1.4) and the blue phosphorescent FIrpic layer. Electrons and holes accumulate in the TCTA: $\text{Ir}(\text{MDQ})_2(\text{acac})/\text{TCTA}/\text{TPBi}:\text{FIrpic}$ region. The presence of a 2 nm intrinsic host (TCTA) interlayer between the red and blue emitting layers is sufficient to prevent Förster transfer from blue FIrpic excitons to red $\text{Ir}(\text{MDQ})_2(\text{acac})$ excitons. Moreover, exciton diffusion is prevented by the high TCTA triplet level. An intrinsic TPBi interlayer is used to avoid Förster transfer from blue FIrpic to green $\text{Ir}(\text{ppy})_3$ excitons, while host-exciton diffusion is allowed. The green $\text{Ir}(\text{ppy})_3$ -doped region thus diffusively harvests host excitons. Key features of the layer stack are, besides the use of phosphorescent materials, (i) the use of a blue host matrix which is resonant with the blue guest emitter, i.e. characterized by similar triplet energy, so blue phosphorescence is not accompanied by internal triplet energy relaxation before emission, (ii) the presence of low energy barriers for hole and electron transport throughout the whole stack, thus reducing the applied voltage needed to drive the device. An overall external quantum efficiency of 46% is reached, corresponding to 124 lm/W, making use of optical macroextractors, already discussed. A drawback of this system is represented by the use of the phosphorescent blue emitting molecule, FIrpic. It is known to be characterized by low stability over time.^{6,31} This results in a device lifetime, defined as the time at which the emission at a constant voltage drops to half of the initial light intensity, of only 1-2 hours at 1000 cd/m².⁶ A general disadvantage of phosphorescent devices is the typical “roll-off” of the external quantum efficiency at high voltage regimes. It is generally attributed to triplet-triplet quenching processes (particularly effective due to the long triplet diffusion length), although recently other causes have been indicated to play a role, such as the less effective charge blocking at high operation voltages.³²

A possible solution which avoids the use of blue phosphors is the concept of hybrid OLEDs,³³ where a fluorescent blue layer is present in combination with red and green phosphorescent layers. An evolution³⁴⁻³⁶ of this concept consists of a triplet “harvesting” approach where the blue spectral component is due to singlet exciton emission, while triplets generated in the blue layer can diffuse to the phosphorescent layers, where they are converted into red and green emitting triplets. An example of such a structure is shown in figure 1.8 (b), presented by Schwartz *et al.*, ref. 35. Holes are injected from the ITO anode, through a *p*-doped hole transport layer (p-HTL) and an electron blocking layer (EBL), into the red phosphorescent $\alpha\text{-NPD}:\text{Ir}(\text{MDQ})_2(\text{acac})$ and the blue fluorescent 4P-NPD layer. Electrons are injected from the aluminum cathode, through an *n*-doped electron transport layer (n-ETL) and hole-blocking layer (HBL), into the green phosphorescent TPBi: $\text{Ir}(\text{ppy})_3$ layer. The electron-hole mobility balance is such that excitons are generated mainly close to the interface between the blue and the green layer. In the TPBi: $\text{Ir}(\text{ppy})_3$ layer, all generated excitons are converted into green triplets, which will decay radiatively. Singlets generated in the blue layer may either decay radiatively or transfer their energy to the adjacent green phosphors via Förster transfer. This will lead to an enhanced green

component in the emission. Triplets in the blue layer are either directly generated via e-h recombination or they originate from Dexter-transfer from the adjacent green triplets, which are characterized by a comparable energy (~ 2.3 eV). Blue triplets are non-emissive since 4P-NPD is a fluorescent molecule. Nevertheless, Dexter energy transfer can occur from blue to red triplets, located in the adjacent α -NPD:Ir(MDQ)₂(acac) layer (this transition is favorable in energy, as the red triplets energy is ~ 2 eV). The large distance between the exciton generation region in the blue layer and the red layer is sufficient to prevent blue singlet conversion to red excitons. As already mentioned in the previous section, triplet states are often characterized by a larger diffusion length compared to singlets, so the diffusion of blue triplets to the red layer is quite probable. A key feature of the system consists in the use of a blue fluorescent material characterized by a high triplet state, which makes the blue to red triplet conversion particularly efficient.

A different way to realize hybrid fluorescent-phosphorescent emission is presented in figure 1.8 (c), presented by Lindla *et al.*, ref. 37. Holes are injected from the ITO anode and reach the emitting region through an hole transport layer. Electrons are injected from the LiF/Al cathode and reach the emitting layers via the hole blocking TMM004³⁸ layer and an electron-transport layer. The key feature of the layer stack is the presence of a “cross-fading mixed-matrix” layer, i.e. two host molecules are employed with a relative concentration varying across the layer, composed of TCTA and TMM004, doped with a red phosphor (TER031)³⁸ and a green phosphor (Irppy). Between the green emitting layer and the blue emitting layer (SMB013³⁸ host and SEB115³⁸ fluorescent guest) an interlayer of intrinsic mixed-host TCTA:TMM004 is present to avoid energy transfer from the green triplet to the lower blue triplet. The use of a mixed-host matrix allows to optimize both the electron-hole mobility balance and the localization of the exciton generation region for optimal outcoupling.

A different OLED concept is known as stacked-device. An example of state-of-the-art structure was recently presented by Chiba *et al.*, ref. 39. This type of device is characterized by the presence of charge generation layers (CGL) in between the emitting layers, so that the whole stack can be considered as a series of single-emitting-layer OLEDs. The use of separate structures for injection into the red, green and blue emitting layers provides more freedom in balancing the three spectral components. Moreover, the subdivision of the OLED in separate stack elements decreases the probability of shorts generation and the presence of multiple photon generation regions gives rise to a higher emission intensity as compared to a corresponding unstacked OLED driven at the same current density. This last feature was proven to be favorable for the device lifetime.³⁹ More fundamentally, the presence of higher volumes from which emission is realized contributes to reducing the chances for exciton-exciton quenching, thus enhancing the emitted light intensity. The disadvantage of this type of device is represented by the technological challenge, and related additional costs, to evaporate a large number of layers, and the need to drive the device at a voltage which is $\sim n$ times larger than that of a corresponding unstacked device, if n is the number of stacks composing the OLED.

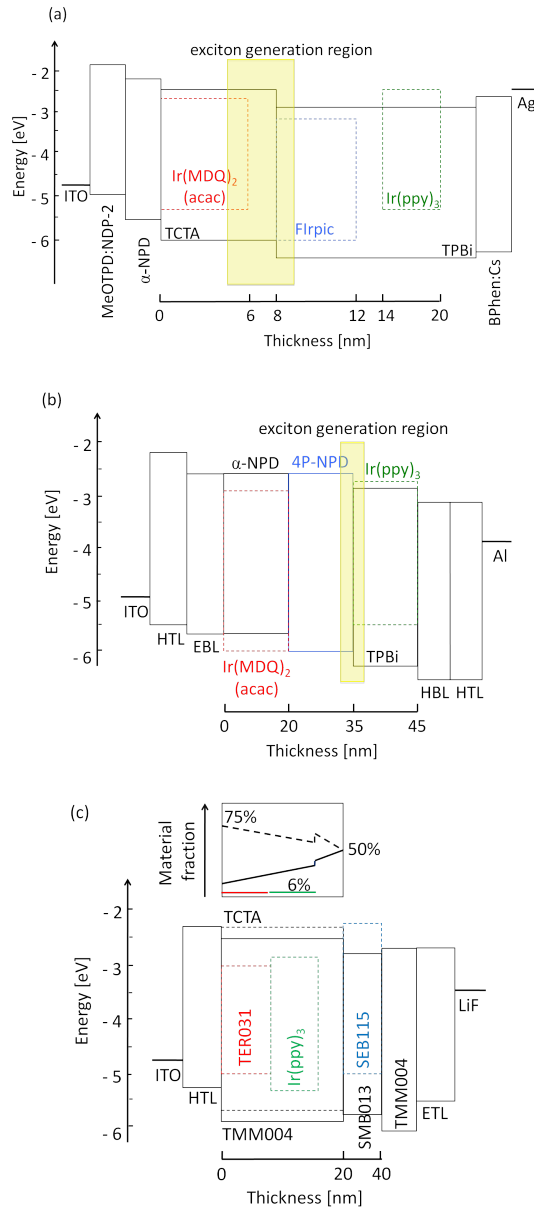


Figure 1.8: State-of-the-art OLED structures and energy level diagram. The yellow zones in structures (a) and (b) indicate the region where excitons are mainly generated. (a) Phosphorescent device, after ref. 6; green excitons are generated by energy transfer from blue excitons. (b) Hybrid fluorescent-phosphorescent device, after ref. 35; red excitons are generated by energy transfer from blue excitons. (c) Hybrid fluorescent-phosphorescent device with mixed-host matrix, after ref. 37. In this device the exciton generation region is spread over all emitting layers.

In all OLED structures presented, a crucial element to be controlled is the precise position of the light-emission profile. It will not only determine the light-outcoupling efficiency, but also the balance between the different spectral components which contribute to the white emission spectrum. Being able to reconstruct the light-emission profile would provide a wealth of information concerning the charge recombination physics and photophysics of the OLED analyzed. Moreover, it will be shown in the examples which follow that the crucial layers which determine the emission spectrum and intensity are only a few nanometers thick. A method is thus needed to reconstruct the light-emission profile with a nanometer-scale resolution. Probably the most direct way to probe the electron-hole recombination profile (somewhat different from the light-emission profile, as previously mentioned) is to use a sensing layer. This concept was introduced by Tang and co-workers⁴⁰ for a bilayer OLED. In that case a diamine was used as a hole-transporting layer, while Alq₃ constitutes the electron-transport layer. Due to the poor electron-transport properties of the diamine used, excitons are expected to be generated within the Alq₃ layer. A very thin red fluorescent DCM₂ layer is used as an exciton-trap layer within the green-emitting Alq₃ layer. By varying the distance of the DCM₂ layer from the diamine interface, the DCM₂ contribution to the electroluminescence spectrum changes, thus providing an indication of the width of the exciton generation profile. Such a direct approach presents two main drawbacks: additional *ad hoc* devices must be fabricated (where the sense layer material should be carefully chosen such that the charge transport of the device is only minimally influenced) and the resolution is limited by the ability to produce series of nominally identical devices where only the position of the thin sensing layer is changed. Throughout this thesis we will show a novel approach which makes it possible to reconstruct the light-emission profile with a nanometer-scale resolution, with no need for additional *ad hoc* devices.

1.4 The scientific questions we want to answer - scope of this thesis

In all state-of-the-art devices described above, a crucial underlying feature is the precise control of the exciton generation region. With emitting layer thickness values on the nanometer-scale, a slight hole-electron mobility unbalance can lead to an unbalance of the spectral contribution from the different layers, and consequently to a shift of the color-point. The availability of a method to measure the light-emission profile across the emitting layers with nanometer-scale resolution would be essential in OLED layer-stack development, OLED electrical device model validation, and investigation of the photophysics of test devices. It would allow for example to non-invasively detect the cause of a slight spectral shift as a function of the applied voltage or during the device lifetime, attributable to a light emission profile change. The main objective of this thesis is thus to answer the following questions:

- **Is it possible to experimentally reconstruct the light-emission profile in organic light-emitting diodes with nanometer resolution?**
- **What can be learnt about the device photophysics exploiting this information?**

In this thesis we will present a method which makes it possible to reconstruct the light-emission profile from the measurement of the wavelength-, polarization- and angle-dependent electroluminescent spectra. The method will be introduced in **chapter 2**, followed by an extensive analysis of the ultimate resolution with which a light-emission profile can be reconstructed in **chapter 3**. A detailed comparison between our profile reconstruction method and other approaches published in the literature is also presented in these chapters. In figure 1.9 the approach is summarized. As an input for the modelling part of the method, the complex refractive index dispersion curves and the photoluminescence quantum yield of the emitters are needed. The first can be measured via ellipsometry, the second via a procedure already presented by de Mello and co-workers.⁴¹ When OLEDs containing multiple (different) emitters are considered, e.g. for white emitting devices, a source spectrum characterizing the different emitters is needed. For this purpose, photoluminescence spectra measured on thin-films of the emitting materials deposited on quartz can be used. This information, together with an accurate knowledge of the thickness of each layer in the stack, will serve as input for the optical microcavity model. Emission spectra as a function of the wavelength, emission angle and polarization are calculated for oscillating dipoles (excitons) as a function of the distance from the electrodes, using a microcavity model. The (incoherent) parameterized sum of the contributions from the different dipoles is compared to the measured wavelength-, emission angle- and polarization-dependent electroluminescence spectra. Through an error minimization routine the light-emission profile is reconstructed. The most critical ingredients for a proper reconstruction of the light-emission profile are the following. First, an accurate measurement is needed of each layer thickness within the device stack. This value can be in principle deduced by treating it as a fit parameter within the reconstruction algorithm. However, in particular for multi-layer stacks, a strong correlation can exist between the changes in the thickness value of different layers located between the emitting region and the metallic electrode. Alternatively, transmission electron microscopy (TEM) measurements of test samples can be employed to accurately measure the thickness of the different organic layers. Secondly, accurate material characterization for each layer is essential, providing the complex refractive dispersion curves, the photoluminescence spectrum (if needed, see above) and the radiative decay probability. Third, there is not a generally accepted method to treat the effects of optical birefringence and self-absorption. Our approach will be described in chapter 2.

In subsequent chapters three applications of the light-emission profile reconstruction method will be discussed. The first application is the development of an accurate and comprehensive method to determine the exciton singlet fraction, i.e. the fraction of singlet excitons over the total amount of generated excitons. The method is presented in **chapter 4**, and it is applied to polyfluorene- and

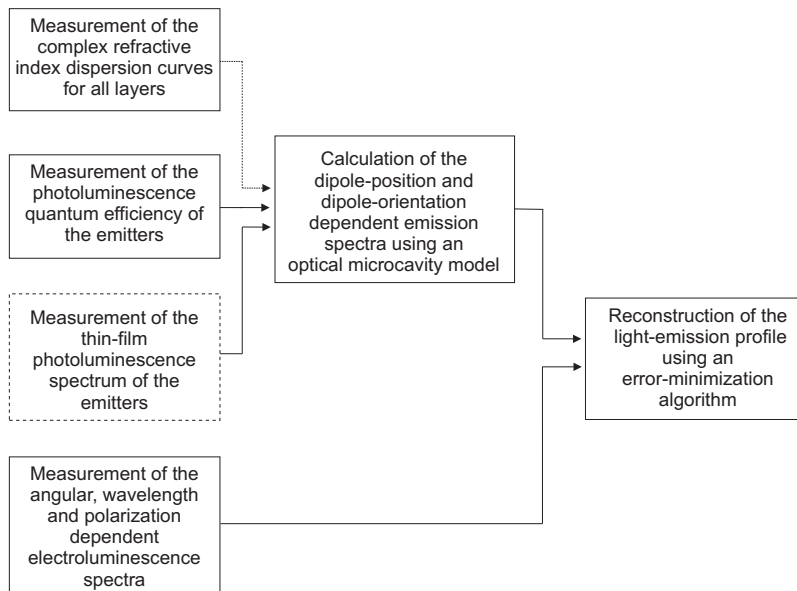


Figure 1.9: Schematic of the light-emission profile reconstruction approach which is discussed in this thesis. The dashed rectangle indicates a measurement needed only in case multiple (different) emitters are present, e.g. for white-light emitting devices.

PPV-based single-layer devices. In all cases the singlet fraction is found to be lower than the standard quantum-statistical value of 25%.

As a first step towards the analysis of a multilayer stacks for white emission, in **chapter 5** the photophysics near organic-organic interfaces is investigated. We have studied a double-layer device composed of α -NPD and BA1q. A shift of the light-emission profile from the α -NPD side to the BA1q side of the interface was measured, when the BA1q layer thickness was increased while the α -NPD layer thickness was fixed. The delicate balance between excitonic emission, from α -NPD and BA1q, and CT state emission at the organic-organic interface is investigated.

The last step, presented in **chapter 6**, consists of investigating the emission profile in a hybrid white-light emitting multilayer device. The method provides a deeper understanding about the key role of the exciton blocking interlayer, employed to prevent energy exchange between a fluorescent blue and a phosphorescent green layer, and about the main photophysical processes which determine the external quantum efficiency of the device.

This thesis is concluded by an outlook in **chapter 7**, where other application directions for the light-emission reconstruction method presented are sketched. First, the possibility to validate charge-transport and recombination models for OLEDs is discussed. Furthermore, we analyze potential applications of the method to other types of devices, such as light-emitting electrochemical cells and light-emitting field-effect transistors.

1.5 References

1. C. W. Tang and S. A. van Slyke, *Appl. Phys. Lett.* **51**, 913 (1987).
2. J. H. Burroughes, D. D. C. Bradley, A. R. Brown, R. N. Marks, K. Mackay, R. H. Friend, P. L. Burn and A. B. Holmes, *Nature* **347**, 539 (1990).
3. International Energy Agency, *Light's labour's lost - Policies for energy-efficient lighting* (2006), <http://www.iea.org>
4. www.konicaminolta.com
5. www.universaldisplay.com
6. S. Reineke, F. Lindner, G. Schwartz, N. Seidler, K. Walzer, B. Lüssem and K. Leo, *Nature* **459**, 234 (2009).
7. www.lumiblade.com
8. M. Pope and C. E. Swenberg, *Electronic Processes in Organic Crystals and Polymers*, Oxford University Press, New York (1999).
9. Y. Cao, I. D. Parker, G. Yu, C. Zhang and A. J. Heeger, *Nature* **397**, 414 (1999).
10. J. S. Kim, P. K. H. Ho, N. C. Greenham and R. H. Friend, *J. Appl. Phys.* **88**, 1073 (2000).
11. M. Wohlgenannt, K. Tandon, S. Mazumdar, S. Ramasesha and Z. V. Vardeny, *Nature* **494**, 409 (2001).
12. J. S. Wilson, A. S. Dhoot, A. J. A. B. Seeley, M. S. Khan, A. Köhler and R. H. Friend, *Nature* **413**, 828 (2001).
13. A. S. Dhoot, D. S. Ginger, D. Beljonne, Z. Shuai and N. C. Greenham, *Chem. Phys. Lett.* **360**, 195 (2002).
14. M. Wohlgenannt, X. M. Jiang, Z. V. Vardeny and R. A. J. Janssen, *Phys. Rev. Lett.* **88**, 197401 (2002).
15. M. Segal, M. A. Baldo, R. J. Holmes, S. R. Forrest and Z. G. Soos, *Phys. Rev. B* **68**, 075211 (2003).
16. T. Virgili, G. Cerullo, C. Gadermaier, L. Lüer, G. Lanzani and D. D. C Bradley, *Phys. Rev. Lett.* **90**, 247402 (2003).
17. C. Yang, Z. V. Vardeny, A. Köhler, M. Wohlgenannt, M. K. Al-Suti and M. S. Khan, *Phys. Rev. B* **70**, 241202(R) (2004).
18. C. Rothe, S. M. King and A. P. Monkman, *Phys. Rev. Lett.* **97**, 076602 (2006).
19. M. Reufer, M. J. Walter, P. G. Lagoudakis, A. B. Hummel, J. S. Kolb, H. G. Roskos, U. Scherf and J. M. Lupton, *Nat. Mater.* **4**, 340 (2005).
20. Z. Shuai, D. Beljonne, R. J. Silbey and J. L. Brédas, *Phys. Rev. Lett.* **84**, 131 (2000).
21. M. N. Kobrak and E. R. Bittner, *Phys. Rev. B* **62**, 11473 (2000).

22. S. Karabunarliev and E. R. Bittner, *Phys. Rev. Lett.* **90**, 057402 (2003).
23. A. Kadashchuk, A. Vakhnin, I. Blonski, D. Beljonne, Z. Shuai, J.-L. Brédas, V. I. Arkhipov, P. Heremans, E. V. Emelianova and H. Bässler, *Phys. Rev. Lett.* **93**, 066803 (2004).
24. J. Gruener, F. Cacialli and R. H. Friend, *J. Appl. Phys.* **80**, 207 (1996).
25. S. Mladenovski, S. Reineke and K. Neyts, *Opt. Lett.* **34**, 1375 (2009).
26. K. Neyts, *J. Opt. Soc. Am. A* **15**, 962-971 (1998).
27. D. E. Markov and P. W. M. Blom, *Appl. Phys. Lett.* **87**, 233511 (2005).
28. O. V. Mikhnenko, P. W. M. Blom and M. A. Loi *Phys. Chem. Chem. Phys.* **13**, 14443 (2011).
29. A. Köhler and H. Bässler, *Materials Science and Engineering R* **66**, 71 (2009).
30. *Commission internationale de l'Eclairage proceedings, 1931*, Cambridge University Press, Cambridge (1932).
31. R. J. Holmes, B. W. D'Andrade, S. R. Forrest, X. Ren, J. Li and M. E. Thompson *Appl. Phys. Lett.* **83**, 3818 (2003).
32. N. C. Giebink and S. R. Forrest *Phys. Rev. B* **77**, 235215 (2008).
33. G. Schwartz, K. Fehse, M. Pfeiffer, K. Walzer and K. Leo, *Appl. Phys. Lett* **89**, 083509 (2006).
34. Y. Sun, N. C. Giebink, H. Kanno, B. Ma, M. E. Thompson and S. R. Forrest, *Nature* **440**, 908-912 (2006).
35. G. Schwartz, M. Pfeiffer, S. Reineke, K. Walzer and K. Leo, *Adv. Mater.* **19**, 3672-3676 (2007).
36. G. Schwartz, S. Reineke, K. Walzer and K. Leo., *Appl. Phys. Lett.* **92**, 053311 (2008).
37. F. Lindla, M. Boesing, C. Zimmermann, P. van Gemmern, D. Bertram, D. Keiper, M. Heuken, H. Kalisch and R. H. Jansen, *J. Photon. En.* **1**, 011013 (2011).
38. Merck KGaA, Darmstadt, Germany, Material Datasheet.
39. T. Chiba, Y.-J. Pu, R. Miyazaki, K.-I. Nakayama, H. Sasabe and J. Kido, *Org. Electron.* **12**, 710 (2011).
40. C. W. Tang, S. A. VanSlyke and H. Chen, *J. Appl. Phys.* **85**, 3610 (1989).
41. J. C. de Mello, H. F. Wittmann and R. H. Friend, *Adv. Mater.* **9**, 230 (1997).

2

Measuring the light-emission profile in organic light-emitting diodes with nanometer spatial resolution

In the Introduction the importance of a method to reconstruct the light-emission profile with nanometer resolution has been explained, in order to get quantitative understanding of the charge recombination and photophysical processes in OLEDs. In this chapter, we present a comprehensive method for accurately measuring the shape of the emission profile, the intrinsic spectrum of emitting dipoles and the emitting dipole orientation. The method employs a microcavity light outcoupling model which includes self-absorption and optical anisotropy, and is based on the full wavelength, angle and polarization resolved emission intensity. Application to blue (polyfluorene-based) and orange-red (NRS-PPV) polymer OLEDs reveals a peaked shape of the emission profile. A significant voltage and layer thickness dependence of the peak positions is observed, with a demonstrated resolution better than 5 nm.[†]*

*The work presented in this chapter has been published: S. L. M. van Mensfoort, M. Carvelli, M. Megens, H. Greiner, D. Wehenkel, M. Bartyzel, R. A. J. Janssen and R. Coehoorn, *Nat. Photon.* **4**, 329-335 (2010), with the exception of figure 5 and related discussion, which has been corrected in this thesis, as explained in the main text.

[†]M. Carvelli and S. L. M. van Mensfoort contributed equally to this work.

2.1 Introduction

In the past five years, organic light-emitting diodes (OLEDs) have emerged as a promising option for energy-efficient solid-state lighting¹⁻⁵ and for cheap light sources produced on flexible foils.^{6,7} The highest luminous efficacies, of more than 100 lm/W to date,^{5,8} are obtained using multilayer structures of evaporation-deposited small-molecule organic semiconductors. Flexible OLEDs are usually based on a single active layer deposited by spin-coating or ink-jet printing. Within both technologies, a key factor that needs to be controlled is the shape of the emission profile, i.e. the spatial distribution of the emitting excitons across the active layer thickness. As has been revealed using microcavity models,⁹⁻¹³ exciton quenching near the electrodes can lead to a light-outcoupling efficiency that is significantly smaller than the value of $\sim 20\%$ for fully planar state-of-the-art multilayer OLEDs,⁵ in which the emission is confined to a layer near the center of the device.

In single-layer OLEDs, the shape of the emission profile depends on the injection conditions and on a delicate balance between the electron and hole mobilities.¹⁴ For studying this interplay, the availability of a method for deducing the precise shape of the profile from measured emission spectra would be desirable. Crucial elements of the methods that have been proposed for solving this “inverse light-outcoupling problem”^{9,15-21} are the use of a combined classical and quantum-mechanical microcavity model for properly treating the radiative decay probability,^{9,15,16,18-21} the inclusion of optical absorption in the emitting layer (“self-absorption”)¹⁷ and of optical anisotropy,^{15,17,19} a self-consistent determination of the intrinsic electroluminescence (EL) spectrum¹⁷ and the use of the full angular dependence of the emission.^{16,17} This last feature is of essential importance for determining the emission profile with high resolution. The angular range can be enhanced using edge emission from the substrate¹⁶ or by making use of an optical hemisphere.¹⁹ However, in none of the methods all these elements are combined. Due to the lack of a complete model it is presently not clear to what extent quantitative measurements of the profile are feasible.

In this chapter, we present a comprehensive novel method to determine the shape of the emission profile, combining all essential elements mentioned above. This allows us for the first time to measure the shape of the profile with such an accuracy that we can detect with nm-scale resolution a voltage (V) and layer thickness (L) dependence. The method is applied to blue and orange-red emitting OLEDs, based on a polyfluorene copolymer (PF-TAA) and a poly(phenylenevinylene) derivative (NRS-PPV), which are members of widely studied archetypical classes of polymers. For both systems, a strongly peaked emission profile is found with a significant voltage and layer thickness dependence. It is argued that a better than 5 nm resolution of peak shifts can be obtained. For the PF-TAA based OLEDs the emission takes place mainly close to the anode, consistent with results from device modelling,²² while for the NRS-PPV based diodes the emission is in all cases close to the middle of the device.

2.2 Solving the inverse outcoupling problem

Figure 2.1 illustrates the question we wish to address: how can we determine the profile of emitting dipoles in a ~ 100 nm thick emitting layer that is embedded in a stack of several other layers in an OLED structure, with a resolution better than 10 nm? The figure gives the molecular structures of the fluorene-(7.5 mol-% triarylamine) co-polymer (PF-TAA) and the poly(2-methoxy-5-(3',7'-dimethyloctyloxy)-p-phenylene vinylene) poly[4'-(3,7-dimethyloctyloxy)-1,1'-vinylene] (NRS-PPV) light-emitting polymer (LEP) layers used, and shows a schematic cross-section of the layer stacks studied: glass/ ITO (120 nm)/ PEDOT:PSS (100 nm)/ LEP/ barium (5 nm)/ aluminum (100 nm). In each case, OLEDs with three LEP layer thicknesses were investigated, with $L = 100, 130, 160$ nm and $L = 60, 90, 120$ nm for the PF-TAA and NRS-PPV based devices, respectively. The PF-TAA copolymer studied in this chapter has been used as the blue emitter in the 13" full-color OLED-TV display demonstrated by Philips in 2005.²³

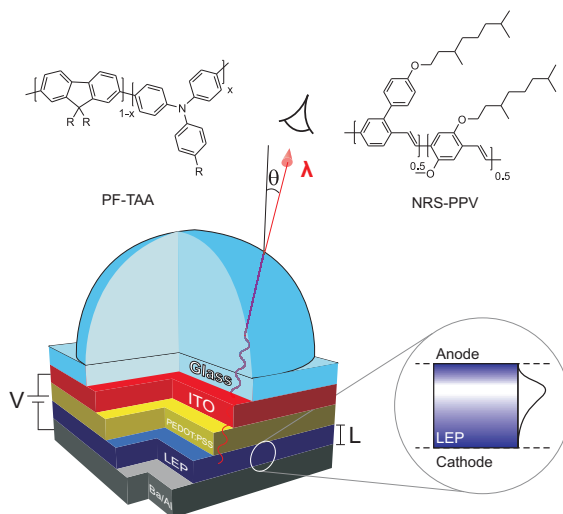


Figure 2.1: Schematic diagram, illustrating the measurement of the shape of the emission profile in an OLED. The layer thickness (L) and voltage (V) dependent emission profile in the light-emitting polymer (LEP) layer, depicted schematically in the right part of the figure, is determined from an analysis of the angle (θ), wavelength (λ) and polarization dependence of the emission intensity, making use of a glass hemisphere. The active material components are PF-TAA and NRS-PPV.

The spectra from which the emission profile is deduced have been obtained for both s and p polarization, and for a wide range of emission angles θ , defined with respect to the surface normal. As shown in figure 2.1, use is made of a glass-hemisphere, so that emission is extracted from modes which would otherwise stay undetected due to internal reflection at the glass/air interface. The shape

of the spectra is found to show a pronounced θ , V and L dependence. As an example, figure 2.2 shows emission spectra for 100 nm and 160 nm PF-TAA based devices, measured at two voltages and at two angles. No polarizer was used for these specific measurements. For the 100 nm device, the shoulder in the emission spectrum at a wavelength of ~ 500 nm almost vanishes when increasing the emission angle from 0° to 70° . In contrast, for the 160 nm device the opposite trend is observed, as it becomes then the most dominant peak. The significant V dependence found provides already a strong indication for a V dependence of the shape of the emission profile. It was found after the publication of ref. 24 that an angular-dependent correction (the measured intensities have to be multiplied by $\cos \theta$) should be applied to the measured EL intensities. This leads to a correction of the reconstructed light-emission profiles as compared to those published. The corrected profiles are shown in figure 2.5. Figures 2.2, 2.3, 2.6, 2.8, 2.9 and 2.10 are left equal to those published, since the main conclusions which can be drawn from the analysis of these figures will not change. The fit-quality, shown in figure 2.3, actually slightly improves after the correction.

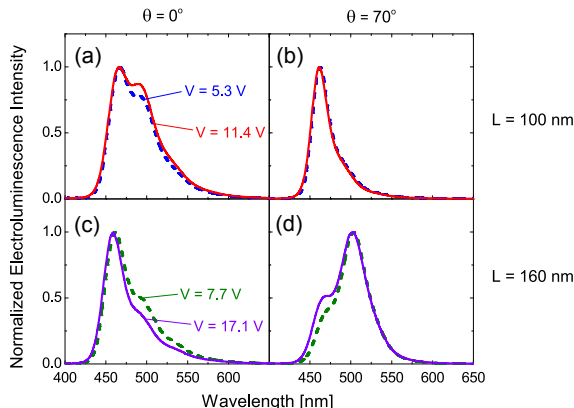


Figure 2.2: Angular dependence of the EL spectra²⁵ for PF-TAA based OLEDs. Normalized electroluminescence (EL) spectrum for blue-emitting PF-TAA based OLEDs, measured at emission angles $\theta = 0^\circ$ and $\theta = 70^\circ$, for 100 nm and 160 nm devices studied at two voltages.

The emission profile is obtained by describing the measured spectra as linear combinations of the spectra calculated for the emission at varying depths within the cavity, with the emission profile as the depth dependent weight function. A key feature of our method is that no intrinsic emission spectrum is assumed. Instead, the method provides this spectrum. For the forward calculation, we have used a well-established light-outcoupling model, within which the excitons are treated (classically) as radiating dipole emitters.^{10,26} The model has been extended to include the effects of optical absorption in the emitting layer and birefringence of the polymer layers. Selfabsorption is expected to be important, as for the materials studied the intrinsic EL spectrum shows overlap with the absorption

spectrum. Ellipsometry is used for carefully determining the required wavelength dependent refractive index functions. The emission profile is obtained by carrying out a least-squares fit to the measured angle, wavelength and polarization dependent intensities, after normalizing the intensities for a given wavelength and polarization by the angle-averaged intensity for that wavelength and polarization. An in-depth description of the method is contained in appendix B (section 1). The normalization procedure makes it possible to obtain the intrinsic emission spectrum directly from the analysis. Furthermore, it gives more weight to the information obtained for wavelengths in the tails of the spectra and it makes the analysis insensitive to the calibration details of the spectrometer employed, making it possible to obtain the emission profile with improved accuracy.

Figures 2.3 and 2.4 explain the method in more detail. Figure 2.3 shows examples of a comparison of measured and calculated normalized emission intensities for the OLEDs studied. The figure reveals the richness of the information contained in the experimental data, and shows to which extent it can be described using the model. In figure 2.4 the bottom part shows the normalized wavelength and angle resolved emission intensities for both polarizations, as calculated for emission from four different positions in the 160 nm PF-TAA based OLED.

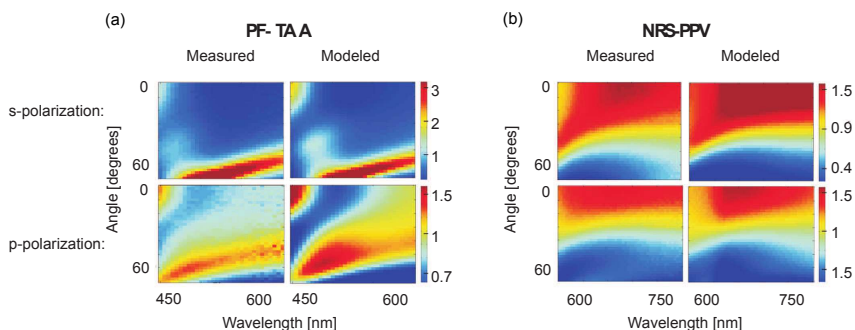


Figure 2.3: Comparison of measured²⁵ and modeled spectra. Measured and modeled angle, wavelength and polarization dependent normalized emission intensities for (a) a 160 nm thick PF-TAA based OLED, studied at $V = 7.7$ V and (b) a 60 nm thick NRS-PPV-based OLED, studied at $V = 3$ V. The color coding, optimized for each case, is indicated by the scale bars at the right-hand-side of the plots.

The (average) angle of the emitting dipoles with respect to the surface-plane (θ_d) was assumed to be equal to zero. Visual comparison with the experimental intensities given in figure 2.3 at 7.7 V already clearly reveals that the emission takes place in a region more close to the anode. This is confirmed by carrying out a full quantitative analysis, which leads to the emission profile shown in the top part of figure 2.4. The analysis makes use of a physically realistic smooth three-parameter fit function for the dipole intensity as a function of the distance to the anode, with one maximum. It furthermore satisfies the requirement that the emission vanishes at the electrode interfaces. There is no net exciton formation

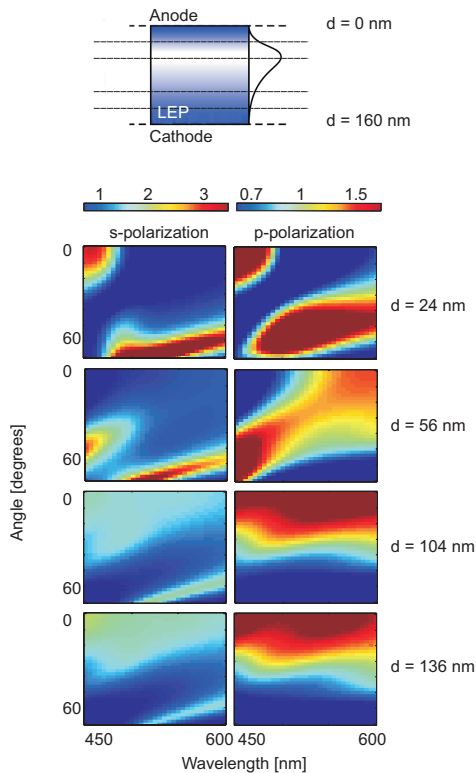


Figure 2.4: Position dependent emission intensities. Bottom: angle and wavelength dependent normalized emission intensities, calculated for emission from single planes within a 160 nm thick PF-TAA based OLED, located at the four positions indicated in the top part of the figure. The color coding, indicated by the scale bars, is optimized for each polarization.

at the electrodes as, due to the local thermal equilibrium, the quasi Fermi-levels for electrons and holes coincide so that the rates of exciton formation and free charge carrier generation are equal. We note that this will not only apply to metal electrodes, but also to electrodes based on PEDOT:PSS, which are known to give rise to efficient hole injection in OLEDs based on e.g. certain polyfluorene-copolymers²⁷ or PPV-derivatives.²⁸ It would therefore be of interest to reconsider the results of earlier analyses of the emission profile in OLEDs in which a significant emission intensity at the anode has been reported, as presented e.g. recently by Gather *et al.*²¹ for spirofluorene-based devices.

The three parameters allow quite independent control over the peak position, the peak width and the peak asymmetry, respectively. The expression for the specific parameterized profile used is given and motivated in detail in appendix B (section 2). The fitting procedure involves also, as a fourth parameter, the

dipole orientation angle θ_d , which defines the relative weights of in-plane dipoles ($\cos^2 \theta_d$) and perpendicular dipoles ($\sin^2 \theta_d$).

2.3 Emission profiles for PF-TAA and NRS-PPV based OLEDs

Figure 2.5(a-c) shows the emission profiles determined for the blue-emitting PF-TAA based devices with $L = 100, 130$ and 160 nm, respectively, at three values of applied voltage for each device. Results of a similar analysis performed on NRS-PPV-based devices with $L = 60, 90$ and 120 nm are shown in figure 2.5(d-f).

For these two types of devices radiative decay probabilities of 0.60 and 0.25 are assumed, respectively, as obtained from the photoluminescence (PL) quantum yield measured for single LEP layers spin-coated on glass in an integrating sphere spectrometer. For two of the cases studied, the quality of the fits may be judged from the comparison with experiment given in figure 2.3. For the entire angular range and for both s and p polarization the most significant experimental spectral features are well described by the modeled intensity distribution. For example, for PF-TAA, the relatively strong emission at high angles is well described, as well as the strong and polarization dependent emission at small angles and small wavelengths. For NRS-PPV, the normalized emission patterns are less structured and the emission is more concentrated at smaller angles, as described well by the model.

In the three PF-TAA based devices studied the emission profile peaks at all applied voltages used at a position quite close to the anode, in accordance with previous predictions from device modelling.²² The peak shifts further towards the anode with increasing voltage. The consistency in the trend of the peak position and width with voltage suggests that the (relative) peak positions are resolved within ~ 5 nm. This is confirmed by explicit calculations of the sensitivity of the method to possible random experimental errors, presented below. The peak shift reflects a shifting balance towards more strongly electron-dominated transport. We note that from the available descriptions of the effects of energetic disorder on the hole²⁹ and electron mobility³⁰ functions in PF-TAA such an effect is indeed expected, as a result of the more important effect of trap states in the electron transport. However, the presence of a sizeable electron injection barrier (~ 0.5 eV²²) will also play a role. The observed emission profiles are therefore expected to provide an important benchmark for advanced device models within which the effects of energetic disorder and an injection barrier on the interplay between injection, transport and recombination is taken into account.

The emission profiles for NRS-PPV based OLEDs shown in figure 2.5(d-f) are surprisingly narrow as compared to the exciton generation profiles as published in the literature by Markov and Blom,³¹ who studied 120 nm devices. Moreover, the distance of the profile peak from the cathode is in all cases larger than 40 nm. The narrow emission profiles could be due to anisotropy in the charge mobility functions (charges move faster along the polymer chains, which are predominantly

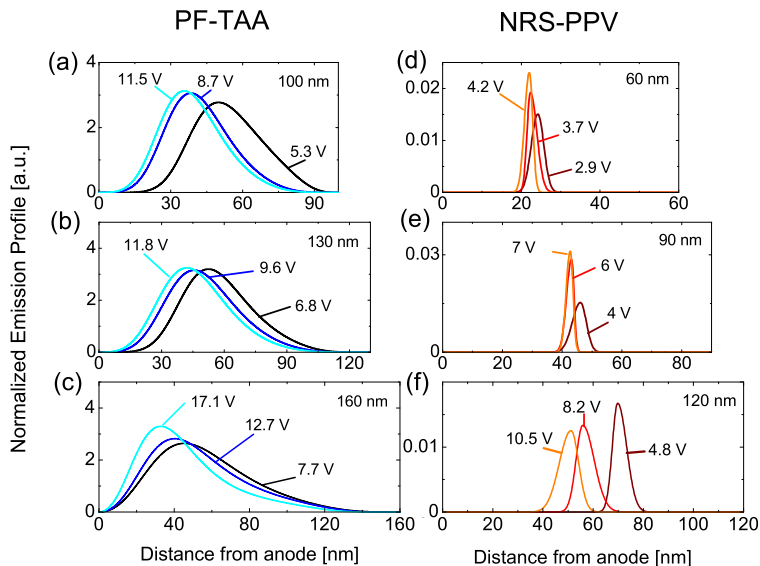


Figure 2.5: Voltage and layer thickness dependence of the emission profile. Normalized emission profiles as determined by the method presented, for PF-TAA based devices with $L = 100$ nm (a), 130 nm (b) and 160 nm (c), and for NRS-PPV based devices with $L = 60$ nm (d), 90 nm (e) and 120 nm (f), at the voltages indicated.

oriented parallel to the layer interface). Exciton diffusion would broaden the emission profile. However this effect is expected to be small, as the singlet exciton diffusion length for fluorescent polymers is generally believed to be only ~ 5 nm, see for example ref. 31. In the absence of injection barriers and electron trap sites, one would in fact expect the hole-electron mobility to be balanced, thus the recombination shall happen in roughly in the middle of the device. Since the presence of electron traps has been demonstrated already for this material,³¹ one possible explanation for the localization of the profile in the middle of the emitting layer and not close to the cathode, as predicted,³¹ would consist in assuming the presence of an injection barrier for holes from PEDOT:PSS.

2.4 Internal consistency and accuracy limits

The internal consistency of the method follows, in the first place, from the observation that, for both polymers studied, the normalized intrinsic EL source spectra obtained are essentially independent of the emissive layer thickness and the voltage. Furthermore, they can be used to successfully predict the PL spectrum.

This is shown in figure 2.6(a), which gives the normalized intrinsic EL emission (“source”) spectrum as obtained for the PF-TAA based devices, as well as the predicted and measured PL spectrum for a 100 nm film on glass. The relative PL spectral intensity at small wavelengths is, as compared to the EL source spectrum, decreased due to self-absorption.

For PF-TAA, the internal consistency also follows from the observation that, for all voltages and layer thicknesses, an essentially equal average dipole orientation is obtained. It falls in the range 0° to 20° (see appendix B). The observation of such a small angle can be viewed as an indication that the dipole orientation is determined by the orientation of the polymer chains, which are expected to be predominantly in-plane due to the spin coating process. A similarly strong degree of orientation has been found earlier for polymer-based devices from PL³² and EL¹⁶ emission measurements or from X-ray diffraction.³³ For the NRS-PPV devices studied, the analysis is found to be less sensitive to the dipole orientation. The optimal, device averaged, orientation is approximately 20° .

In order to study the accuracy limits of the method, we first analyze the sensitivity of the determined peak positions to the presence of random (uncorrelated) Gaussian errors, added to the measured intensity obtained for each angle, wavelength and polarization. Figure 2.6(b) shows a superposition of 1000 profiles as calculated from the experimental intensities to which 20% Gaussian noise has been added, a factor of 10 larger than the actual value in order to more clearly visualize the effects of experimental uncertainties. The figure shows that even in such a case the shape of the profile is only very weakly affected by the noise. The inset shows that a statistically significant voltage-dependence of the peak position can still be resolved. It is thus well possible for this case to accurately determine the small peak shift.

More generally, the accuracy depends on the specific material and the layer thickness. We have analyzed the accuracy limits of the method by investigating the well-conditionedness of the set of linear equations relating the measured emission intensities to the shape of the emission profile. The degree to which errors in the measured data propagate to the calculated emission profile can be obtained by analyzing the properties of the matrix which connects both quantities, as discussed in detail in appendix B (section 4). We consider a system with emission from K discrete planes, uniformly distributed over the layer thickness at relative distances equal to $1/K$. The dipole angles are taken equal to $\theta_d = 0^\circ$. The analysis is carried out for the PF-TAA and NRS-PPV devices studied in this chapter, for $K = 3$ and 5, as a function of the emitting layer thickness L . We thus analyze the cases of three and five degrees of freedom, and view the $K = 3$ case as representative to our approach, although this employs a three-parameter continuum shape function instead of a discrete shape function. Figure 2.6(c) shows the calculated relative error in the emission profile, assuming a (realistic) 2% error in the experimental emission intensities. The figure shows that the relative error decreases with increasing L , as may be expected from the fact that then the distance in between the emitting planes increases so that obtaining good spatial resolution becomes less difficult. In order to obtain a good resolution, it is thus, in general, advisable to use a large layer thickness. A weak oscillation of the

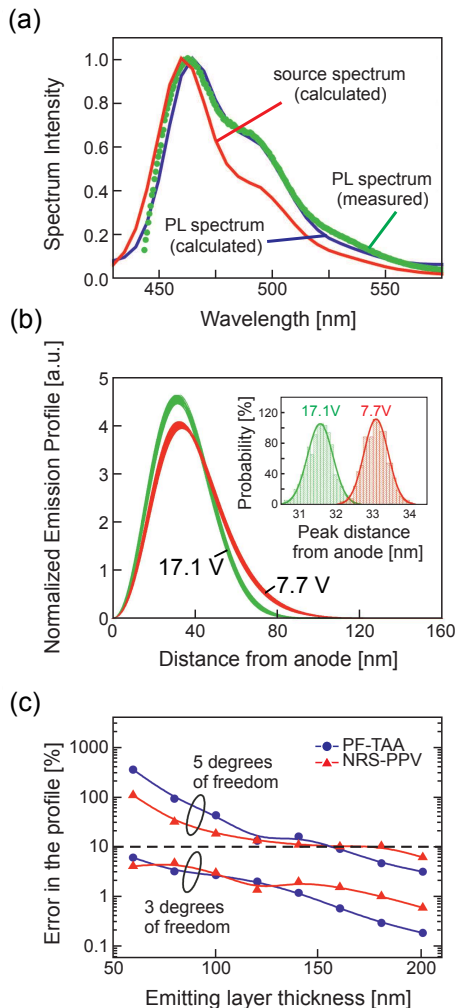


Figure 2.6: Consistency and resolution.²⁵ (a) Calculated source spectrum, measured PL spectrum and PL spectrum calculated from the source spectrum, for a 100 nm PF-TAA layer on glass. (b) Effect on the determined light emission profile in 160 nm PF-TAA based OLEDs at 7.7 and 17.1 V, if uncorrelated relative Gaussian noise of 20% is added to the measured intensity values. Inset: the corresponding distribution of peak positions. (c) Layer thickness dependence of the error in each of the K intensities defining a discrete emission profile with $K = 3$ or 5 degrees of freedom, for PF-TAA (spheres) and NRS-PPV (triangles) based devices, assuming a 2% experimental error.

curves is found, which may be viewed as a microcavity effect. The figure shows that the relative uncertainty in each of the K discrete intensities describing the emission profile is less than 10% (dashed line) if the profile is described by three

degrees freedom. The figure also shows that resolving with such an accuracy five degrees of freedom would, for both materials, only be possible for layer thicknesses larger than 160 nm. Furthermore, we demonstrate in appendix B that limiting the analysis to the normal emission spectrum only, as has been done in several studies,^{15,18,20,21} severely reduces the attainable resolution.

2.5 Conclusions

A novel method was presented for determining the voltage and layer-thickness dependent emission profile and average dipole orientation in single layer OLEDs. It is based on the wavelength and polarization dependence of the emission within a wide angular range, which is shown to be essential for obtaining high resolution, and it employs a comprehensive optical outcoupling model which includes self-absorption and optical anisotropy. The method was applied to OLEDs based on a blue-emitting PF-TAA copolymer and on the orange-red emitting polymer NRS-PPV. For both materials, it is found that the dipole orientation is fully or almost fully in-plane, which can be understood from a predominant in-plane orientation of the polymer chains due to the spin coating process. In OLEDs with active layer thicknesses of the order 100 nm, a resolution of the voltage-dependent peak-position shifts better than ~ 5 nm has been demonstrated.

We expect that the method will be an important tool for the optimization of the power efficiency and lifetime of OLEDs. Knowing the light emission profile with high accuracy is required for calculating the light outcoupling efficiency, which is the most important efficiency loss factor in state-of-the-art OLEDs. The high resolution will make it possible to study the subtle changes of the emission profile during the operational lifetime, thereby contributing to the microscopic-scale understanding of lifetime limiting effects. Our approach is not restricted to a specific class of shapes of the emission profile. We are currently extending the analysis to multilayer devices, for which a more structured profile is expected. Determination of the light outcoupling efficiency will also make it possible to more accurately deduce the internal quantum efficiency (IQE) from the external quantum efficiency. This is a crucial step towards the understanding of all factors which limit the IQE, including for example the fraction of singlet excitons formed. For fluorescent polymer OLEDs this is a subject of intensive debate.³⁴⁻³⁷

2.6 Appendix A

1. Experimental set-up

The wavelength, angle and polarization-dependent radiance of the light emitted from the OLEDs is measured (in units $\text{Wm}^{-2}\text{nm}^{-1}\text{sr}^{-1}$) using a Melcher Autronic Display Metrology System (DMS). The wavelength steps are 5 nm. Using the DMS, emission spectra can be obtained at any angle from 0 to 90° . The use of the glass hemisphere allows us to detect external light emission up to angles of 70° , in steps of 2° . This makes it possible to detect internal emission under angles that would otherwise give rise to total internal reflection. An index-matching fluid is applied in between the hemisphere and the OLED, with the same refractive index as the glass substrate, in order to make proper optical contact.

2. Optical outcoupling-model

The optical outcoupling model employed, LIGHTEX, is a computer simulation tool developed at Philips Research Aachen that treats excitons as radiating dipole emitters.²⁶ LIGHTEX is used for calculating the dipole-orientation dependent external emission spectrum as a function of the emitting dipole position in the cavity and as a function of the external emission angle and polarization. LIGHTEX takes into account the effects of reflection and refraction at interfaces, of absorption in the layers, of exciton quenching, and of a finite radiative decay probability. The model also considers that the actual radiative decay probability in the microcavity is enhanced close to the electrodes, as compared to the “intrinsic” radiative decay probability for an emitter in an infinite slab of the organic material. Therefore, the decay probability depends on the distance of the emitter to the electrodes. Furthermore, all optical modes are considered. In these respects the model is very similar to the models described in Refs 9,15,18,19,38. Within these models, to all layers a complex refractive index is assigned, except for the emitting layer, for which the imaginary (absorptive) part of the refractive index is usually set to zero.

In order to include now the effect of absorption in the emitting layer, we use the following approach. For calculating the emission spectrum for a plane of dipole emitters at a certain position between anode and cathode the emitting layer is subdivided in three parts: a central part that contains the plane of dipoles with a width of ~ 10 nm (~ 5 nm towards both electrodes), and two outer parts more close to the anode and cathode. To the outer sublayers the full complex refractive index of the material is assigned whereas to the middle sublayer only the real (nonabsorptive) part is assigned. This rather practical approach avoids numerical divergencies in the calculation of the emission intensities. By taking self absorption into account, the fit quality is found to increase slightly, but the shape of the emission profile obtained is only very weakly affected (see appendix B for a detailed analysis). We note that it is still a point of debate in the literature how to physically treat emission from a radiating dipole in a medium that is itself absorbing at the emission wavelength of the dipole.^{39,40}

The optical anisotropy of the LEP and the PEDOT:PSS layer is taken into account by introducing an effective refractive index that is a function of the angle in the anisotropic layer. The approach is the same as presented in Ref. 41 for

the real part of the refractive index, but is now applied to the complex refractive index.

2.7 Appendix B

1. Analysis method

The shape of the emission profile and the intrinsic EL emission (“source”) spectrum are obtained in the following way using a least-mean-squares fitting method. As a first step, the experimental s and p polarized emission intensities $I_{s(p)}^{\text{expt}}(\lambda, \theta)$, measured at M values of the wavelength λ and N values of the emission angle θ , are normalized using the expression

$$I_{\text{norm},s(p)}^{\text{expt}}(\lambda, \theta) = \frac{I_{s(p)}^{\text{expt}}(\lambda, \theta)}{S_{s(p)}^{\text{expt}}(\lambda)}, \quad (2.1)$$

with

$$S_{s(p)}^{\text{expt}}(\lambda) \equiv \frac{1}{N} \sum_{j=1}^N I_{s(p)}^{\text{expt}}(\lambda, \theta_j) \quad (2.2)$$

angle-averaged experimental spectral intensities. In the same manner, the normalized s and p emission spectra for a trial emission profile $P(\delta)$, where $\delta \equiv d/L$ is the normalized distance to the anode, and a trial dipole orientation θ_d are calculated, making use of the emission $I_{s(p)}^{\text{calc}}(\lambda, \theta, \delta, \theta_d)$ from unit dipoles at a position δ obtained from the LIGHTEX program:

$$I_{\text{norm},s(p)}^{\text{calc,trial}}(\lambda, \theta) = \frac{\int_0^1 P(\delta) I_{s(p)}^{\text{calc}}(\lambda, \theta, \delta, \theta_d) d\delta}{S_{s(p)}^{\text{calc,trial}}(\lambda)}, \quad (2.3)$$

with

$$S_{s(p)}^{\text{calc,trial}}(\lambda) \equiv \frac{1}{N} \sum_{j=1}^N \int_0^1 P(\delta) I_{s(p)}^{\text{calc}}(\lambda, \theta_j, \delta, \theta_d) d\delta \quad (2.4)$$

angle-averaged calculated spectral intensities. The starting point of the calculation is thus a flat emission spectrum.

The optimal emission profile and dipole orientation are found by iteratively minimizing the quantity

$$\chi^2 \equiv \sum_{i=1}^M \sum_{j=1}^N \sum_{s,p} \{I_{\text{norm},s(p)}^{\text{calc,trial}}(\lambda_i, \theta_j) - I_{\text{norm},s(p)}^{\text{expt}}(\lambda_i, \theta_j)\}^2. \quad (2.5)$$

From the angle-averaged spectral intensities obtained for the optimized parameter set the source spectrum is then calculated using

$$S_{\text{source}}(\lambda) = \frac{S_s^{\text{expt}}(\lambda) + S_p^{\text{expt}}(\lambda)}{S_s^{\text{calc,opt}}(\lambda) + S_p^{\text{calc,opt}}(\lambda)}. \quad (2.6)$$

2. Parameterized function describing the shape of the emission profile

In this study, we describe the shape of the emission profile using the following three-parameter function:

$$P(\delta, p, w, a) = \frac{\sin^2(\pi\delta)\Gamma(w+1)}{\Gamma(wg(\delta, a)+1)\Gamma(w-wg(\delta, a)+1)} p^{wg(\delta, a)} (1-p)^{w-wg(\delta, a)}. \quad (2.7)$$

Γ is the Euler Gamma function. $P(\delta, p, w, a)$ is a smooth function which vanishes at the electrodes, as motivated in the main text, and shows a single peak for a value of δ in between 0 and 1. The peak position, peak width and peak asymmetry are determined by the parameters p , w and a , respectively. The function is based on the continuum form of the binomial distribution function, given by

$$P_{\text{bin}}(\delta, p, w) = \frac{\Gamma(w+1)}{\Gamma(w\delta+1)\Gamma(w-w\delta+1)} p^{w\delta} (1-p)^{w-w\delta}. \quad (2.8)$$

Varying the peak parameter p from 0 to 1 gives rise to a peak shift from the anode to the cathode. With increasing width parameter w (a number in between 0 and infinity), the peak becomes narrower. The requirement that the function vanishes at the electrode planes is realized by multiplying $P_{\text{bin}}(\delta, p, w)$ by the function $\sin^2(\pi\delta)$. For that purpose, multiplication with a $\sin(\pi\delta)$ would already be sufficient. However, results of OLED device modeling assuming bimolecular (Langevin) recombination suggest that quite generally the recombination rate increases superlinearly with increasing distance to the electrodes, motivating the choice for a \sin^2 function.⁴² It should be remarked that in the work of Markov *et al.*³¹ the maxima in the recombination profile are found at one or both polymer/electrode interfaces. This is due to the use of a drift-only model for calculating the current density and recombination profile. The most important change obtained from more realistic drift-diffusion modeling is that the recombination rate at the interfaces will vanish.

Control over the peak asymmetry is realized by deforming the shapes of the increasing and decreasing slopes of the peak while leaving the peak position (at δ_{peak}) and the end points unchanged. This is done by introducing a transformation $\delta \rightarrow \delta' \equiv g(\delta, a)$, specified by an asymmetry parameter a which is such that at both sides of the peak the difference between δ and δ' has the same sign. We have used the simplest possible polynomial function $g(\delta, a)$ that satisfies these criteria, which is given by

$$\delta' = g(\delta, a) = (1+a)\delta + x\delta^2 + y\delta^3 + z\delta^4. \quad (2.9)$$

With increasing asymmetry parameter a , the difference between δ and δ' becomes larger. The coefficients x , y and z are fully determined by the requirements $g(0, a) = 0$, $g(1, a) = 1$, $g(\delta_{\text{peak}}, a) = \delta_{\text{peak}}$, and $\partial g/\partial \delta = 1$ at $\delta = \delta_{\text{peak}}$. If $a = 0$, leading to $x = y = z = 0$, there is no (additional) asymmetry. Figure 2.7(a-c) shows examples of the function $P(\delta, p, w, a)$, normalized with respect to the integral over δ , for variations in p , w and a , while keeping the other parameters constant.

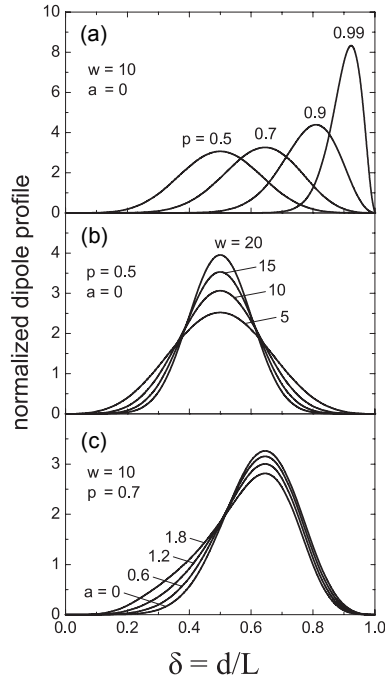


Figure 2.7: Examples of area-normalised emission profiles generated using Eq. (2.7), for (a) varying peak position parameter p , (b) varying peak width parameter w , and (c) varying peak asymmetry parameter a .

The parametrization used is quite versatile. E.g., it includes the possibility to describe emission with a peak close to one electrode interface, but with a long tail into the bulk of the device. We emphasize that, however, depending on the specific system studied, other parameterizations may be more suitable. An emission profile with a single rather narrow peak is expected for the case of Langevin recombination in single-layer OLEDs within which the electron and hole mobilities are strongly charge carrier density dependent as a result of the presence of strong energetic disorder.²² This is the situation expected to be relevant to the materials studied in this chapter. However, a strong field-dependence of the mobilities could lead to a much wider recombination profile with even two local maxima.^{22,43} For both types of OLEDs studied, we have verified that analyses using a more general parameterization of the shape function which allows for a double peak structure converges to a single peak structure.

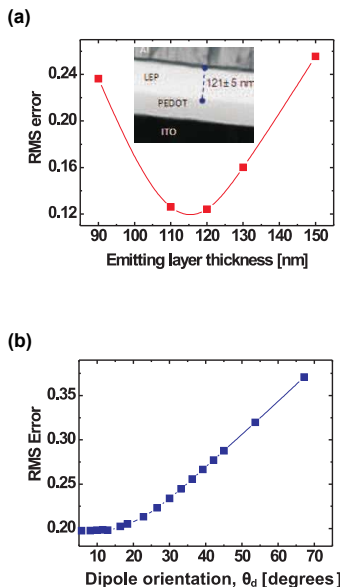


Figure 2.8: Sensitivity of the fit quality²⁵ to the layer thickness and average dipole orientation. (a) Minimum root-mean-square (RMS) error as a function of the emitting layer thickness assumed in the calculations for a nominally 120 nm thick NRS-PPV device, for which a TEM cross-section is shown as an inset. (b) Minimum RMS error as a function of the dipole angle assumed for a 100 nm PF-TAA based device.

3. Sensitivity of the fit quality to the layer thickness, average dipole orientation and self-absorption

In addition to the internal consistency checks discussed in the main text, we have investigated the sensitivity of the quality of the fit to a variation of the thickness of the emissive layer. Figure 2.8(a) gives for an NRS-PPV based device with a nominal emitting layer thickness of 120 nm the root mean square (RMS) error as a function of the emitting layer thickness assumed in the analysis. The figure reveals a strong sensitivity to that thickness, and shows that the minimum RMS error is obtained for an assumed emitting layer of 116 nm. This coincides within the accuracy margins with the thickness of 121 ± 5 nm that was determined by a Transmission Electron Microscopy (TEM) measurement. The TEM image is shown as an inset.

Figure 2.8(b) shows the sensitivity of the RMS error to the assumed dipole orientation angle for a 100 nm PF-TAA device. From the figure, θ_d is estimated to be 0° to 20° . A similar angular variation of the RMS error is found for different layer thicknesses and voltages.

As mentioned in the Methods section, self-absorption in the emitting layer is included in our modeling approach by subdividing the layer in three regions, one central region around the dipole which is non-absorbing and two outer regions

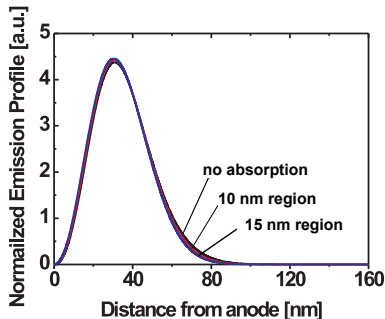


Figure 2.9: Sensitivity of the shape of the profile to the thickness of the central non-absorbing layer²⁵. Calculated emission profiles for a 160 nm thick PF-TAA device, at 17.1 V, for 10 nm and 15 nm widths of the non-absorbing region centered around the dipole position, and for the case in which the whole emitting layer is considered as non-absorbing. The shape of the profile is only weakly affected by the choice of the width of the non-absorbing central region.

which are absorbing. The assumed thickness of the central region is 10 nm. Figure 2.9 shows that the determined shape of the emission profiles is only weakly affected by the choice of a larger central region width (15 nm instead of 10 nm), or even by assuming a totally non-absorbing emitting layer. However, we find that the minimum RMS error is for both cases approximately 5 percent larger than for a 10 nm thick central layer. This small sensitivity can be understood from the rather large Stokes-shift, giving rise to relatively weak self-absorption.

4. The resolution limit - full angle analysis *versus* normal emission analysis

In this subsection we discuss in a more extended way the resolution limits involved in the method, by analyzing the well-conditionedness of the inverse outcoupling problem. As mentioned already in the main text, we consider a system with emission from K discrete planes, uniformly distributed over the layer thickness at relative distances equal to $1/K$. The dipole angles are taken equal to $\theta_d = 0^\circ$. We analyze under which conditions the internal emission intensities at each plane, $x(k)$ with $k = 1$ to K , can be properly resolved. Making use of the formalism developed in the section 1, these intensities may be viewed as a solution of a matrix equation, $A \cdot x = b$. The matrix A has dimensions $2NM \times K$. Its K columns give the normalized emission from each plane expressed by Eq. 5.5. The vector $b \equiv I_{\text{norm}}^{\text{expt}}$, with dimension $2NM$, gives the normalized experimental wavelength, angle and polarization dependent intensity. From standard matrix theory,⁴⁴ it is known that the maximum ratio between the relative error in the norm of the output vector x and the relative error in the norm of the input vector b is equal to the so-called condition number, κ , of the matrix A . So a large condition number implies that a small measurement error can already give rise to a large error in the calculated emission profile.

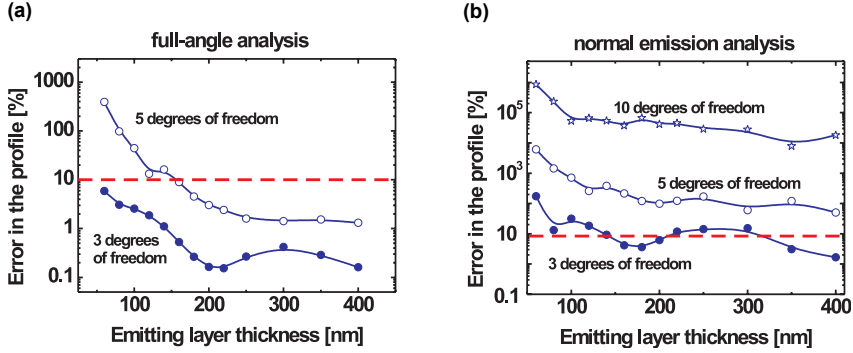


Figure 2.10: The resolution limit - full angle analysis *versus* normal emission analysis²⁵. (a) Layer thickness dependence of the error in the profile, for PF-TAA based devices and for 3 and 5 degrees of freedom (see text), using a full angle analysis. (b) Layer thickness dependence of the error in the profile for PF-TAA based devices and for 3, 5 and 10 degrees of freedom, using only the normal emission spectrum. Already for three degrees of freedom the error in the profile is higher than 10% if the layer thickness is less than ~ 140 nm. In both figures, an experimental error equal to 2% is assumed. The dashed lines shows the 10% error level.

Figure 2.10(a) shows the calculated error in the emission profile for the PF-TAA devices studied in this Article for the cases $K = 3$ and 5. It is an extension of the figure shown in the main text to a larger emitting layer thickness range L . The typical error in the norm of the input vector b may be estimated as follows. The experimental errors involved in the measurements using the Autronic DMS system used are approximately 2%. Assuming that these errors are uncorrelated, the relative error in the norm of b is approximately $0.02/\sqrt{(2NM)} \approx 4 \times 10^{-4}$ for both systems considered. The error in the components of the emission profile vector x is then equal to $4 \times 10^{-4} \cdot \kappa(A)$. In general, we observe that the error in the profile decreases with increasing layer thickness.

In figure 2.10(b) the results of a similar analysis are shown in case only the normal emission spectrum is used, assuming 3, 5 or 10 degrees of freedom. Again, an overall decrease of the error in the profile with increasing layer thickness is observed. However, for a given number of degrees of freedom K the error in the profile is in all cases up to almost one order of magnitude larger than when using spectra obtained within the full angular range. Furthermore, the relative errors in the norm of the experimental intensity vector b are a factor of $\sqrt{72} \sim 8.5$ larger, as a result of not making use of spectra taken at the 36 angles and two polarization directions. As a result, already for three degrees of freedom the uncertainty on the profile is higher than 10% (dashed line) if the layer thickness is less than ~ 140 nm. The figure shows that resolving five degrees of freedom or more with 10% or better accuracy is not possible within the entire thickness range considered.

5. Refractive indices

The wavelength-dependent complex refractive indices of the ITO layer, the LEP layer and the PEDOT:PSS layer were determined from ellipsometry measurements using a Woollam Variable Angle Spectroscopic Ellipsometer (VASE). The LEP layer and the PEDOT:PSS layer were found to be optically anisotropic. Figure 2.11(a,b) show, respectively, the real part, n , and the imaginary part, k , of the measured wavelength dependent refractive index for the PF-TAA based emitting layer, for an in-plane and out-of-plane electric field, measured using ellipsometry. Figure 2.11(c,d) and figure 2.11(e,f) show similar results for NRS-PPV and PEDOT:PSS, respectively. The birefringent nature of PEDOT:PSS has been observed earlier by Pettersson *et al.*⁴⁵

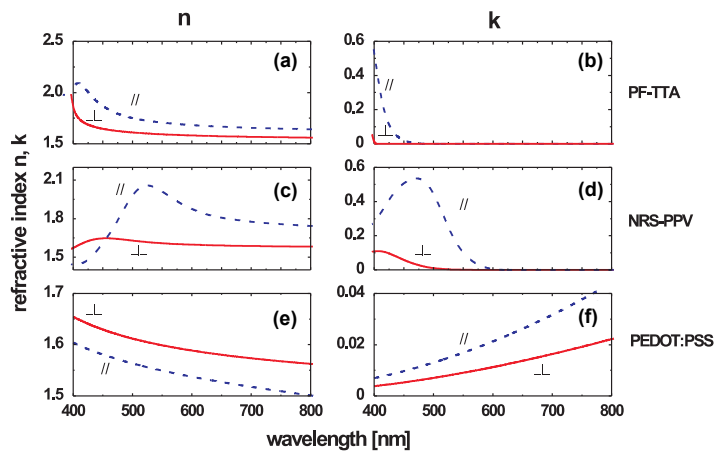


Figure 2.11: Refractive indices of the polymer layers. Wavelength dependence of the real (n) and imaginary (k) part of the refractive index of a thin (~ 100 nm) film of the PF-TAA co-polymer (a, b), NRS-PPV (c, d) and PEDOT:PSS (e, f).

2.8 References

1. B. W. D'Andrade and S. R. Forrest, *Adv. Mater.* **16**, 1585-1595 (2004).
2. Y. Sun, N. C. Giebink, H. Kanno, B. Ma, M. E. Thompson and S. R. Forrest, *Nature* **440**, 908-912 (2006).
3. G. Schwartz, M. Pfeiffer, S. Reineke, K. Walzer and K. Leo, *Adv. Mater.* **19**, 3672-3676 (2007).
4. S. O. Jeon, K. S. Yook, C. W. Joo and J. Y. Lee, *Opt. Lett.* **34**, 407-409 (2009).
5. S. Reineke, F. Lindner, G. Schwartz, N. Seidler, K. Walzer, B. Lüssem and K. Leo, *Nature* **459**, 234 (2009).
6. G. Gustafsson, Y. Cao, G. M. Treacy, F. Klavetter, N. Colaneri and A. J. Heeger, *Nature* **357**, 477-479 (1992).
7. G.-F Wang, X.-M. Tao and R.-X Wang, *Nanotechnology* **19**, 145201 (2008).
8. B. W. D'Andrade, J. Esler, C. Lin, V. Adamovich, S. Xia, M. S. Weaver, R. Kwong and J. J. Brown, *Proc. SPIE* **7051**, 70510Q (2008).
9. M.-H Lu and J. C. Sturm, *J. Appl. Phys.* **91**, 595-604 (2002).
10. K. Neyts, *J. Opt. Soc. Am. A* **15**, 962-971 (1998).
11. V. Bulović, V. B. Khalfin, G. Gu, P. E. Burrows, D. Z. Garbuov and S. R. Forrest, *Phys. Rev. B* **58**, 3730-3740 (1998).
12. X.-W. Chen, W. C. H. Choy and S. He, *J. Displ. Techn.* **3**, 110-117 (2007).
13. S. Nowy, B. C. Krummacker, J. Frischeisen, N. A. Reinke and W. Brütting, *J. Appl. Phys.* **104**, 123109 (2008).
14. G. G. Malliaras and J. C. Scott, *J. Appl. Phys.* **83**, 5399-5403 (1998).
15. W. M. V. Wan, R. H. Friend and N. C. Greenham, *Thin Solid Films* **363**, 310-313 (2000).
16. J.-S. Kim, P. K. H Ho, N. C. Greenham and R. H. Friend., *J. Appl. Phys.* **88**, 1073-1081 (2000).
17. T. Granlund, L. A. A. Pettersson, O. and Inganäs, *J. Appl. Phys.* **89**, 5897-5902 (2001).
18. J. M. Leger, S. A. Carter, B. Ruhstaller, H.-G. Nothofer, U. Scherf, H. Tillman and H.-H. Hörhold, *Phys. Rev. B* **68**, 054209 (2003).
19. M. Roberts, *Proceedings of OEC* 1 (2006).
20. B. Ruhstaller, T. Flatz, M. Moos, G. Sartoris, M. Kiy, T. Beierlein, R. Kern, C. Winnewisser, R. Pretot, N. Chebotareva, and P. van der Schaaf, *SID Symposium Digest of Technical Papers* **38**, 1686 (2007).
21. M. C. Gather, M. Flämmich, N. Danz, D. Michaelis and K. Meerholz, *Appl. Phys. Lett* **94**, 263301 (2009).

22. R. Coehoorn, S. I. E Vulto, S. L. M. van Mensfoort, J. Billen, M. Bartyzel, H. Greiner and R. Assent, *Proc. SPIE*, **6192**, 61920O (2006).
23. N. C. Van der Vaart, H. Lifka, F. P. M. Budzelaar, J. E. J. M. Rubingh, J. J. L. Hoppenbrouwers, J. F. Dijkman, R. G. F. A. Verbeek, R. van Woudenberg, F. J. Vossen, M. G. H. Hiddink, J. J. W. M. Rosink, T. N. M. Bernards, A. Giraldo, N. D Young, D. A. Fish, M. J. Childs, W. A. Steer, D. Lee, D. S. George, *J. Soc. Inf. Disp.* **13**, 9 (2005).
24. S. L. M. van Mensfoort, M. Carvelli, M. Megens, H. Greiner, D. Wehenkel, M. Bartyzel, R. A. J. Janssen and R. Coehoorn, *Nat. Photon.* **4**, 329-335 (2010).
25. It was found after the publication of ref. 24 that an angular-dependent correction (the measured intensities have to be multiplied by $\cos \theta$) should be applied to the measured EL intensities. This leads to a correction of the reconstructed light-emission profiles as compared to those published. The corrected profiles are shown in figure 2.5. Figures 2.2, 2.3, 2.6, 2.8, 2.9 and 2.10 are left equal to those published, since the main conclusions which can be drawn from the analysis of these figures will not change. The fit-quality, shown in figure 2.3, actually slightly improves after the correction.
26. H. Greiner and O. J. F. Martin, *Proc. of SPIE* **5214**, 248-259 (2004).
27. R. U. A. Kahn, D. D. C. Bradley, M. A. Webster, J. L. Auld and A. B. Walker, *Appl. Phys. Lett.* **84**, 921-923 (2004).
28. M. M. de Kok, M. Buechel, S. I. E. Vulto, P. van de Weijer, E. A. Meulenkamp, S. H. P. M. de Winter, A. J. G. Mank, H. J. M. Vorstenbosch, C. H. L. Weijtens and V. van Elsbergen, *Phys. Stat. Sol. A* **201**, 1342-1359 (2004).
29. S. L. M. Van Mensfoort, S. I. J. Vulto, R. A. J. Janssen and R. Coehoorn, *Phys. Rev. B* **78**, 085208 (2008).
30. S. L. M. Van Mensfoort, J. Billen, S. I. L. Vulto, R. A. J. Janssen and R. Coehoorn, *Phys. Rev. B* **80**, 033202 (2009).
31. D. E. Markov and P. W. M. Blom, *Appl. Phys. Lett.* **87**, 233511 (2005).
32. H. Becker, S. E. Burns and R. H. Friend, *Phys. Rev. B* **56**, 1893-1905 (1997).
33. C. Y. Yang, F. Hide, M. A. Diaz-Garcia, A. J. Heeger and Y. Cao, *Polymer* **39**, 2299-2304 (1998).
34. Y. Cao, I. D. Parker, G. Yu, C. Zhang and A. J. Heeger, *Nature* **397**, 414-417 (1999).
35. J. S. Wilson, A. S. Dhoot, A. J. A. B. Seeley, M. S. Khan, A. Köhler and R. H. Friend, *Nature* **413**, 828-831 (2001).
36. M. Segal, M. A. Baldo, R. J. Holmes, S. R. Forrest and Z. G. Soos, *Phys. Rev. B* **68**, 075211 (2003).
37. C. Rothe, S. M. King and A. P. Monkman, *Phys. Rev. Lett.* **97**, 076602 (2006).
38. S. Nowy, N. A Reinke, J. Frischeisen and W. Brütting, *Proc. of SPIE* **6999**, 69992V (2008).

39. M .S. Tomaš and Z. Lenac, *Phys. Rev. A* **56**, 4197-4206 (1997).
40. M. S. Tomaš, *Phys. Rev. A* **63**, 053811 (2001).
41. W. M. V. Wan, N .C. Greenham and R. H. Friend, *J. Appl. Phys.* **87**, 2542-2547 (2000).

42. R. Coehoorn and S. L. M. Van Mensfoort, *Phys. Rev. B.* **80**, 085302 (2009).
43. B. K. Crone, P. S. Davids, I. H. Campbell and D. L. Smith, *J. Appl. Phys.* **84**, 833-842 (1998).
44. D. S. Watkins, *Fundamentals of matrix computations.*, 2nd edition (Wiley, New York, 2002).
45. L. A. A. Pettersson, S. Ghosh and O. Inganäs, *Org. Elec.* **3**, 143-148 (2002).

3

Spatial resolution of methods for measuring the light-emission profile in organic light-emitting diodes

*In chapter 2 the method we developed to reconstruct the light-emission profile in OLEDs was introduced and a first analysis of the resolution limits was provided. In this chapter, we further investigate resolution limits and compare the method with an alternative approach for deducing the light-emission profile in OLEDs: a comparison is given between our “fit-profile” (FP) method, within which the known physics of the recombination process is employed to describe the shape of the profile using a strongly reduced number of degrees of freedom, and the Tikhonov method, which provides a more general solution. The cases of a delta-function shaped emission profile and a broad single-peak emission profile are investigated. It is demonstrated that for these cases a ~ 1 nm resolution of the peak position may be obtained, provided that the peak is positioned optimally in the OLED microcavity. Finally, an analysis is given for a double-peak emission profile and for a rectangular profile, as may be obtained in multilayer OLEDs, revealing a resolution of ~ 10 nm for the cases studied. It is suggested that, in general, an optimal analysis should be based on a combined Tikhonov-FP approach. An analysis of the experimental accuracy of the spectral measurements concludes the chapter as an appendix.**

*The work presented in this chapter has been published: M. Carvelli, R. A. J. Janssen, and R. Coehoorn, *J. Appl. Phys.* **110**, 084512 (2011).

3.1 Introduction

In the past five years, organic light-emitting diodes (OLEDs) have emerged as a promising option for energy-efficient solid-state lighting and for cheap light sources produced on flexible foils.¹ The luminous efficacies, of more than 100 lm/W to date² when using macroextractors for enhancing the light-outcoupling and 64 lm/W without macroextractors,³ are obtained using multilayer structures of evaporation-deposited small-molecule organic semiconductors. Flexible OLEDs are usually based on a single active layer deposited by spin-coating or ink-jet printing. Within both technologies, a key factor that needs to be measured and controlled is the shape of the emission profile, i.e. the spatial distribution of the emitting excitons across the active layer thickness. Being able to accurately measure the emission profile makes it possible to better understand the voltage dependence of the light-outcoupling efficiency and (in multilayer OLEDs with closely spaced emissive layers) the color stability. Nanometre-scale resolution is required in order to investigate state-of-the-art devices, containing $\sim 10 - 20$ nm thick emitting layers.² The possibility to extract emission profiles with a high accuracy would also be essential to investigate the validity of recombination models.⁴ We note that recently refinements of the standard Langevin-model have been proposed, by more properly including the Coulomb interactions between holes and electrons⁵ and the effect of recombination with trapped charges.^{6,7} Furthermore, being able to resolve a shift of the light-emission profile during the device operational lifetime would provide valuable insight into degradation processes.

A fully experimental method for locating the emission zone, based on the addition of a small concentration of dye-molecules with a red-shifted emission to the emissive layer, has been introduced and applied successfully by Tang and co-workers.⁸ However, the use of this “sense layer” method requires the fabrication of a series of additional OLEDs and its applicability depends on the availability of suitable dye molecules. The light-emission profile can also be obtained from an analysis of measured spectral intensities.^{9–20} We recently proposed a comprehensive novel approach to solve this “inverse outcoupling problem”.²⁰ Crucial elements are (i) the use of the full angular and polarization dependent emission spectra, extracted using a glass hemisphere, (ii) the use of a combined classical and quantum-mechanical microcavity model for properly treating the radiative decay probability and light-outcoupling efficiency, and (iii) the use of a flexible and problem-specific fit function describing the profile. Within this “fit-profile” (FP) approach, enhanced accuracy was obtained by describing the profile in a manner which is consistent with the physics of the known recombination process for the single-layer OLEDs studied. We note that also in earlier studies FP-approaches were employed, using more strongly constrained functions such as a parameterized exponential^{10,15} or a double-exponential fit-profile function.¹² In some cases a single oscillating dipole was used to replicate the experimental data.¹³ A different approach, allowing more flexibility in the profile shape, involves the use of a dense set of dipoles distributed uniformly across the emitting layer.^{17–19} In ref.^{18,19} the contribution of the ensemble of dipoles is regularized, leading to a more smooth light-emission profile. In all these earlier studies no analysis was given of the

accuracy with which the experimental data were collected.

The resolution with which the light-emission profile may be reconstructed from, realistically, noisy spectral data was for the first time discussed in ref. 20 for the case of a broad emission profile in a single-layer OLED. The analysis focused on the emitting layer thickness dependence of the resolution. A formal condition number analysis was performed, as well as a more practical study of the profiles as obtained from a large ensemble of spectral datasets created by adding random noise to the ideal noise-free dataset for the system studied. In this chapter, we compare the resolution limits as obtained using FP-methods and as obtained using a well-established more general and (potentially) high-resolution inverse-problem solving approach, the Tikhonov-method,^{21–23} using the same microcavity model and experimental data and employing the “ensemble method” mentioned above. After analyzing the experimental precision and accuracy, four specific cases are studied, relevant to single-layer, double-layer and multilayer OLEDs. Depending on the case studied, the resolution limit is found to be in the range of ~ 1 to ~ 10 nm. We investigate the resolution as a function of the exciton position within the device, and show how one may design the device for optimal resolution. From the analysis, it is argued that the most optimal approach would be to use the FP-method employing a shape of the profile which is suggested by a pre-analysis using the Tikhonov method.

In Section 4.2 the FP-method and the Tikhonov method, as applied to the inverse light-outcoupling problem, will be described. In appendix, a detailed analysis of the experimental precision and accuracy is presented. In Section 4.4 a comparison is given between the two methods for the four specific cases studied. A summary and conclusions are given in Section 4.5.

3.2 Theoretical methods

The FP and Tikhonov methods involve both a least-squares minimization of a weighed difference between the experimental spectra, measured as a function of the angle and the polarization, and modeled emission spectra. Both experimental and modeled spectra are normalized over the sum of the intensities, in order to enhance the sensitivity to the lower-intensity tails of the spectrum.²⁰ This also makes it possible to extract the “source spectrum”, as will be shown later in this section and as was already discussed in ref. 20. The calculated emission spectra derive from incoherently oscillating dipoles. The OLED stack is modeled as an optical microcavity, using a computer simulation tool, LIGHTEX, developed at Philips Research Aachen.²⁴ The simulations include optical absorption in the emitting layer (“self-absorption”), optical anisotropy and the microcavity effect on the ratio of the radiative and non-radiative decay rates, as described in ref. 20. In all cases, the emission is considered from a source spectrum with a uniform intensity in the 450 to 600 nm wavelength (λ) range, as probed in $M = 31$ equidistant wavelength steps and in $N = 36$ equidistant polar angles (θ) steps in the 0° to 70° range, and for s and p polarization. The intensities can be expressed as an experimental vector b of length $2M \times N$. The profile to be determined is

expressed by a (dense) set of weights of discrete dipoles at equidistant points across the OLED, given by the vector x . Solving the inverse outcoupling problem then implies finding the solution of the equation $A \cdot x = b$, where A is the matrix which models the emission from the OLED microcavity.

Within the FP-method, the dipole weights at each of the grid points are constrained to a specific form of the emission profile, described by only a small number of free parameters. These are obtained by minimizing the difference between the emission intensity as predicted from these parameters and the experimental emission intensities, using a least-squares fitting routine. The parameterization of the fit profile will be adapted optimally to the problem to be solved, as explained in more detail in the case studies given in section 4.4. By making use of a fit profile the reconstructed profile can be constrained to a physically realistic form, with intensities which are non-negative everywhere, zero at the electrode interfaces in the case of injection under thermal equilibrium conditions, and a restricted number of minima and maxima. In order to make this chapter sufficiently self-contained, we briefly summarize the procedure applied to determine the light emission profile, reported in Ref. 20. As a first step, the experimental s and p polarized emission intensities $I_{s(p)}^{\text{expt}}(\lambda, \theta)$ are normalized using the expression

$$I_{\text{norm},s(p)}^{\text{expt}}(\lambda, \theta) = \frac{I_{s(p)}^{\text{expt}}(\lambda, \theta)}{S_{s(p)}^{\text{expt}}(\lambda)}, \quad (3.1)$$

with

$$S_{s(p)}^{\text{expt}}(\lambda) \equiv \frac{1}{N} \sum_{j=1}^N I_{s(p)}^{\text{expt}}(\lambda, \theta_j) \quad (3.2)$$

angle-averaged experimental spectral intensities. In the same manner, the normalized s and p emission spectra for a trial emission profile $P(\delta)$, where δ is the normalized distance to the anode, and a trial dipole orientation θ_d are calculated, making use of the emission $I_{s(p)}^{\text{calc}}(\lambda, \theta, \delta, \theta_d)$ from unit dipoles at a position δ obtained from the LIGHTEX program:

$$I_{\text{norm},s(p)}^{\text{calc,trial}}(\lambda, \theta) = \frac{\int_0^1 P(\delta) I_{s(p)}^{\text{calc}}(\lambda, \theta, \delta, \theta_d) d\delta}{S_{s(p)}^{\text{calc,trial}}(\lambda)}, \quad (3.3)$$

with

$$S_{s(p)}^{\text{calc,trial}}(\lambda) \equiv \frac{1}{N} \sum_{j=1}^N \int_0^1 P(\delta) I_{s(p)}^{\text{calc}}(\lambda, \theta_j, \delta, \theta_d) d\delta \quad (3.4)$$

angle-averaged calculated spectral intensities. The starting point of the calculation is thus a flat emission spectrum. The optimal emission profile and dipole orientation are found by minimizing the quantity

$$\chi^2 \equiv \sum_{i=1}^M \sum_{j=1}^N \sum_{s,p} \{I_{\text{norm},s(p)}^{\text{calc,trial}}(\lambda_i, \theta_j) - I_{\text{norm},s(p)}^{\text{expt}}(\lambda_i, \theta_j)\}^2. \quad (3.5)$$

From the angle-averaged spectral intensities obtained for the optimized parameter set the source spectrum is then calculated using

$$S_{\text{source}}(\lambda) = \frac{S_s^{\text{expt}}(\lambda) + S_p^{\text{expt}}(\lambda)}{S_s^{\text{calc,opt}}(\lambda) + S_p^{\text{calc,opt}}(\lambda)}. \quad (3.6)$$

The fit-profile method makes it possible to include constraints which lead to a solution which is consistent with assumptions made concerning the transport and recombination physics. However, it is not always *a priori* clear which assumptions would be most appropriate. In such cases, sufficient freedom should be given to the shape of the solution. The most general approach would be an unconstrained χ^2 -method, within which the dipole weights at a dense set of grid points across the full thickness of the emissive layer are the degrees of freedom. For solving the corresponding inverse problem, we have used numerical methods which are standardly available,²⁵ including a non-negativity constraint which is obviously required to obtain physically realistic profiles. We will indicate this approach as the “non-negativity-constrained (NNC) χ^2 -method”.

Although non-negativity constrained solutions are already much more realistic than unconstrained solutions, it is often found that the problem is still to such an extent ill-posed that large unphysical point-to-point variations in the dipole intensities are obtained. An often-used method which makes it possible to reduce such variations is the Tikhonov-method.^{21–23} Within this method, the quantity $\|A \cdot x - b\|^2 + \alpha^2 \|x\|^2$ is minimized. Here the symbol $\|\cdot\|$ refers to the 2-norm of the vector and α is a parameter which controls the weight given to a penalty term $\alpha^2 \|x\|^2$. We have employed this “regularization” method, again including a non-negativity constraint. In the $\alpha = 0$ limit, the Tikhonov method thus reduces to the non-negativity-constrained χ^2 -method. Although the dipole weights can still have any positive value, strong variations are damped by the inclusion of the penalty term. This is known as the zeroth-order Tikhonov approach. Higher (n th) order approaches have been defined, by substituting $\|x\|$ with the 2-norm of the n th-order derivative of x . However, we restrict the discussion here to the zeroth-order approach. In practice, a trade-off will arise between the minimization of $\|A \cdot x - b\|^2$ and of $\|x\|^2$. The optimum value of α is then often chosen as the value at the corner of the L-shaped curve connecting the optimal $\{\|A \cdot x - b\|^2, \|x\|^2\}$ points as calculated as a function of α . The corner is defined as the point of maximum curvature of this curve. This is known as the “L-curve criterion”.²³ An example of this approach will be given below (Fig. 3.3). The optimization procedure used within the Tikhonov method is similar to the one described by equations 6.1 - 3.4 and 3.6, but the χ^2 error is given by:

$$\begin{aligned} \chi^2 \equiv & \sum_{i=1}^M \sum_{j=1}^N \sum_{s,p} \{I_{\text{norm},s(p)}^{\text{calc,trial}}(\lambda_i, \theta_j) - I_{\text{norm},s(p)}^{\text{expt}}(\lambda_i, \theta_j)\}^2 \\ & + \alpha^2 \sum_{k=1}^Q (x_k)^2. \end{aligned} \quad (3.7)$$

where Q is the total number of dipoles considered. A grid point distance of 1 nm is used throughout this chapter, with the first and last grid points at 8 nm distance from the electrodes. The dipole intensities x_k are normalized such that their sum is equal to 1.

3.3 Spatial resolution - four case studies

In this section we analyze the spatial resolution with which the emission profile can be determined for four cases, schematically represented in figure 3.1. In all cases a 160 nm thick emissive layer is present in between glass/ITO/PEDOT:PSS (anode) and Ba/Al (cathode) layers, with the same layer thicknesses and refractive index functions as used in the previous section (and taken from Ref. 20). The figure gives the profile distributions as a function of the distance from the PEDOT:PSS/(emitting layer) interface. The first case (a) deals with emission from a delta-function shaped profile, i.e. an infinitely narrow zone located at a distance z_1 from the anode. In the second case (b) a single-peaked, broad emission profile similar to those deduced earlier from the analysis of blue polymer OLEDs (ref. 20, 26) is analyzed. Case (c) deals with a emission from multiple regions, described as two delta-like profiles located at a distance z_1 and z_2 from the anode. Case (d) considers the possibility to have a uniform emission profile over a narrow region. The last two profile shapes could be generated, for example, at the organic-organic interface in multilayer devices (c) or in between interfaces (d). In all cases an ensemble of 100 artificial “experimental datasets” (b-vector, see section 4.2) is created by adding Gaussian noise to the calculated emission spectra. Following the experimental precision and accuracy analysis given in appendix, 2 % random noise is used for case (b), and 5 % random noise is used for the other cases. In the appendix, it is also shown how the experimental conditions are optimized in order to avoid or drastically reduce systematic errors. In each case, the FP and the Tikhonov methods are applied to the complete ensemble of artificial experimental data, in order to be able to determine the resolution with which the light-emission profile can be reconstructed.

3.3.1 Emission at one interface: delta-function shaped profile

In order to study the ultimate achievable resolution we consider as a first case the emission from a single dipole position in the emissive layer, i.e. from a delta-function shaped emission profile. Such a profile can arise in a bilayer OLED due to emission from charge-transfer excitons which are confined to the interface, when the electron and hole transport layers are at the same time are hole and electron blocking, respectively.

First, we have analyzed the accuracy with which the profile can be reconstructed using the fit profile method, assuming a Gaussian profile with a peak shift Δ (as defined in the inset of figure 3.2(a)) and the peak width as free parameters. Figure 3.2(a) (full spheres) shows the ensemble-averaged value of the

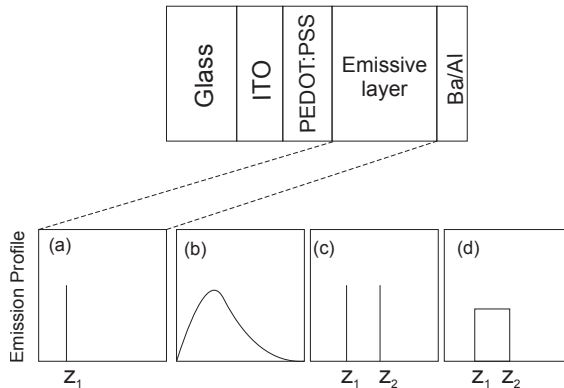


Figure 3.1: Schematic representation of the four emission profile cases analyzed. (a) Delta-function shaped emission profile, located at a distance z_1 from the anode. (b) Broad single-peaked emission profile as obtained for a realistic device.^{20,26} (c) Double delta-function shaped emission profile, with peaks at a distance z_1 and z_2 from the anode. (d) Rectangular emission profile, located in the range $z_1 - z_2$ from the anode.

peak shift (error) Δ as a function of the distance to the anode. The grey regions give the 99.6% confidence interval on the peak position error. A positive error corresponds to a peak position further from the anode as compared to the real peak position. It is found that in all cases the error is of the order of 1 nm, and smallest at a distance of 120 nm from the cathode (40 nm from the anode). For dipoles located close to the cathode the error gets larger, although the uncertainty is still always less than 3 nm. For dipoles more close to the anode, the error increases only slightly. An otherwise identical calculation for a 320 nm device revealed the same position dependence of the error in the peak position and uncertainty interval in the region within 120 nm from the cathode. The error and its uncertainty were found to stay significantly smaller than 1 nm for larger distances from the cathode.

Figure 3.2(b) describes the results obtained using the Tikhonov method with $\alpha = 0$. The method reduces in this case to a non-negativity constrained χ^2 -method. No regularization is used, as that would widen the profile. As noted above, the analysis was done for a discrete set of dipole positions at a 1 nm mutual distance. The determined emission profiles obtained for emission at three different distances from the anode are given. The peak position is in all cases retrieved within 1 nm, and the width of the profile is almost equal to the 1 nm distance between the dipole positions used. The resolution is thus in this case essentially as good as that of the FP-method. However, it may be noted that artifacts in the form of additional peaks are present very close to the cathode. Their weight increases if the actual emission position approaches the cathode (see figure 3.2(b)). This intensity may be explained as a result of the very small outcoupling efficiency close to the cathode, so that the χ^2 function is almost insensitive to spurious high dipole intensities near the cathode.

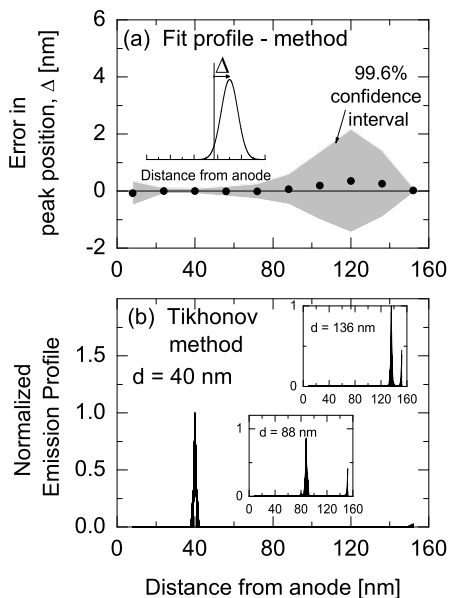


Figure 3.2: Single-delta profile resolution. (a) Fit-profile method results. Error in the peak position determination, Δ , defined as in the inset, as a function of the distance of the emitting plane from the anode. The full dots indicate the average over 100 noise configurations, while the grey region describes a 99.6% confidence interval. (b) Tikhonov-method results, with $\alpha = 0$, for emission at three different distances (d) from the anode.

3.3.2 Broad emission profile

In single-emissive-layer devices, a broad and single-peaked emission profile is expected, as observed e.g. for the case of blue and red emitting polymer OLEDs²⁰ and as predicted from drift-diffusion-recombination modelling.^{4,26,27} In this subsection, the ensemble of artificial data is based on the emission profile for a 160 nm thick blue-emitting OLED, driven at 18 V, as obtained in the framework of the study presented ref. 26. Figure 4(f) of that chapter shows the voltage dependence of the emission profile deduced. The profile was described in terms of its peak position, peak width and peak asymmetry in a manner described in Ref. 20. The same three-parameter approach is also used in this chapter when employing the FP-method. The emission profiles obtained using the FP and Tikhonov methods are given in figure 3.3(a) and 3.3(b-d), respectively.

Figure 3.3(a) shows that the ensemble of 100 reconstructed profiles as obtained from the FP method reveals that the uncertainty resulting from the 2% random

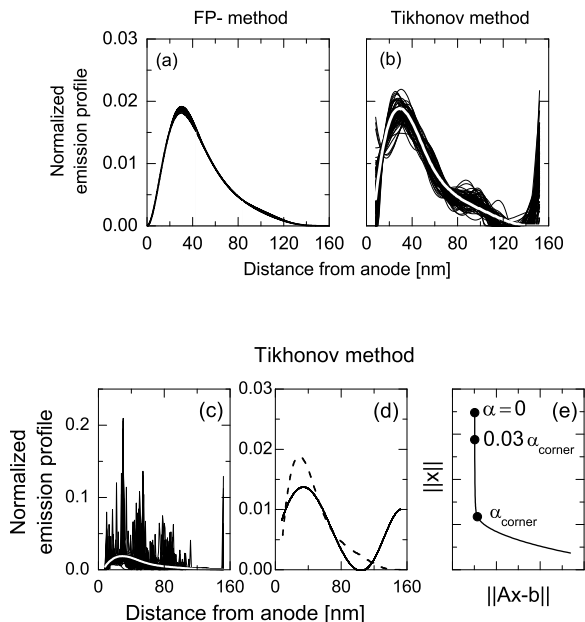


Figure 3.3: Reconstructed emission profiles for a broad single-peaked profile case, for a profile determined for a 160 nm thick blue-emitting OLED, driven at 18 V, as obtained using the FP-method (a) and as obtained using the Tikhonov method with regularization parameter $\alpha = 0.03 \cdot \alpha_{\text{corner}}$ (b), $\alpha = 0$ (c) and $\alpha = \alpha_{\text{corner}}$ (d), with α_{corner} as deduced from the L-curve (e). The original profile coincides with the average of the profiles shown (a), is given in white (b,c) or is given as a dashed curve (d).

noise included is very small. The original profile (not shown) coincides with the average of the curves displayed. The original profile can thus be reconstructed with nanometer-scale resolution, as concluded already in ref. 20. In figure 3.3(b) the results for the Tikhonov method with a relatively small regularization parameter ($0.03 \times \alpha_{\text{corner}}$) are presented, and figures 3.3(c) and (d) show the results obtained using the Tikhonov approach using $\alpha = 0$ and $\alpha = \alpha_{\text{corner}}$, i.e. at the corner point of the L-curve, shown in figure 3.3(e). In the absence of regularization (figure 3.3(c)), the resulting profiles show huge point-to-point variations, unlike the smooth original profile (white curve). A non-zero value of α , but still smaller than the corner-point value (figure 3.3(b)), gives rise to an ensemble of profiles which describe, on average, the original profile. However, additional intensity arises near the cathode, an artifact which was already visible for the $\alpha = 0$ case and which was also found for emission from a delta-function profile in the previous subsection. When α is equal to the corner-point value (figure 3.3(d)), the point-to-point variations have essentially vanished. However, the original profile (dashed) is not correctly retrieved. It is too wide near the peak, and the recon-

struction shows an even more strong intensity near the cathode than as obtained using less regularization.

We conclude that it is within the Tikhonov method not trivial to choose the most appropriate value of the optimization parameter. The non-regularized profiles are very noisy and provide little information about the original profile, showing (at best) that the emission originates from a region more close to the anode, whereas the profiles obtained for α_{corner} produce a strong artifact close to the cathode. The use of an α value in between zero and the corner point seems in this case to be preferable, provided that a large ensemble of nominally identical experimental data sets would be available. The analysis shows that even without such an additional effort the FP method already gives rise to a very accurate reconstructed profile.

3.3.3 Emission at two interfaces

In efficient multilayer OLEDs the recombination and emission takes place in a central layer, sandwiched in between hole transporting and electron transporting layers which are blocking for electrons and holes, respectively. In the case of well-balanced electron and hole mobilities, charge accumulation at the two internal interfaces can give rise to recombination which is strongly localized at these interfaces. We investigate here to what extent the emission from the two interfaces can be resolved experimentally. For that purpose, we consider a double delta-function shaped emission profile from two positions in the 160 nm thick emissive layer, viz. from a first interface at 24 nm from the anode, and from a second interface at 40 nm, 56 nm or 72 nm from the anode. We consider thus emission from the region in the OLED for which from the analysis given in section 3.3.1 the highest resolution is expected. Equal intensities for the emission from both interfaces are assumed. The three cases have been studied using the FP-approach and using the Tikhonov approach with $\alpha = 0$. The results are given in figure 3.4(a-c) and 3.4(d-f), respectively, which in all cases show a superposition of all reconstructed profiles as obtained for an ensemble of 100 artificial datasets.

Using the FP-approach, the presence of the two separate peaks can be retrieved when their distance is 24 nm or larger (figures (a) and (b)). When their distance is 16 nm (case (c)), the spread in the peak distribution is so large that the two peaks cannot be distinguished anymore. Using the Tikhonov-method it is in all cases possible to resolve the presence of two distinct peaks, even at an distance as small as 16 nm, although in this case the profiles obtained start to show additional smaller peaks in the region in between the two interfaces and although (as observed also above) additional intensity is found close to the cathode.

We conclude that for this case the ultimate resolution is not as good as would be expected from the resolution obtained for the case of a single delta-function shaped profile studied in section 3.3.1, and that the Tikhonov approach shows in this case a somewhat better resolution.

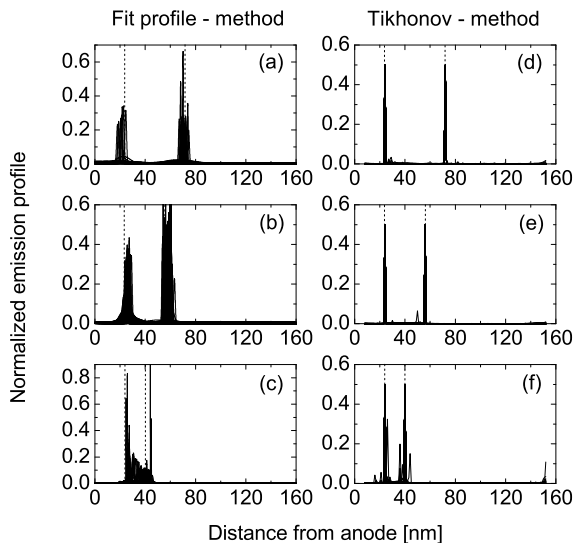


Figure 3.4: Light-emission profiles as determined using the FP (a-c) and Tikhonov (d-f) approaches for emission at a distance of 24 nm (fixed) and 72 (a,d), 56 (b,e) and 40 nm (c,f) from the anode, indicated by dashed lines.

3.3.4 Uniform emission in between two interfaces: rectangular profile

In multilayer OLEDs such as considered in the previous subsection, the emission from the central emissive layer can also be uniform. The emission profile is then rectangular. It may be shown from drift-diffusion-recombination device modelling that such a situation arises if the mobility in the transport layers is much larger than the mobility (for both carriers) in the emissive layer, if the mobility is constant and equal for electrons and holes, and if charge-carrier diffusion may be neglected. Designing OLEDs such that the emission originates from the entire emissive layer, instead of from the interface regions, is expected to give rise to an enhanced operational lifetime. It is therefore of interest to be able to distinguish experimentally emission from the rectangular profile assumed from emission originating from the two interface regions. We consider uniform emission from a range 36 to 44 nm from the anode.

Within the fit-profile analysis we try to reconstruct the profile by describing it as a superposition of a rectangular profile and two delta-function peaks (see figure 3.5(a)). All 100 artificial datasets were found to lead, within 1 nm, to the correct original value of the boundary positions of the profile. Furthermore, the weight (w_3 given to the rectangular component was found to be on average very

large, viz. $87 \pm 11\%$, and the average weights of the two delta-function peaks at the interfaces (w_1 and w_2) were almost equal quite small, as shown in the figure. The FP-approach is thus able to provide a quite accurate picture of the recombination process, being distributed uniformly over the emissive layer instead of being peaked at the interfaces.

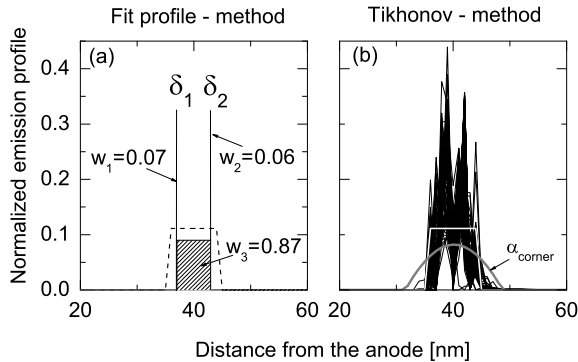


Figure 3.5: Reconstruction of a rectangular light-emission profile. (a) Results of the fit-profile method, indicating the average weights w_1 and w_2 obtained for the two assumed delta-function emission peaks at the interval edges and the average weight w_3 for the uniform emission profile. The edge positions are $\delta_1 = 36$ nm and $\delta_2 = 44$ nm are almost perfectly retrieved. Original profile: dashed curve. (b) Results of the Tikhonov method, indicating in black the ensemble of profiles obtained without regularization ($\alpha = 0$), and in grey a single profile obtained after regularization using L-curve corner point α_{corner} . Original profile: white curve.

Analyzing the same ensemble of 100 artificial datasets with the Tikhonov approach, the results shown in figure 3.5(b) are obtained. The original profile is here represented in white, while the ensemble of reconstructed profiles as obtained without regularization ($\alpha = 0$) is shown in black. It is found that the width and the position of the rectangle are correctly retrieved. The reconstructed emission zone coincides almost completely with the original 36-44 nm emission zone. However, the uniformity of the emission is not retrieved. Instead, a rather noisy profile is in all cases obtained. Furthermore, also (again) some intensity is found near the cathode (not shown). In grey, we give for a specific dataset the L-curve corner profile; the other datasets yield almost identical profiles. Regularizing the solution thus smoothes the curve, however at the expense of a loss of sharpness in the profile.

3.4 Conclusions

The resolution limits of two inverse-problem solving approaches for reconstructing the light-emission profile from experimentally collected electroluminescence spectra in OLEDs were investigated. The fit-profile (FP) method is based on a parameterized emission profile, while the Tikhonov method produces profiles free of any assumption concerning the shape. The only constraint is the non-negativity of the solution. After analyzing the experimental precision and accuracy, both methods have been applied to four cases: a delta-function shaped profile as may be obtained for a bilayer OLED, a broad single-peak profile as may be obtained for a single-layer OLED, a double delta-function shaped profile and a rectangular profile as may be obtained for a multilayer OLED.

In the two narrow emission profile cases studied (single and double delta-function shaped profiles) we have found nanometer-scale resolution of the peak positions for both approaches, with the non-regularized Tikhonov method ($\alpha = 0$) leading to a better resolution for the double-delta-function shaped profile. In the two broad emission profile cases studied (broad single-peak profile and rectangular profile) we have found that the FP-approach provides accurate reconstructions with nanometer-scale resolution. In such cases the Tikhonov approach quite accurately provides unbiased information about the region in the device from which the emission predominantly originates. However, the profiles obtained show strong point-to-point intensity variations which can only be damped out by means of regularization at the expense of a loss of sharpness or resolution. Furthermore, in all four cases the Tikhonov method gives rise to intensity artifacts near the cathode, in particular when using strong regularization. We note that the resolution limits given were based on conservatively chosen experimental noise levels, and that the development of lower-noise measurement techniques could give rise to further improved resolution.

For the case of wide emission profiles for which the shape is not *a priori* known, an improved method would consist of a two-step Tikhonov-FP approach. The FP approach provides high resolution if the parameterized function describing the profile is sufficiently constrained so that non-physical point-to-point variations are avoided, but also sufficiently flexible. As it is not always clear what the optimal parameterization should actually be, it would be helpful to have unbiased additional information available on the shape of the profile. The Tikhonov-method provides such information. For example, for the emission profile studied in section 3.3.2, it strongly suggests that the profile has the shape of a single broad peak located close to the anode. Thereby, alternative solutions such as a double-peaked profile can be excluded. For the emission profile studied in section 3.3.4 the results obtained from the Tikhonov method show that the emission is confined to the region in between the two interfaces, thus excluding major contributions due to emission elsewhere. Such contributions can often not be excluded *a priori*, as that will depend on the effectiveness of the electron or hole blocking at the interfaces. A two-step approach, consisting of (i) a pre-analysis using the Tikhonov method in order to determine an appropriate parameterized fit function and (ii) application of the FP method, is therefore expected to improve the resolution.

3.5 Appendix

Experimental precision and accuracy

In this appendix we discuss the systematic and random errors which can occur in the measurement of the electroluminescence spectra. They determine the ultimate resolution of the light-emitting profile reconstruction methods discussed. For this purpose, we have carried out a study of the measurement uncertainties for the case of a blue-emitting polymer-based OLED. The layer stack is, from anode to cathode: glass (1 mm) / ITO (125 nm) / PEDOT:PSS (100 nm) / PF-TAA (100 nm) / barium (5 nm) / aluminum (100 nm), where the light-emission takes place in a polyfluorene-7.5 wt.% triarylamine co-polymer (PF-TAA) with a structure which is presented in ref. 20. The refractive index functions of the layers included are also given in ref. 20. We regard the results of the analysis as representative and also applicable to (for example) small-molecule based white multilayer OLEDs.

The angular-dependent emission spectra have been measured using a Melcher Autronic DMS system. A schematic drawing of the experimental set-up is shown in figure 3.6. We measure the radiance emitted by a pixel via a light collection system composed of two diaphragms and a lens which focuses the collected light on the entrance of an optical fiber, mounted on a mechanical arm which can rotate around the pixel, describing an angle θ . A polarizer is mounted between the sample and the first diaphragm, which fixes the opening angle to 2° . By changing the size of the second diaphragm, closer to the fiber, one can change the size of the observed spot on the sample. The distance from the OLED pixel to the objective lens is approximately 15 cm. A glass hemisphere (radius 4 cm) is mounted on top of the glass substrate (1 mm), separated by an index matching fluid (dashed line in the figure). It can be demonstrated that such a large value for the hemisphere radius, much larger than the pixel size which is at most 1 mm, prevents curvature distortion effects on the collected angular-dependent spectra.

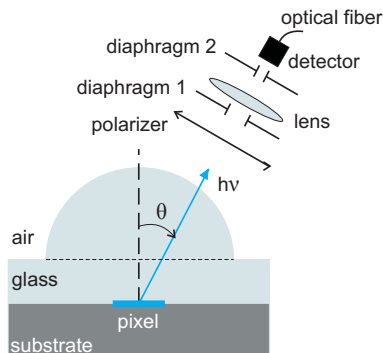


Figure 3.6: Schematic of the experimental set-up. Light emitted through the glass side of OLEDs is coupled into an optical fiber through a double-diaphragm system. The light collection system can rotate describing an angle θ .

The use of small pixels greatly facilitates the alignment of the sphere with respect to the center of the observed spot. However, the finite pixel size can also be a cause of systematic errors, viz. when the measurement conditions are such that the area as seen by the detector is determined in part by the finite size of the OLED. Three measurement regimes can be distinguished, depending on the ratio between the observation spot diameter d (in glass and at $\theta = 0^\circ$) and the size l of the square OLED pixel, $r \equiv d/l$. In order to investigate the occurrence of systematic errors, the three regimes have been studied by carrying out measurements without and with the glass hemisphere. The pixel size was $l = 1$ mm, and the spot diameter in air was equal to 0.2, 1.0 and 3.0 mm, i.e. $d = 0.13, 0.67$ and 2.0 mm, using $n = 1.5$ as the refractive index of glass. For the cases where $r = 0.13$ and 2.0 (i.e. $d = 0.13$ mm and 2.0 mm) the spot size is for all emission angles smaller and larger than the pixel size, respectively, whereas for the intermediate $r = 0.67$ case the spot as seen without the hemisphere just falls within the pixel for normal emission but becomes at finite emission angles immediately larger than the pixel size. Figure 3.7 (symbols) shows the measured ratio η between the “emission in air” (i.e. measured without a hemisphere), P_{air} , and the “emission in glass” (i.e. measured using a glass hemisphere), P_{glass} , for a selected wavelength and for the three measurement regimes mentioned above. The result was found to be wavelength-independent. The results are given as a function of the polar emission angle in glass. In the experiments without a hemisphere, the highest value, 38.8° , gives rise to emission at 70° in air. In the figure, these intensities are compared to the intensities measured with a hemisphere in the range (in glass and in air) up to 38.8° . For the three measurement regimes, a different angular- and polarization-dependence is expected for η . This is confirmed by the results of emission calculations including the angular dependent Fresnel refraction and reflection at the glass-air interface and including for the $r = 0.13$ and 0.67 cases the finite pixel size effect by means of a ray-tracing approach (solid curves).

The theoretical results at 0° can be understood as follows. After transmission from the glass substrate to the air, the emission solid angle increases by a factor n^2 . On the other hand, the observed spot area in the glass is reduced by a factor n^2 if the spot is much smaller than the pixel size used. Overall, this leads to a ratio $\eta = 1$, in agreement with the observed $r = 0.13$ result. When the spot size in glass is larger than the pixel size, the ratio η reflects purely the solid angle increment. Its effect is not compensated by a spot size increase, so that $\eta = 1/n^2 \simeq 0.44$, in agreement with the observed $r = 2.0$ result. For an intermediate value of the spot radius, η is at 0° found to be slightly smaller than predicted. We interpret this as a result of a somewhat decreased emission intensity from the region close to the pixel boundary. This can affect the intensity observed in air, as the 1 mm spot radius in then equal to the size of the square pixel, but not the intensity observed in the case of emission in glass, as the observed spot size in glass is then only 0.67 mm, well below the pixel size.

For higher emission angles, the calculations accurately describe the small-spot case ($r = 0.13$), whereas for the large-spot case ($r = 2.0$) the experimental curves deviate at high angles (larger than $\sim 30^\circ$) somewhat from the calculated curves.

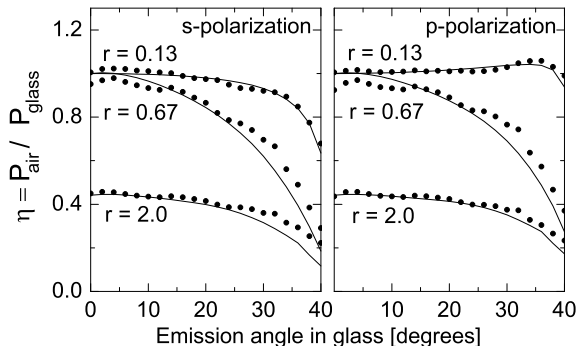


Figure 3.7: Calculated (solid curve) and experimental (symbols) value of the ratio η between the power emitted in air and the power emitted in glass, as a function of the emission angle in glass, for s -polarized and p -polarized light, as indicated on the figure. Three possible measurement conditions are investigated, described by the ratio $r = d/l$ between the diameter of the observation spot, d , and the size of the squared pixel, l .

We will discuss two factors which play a role, both related to the finite (1 mm) thickness of the glass substrate: multiple reflection in the glass substrate and parallax alignment errors. Multiple reflection in the glass substrate leads to a “light recycling effect”: in the case of a large spot size light which is reflected at the glass/air interface and subsequently to a point outside the OLED pixel can finally still be collected. It should be noted that the OLED pixel size is determined by the size of the patterned ITO anode, whereas the emissive layer and the reflecting cathode are not patterned. The effect is expected to increase with increasing angle, consistent with the observations. In the ultimate limit (multiple reflections with large reflection coefficients), finally all light would be collected, irrespective of the polarization. This may explain why for the large-spot case at high angles the experimental curves are for both polarizations more similar than as calculated (without taking multiple reflection effects into account). The influence of multiple reflections is expected to be less in the small-spot case, consistent with the results shown in the figure.

Second, we consider possible systematic errors due to a parallax error in the alignment of the spot center with respect to the pixel center. As a result of the finite thickness of the glass substrate, the actual position of the spot center varies slightly with respect to the OLED pixel center with increasing emission angle. This parallax error can be minimized as follows. First, perfect alignment and focus (height adjustment) is created for $\theta = 0^\circ$. Subsequently, perfect spot angle alignment is realized at the highest polar angle included by a slight height adjustment (while keeping the lateral alignment the same). Although this introduces a small defocus, it strongly reduces the spot center alignment error. We have

experimentally and theoretically investigated the remaining effect as a function of the glass substrate thickness. The effect is absent in the large spot-size case. For the small spot-size case it becomes larger with increasing glass thickness. However, for all cases shown in Fig. 3.7 (1 mm substrate) the remaining effect is found to be negligible. In conclusion, in order to minimize systematic errors the glass substrate thickness should be taken sufficiently small. For a small spot-size this will reduce remaining parallax errors, whereas for a large spot size this will reduce errors related to multiple reflection.

In general, systematic errors may also be introduced by errors in the wavelength dependent complex refractive index functions of the materials present in the OLED stack. To a certain extent it is possible to detect such errors by minimizing the χ^2 function with respect to the thickness of the layer for which the refractive index is uncertain. We furthermore stress that although such errors would lead to an error in the absolute position of the light-emission profile, the resolution with which various other relevant predictions can be made, such a shift in the emission profile with the OLED driving voltage, is not or only weakly affected.

In order to determine random errors affecting the accuracy of the measurements, we have investigated the reproducibility of the experimental spectra obtained for the same OLED as studied above. The spread between nominally identical measurements is found to be slightly angle, wavelength and polarization dependent. The error is smaller for higher emission intensities. At low voltages the ultimate measurement accuracy is determined by the occurrence of slow drift in the emission intensities during the large total measurement times needed, which limits the total data accumulation time to in practice a few hours. The highest errors are then obtained in the low-intensity parts of the spectrum and at large angles. For the blue OLEDs studied at a low brightness (4 cd/m^2 at 0°) the highest error is in the range 2-4% (defined here and below as the standard deviation of the intensity distribution), as obtained for p -polarized light in the 550-600 nm wavelength range and in the $55\text{-}70^\circ$ polar angle range. Outside this angle and wavelength range, the error is well below 1.5%. Also at high voltages, the ultimate measurement accuracy is determined by the drift, which is now much faster due to the larger effect of self-heating. However, much shorter measurement times are then feasible due to the larger signal. A conservative estimate of the resulting random intensity error is 2%. We use this error in our analysis of resolution limits of the emission profile for the blue OLEDs in section 3.3.2. In the other case-studies presented in section 4.4 we assume, even more conservatively, 5% random errors.

3.6 References

1. *Nat. Photon. Technology Focus* **3**, 8 (2009).
2. S. Reineke, F. Lindner, G. Schwartz, N. Seidler, K. Walzer, B. Lüssem and K. Leo, *Nature* **459**, 234 (2009).
3. K. H. Kuma, Y. Jinde, M. Kawamura, H. Yamamoto, T. Arakane, K. Fukuoka, C. Hosokawa, *Society for Information Display (SID) Symposium Digest of Technical Papers* **38**, 1504 (2007).
4. S. L. M. van Mensfoort, J. Billen, M. Carvelli, S. I. E. Vulto, R. A. J. Janssen and R. Coehoorn, *J. Appl. Phys.* **109**, 064502 (2011).
5. J. J. M. van der Holst, F. W. A. van Oost, R. Coehoorn and P. A. Bobbert, *Phys. Rev. B* **80**, 235202 (2009).
6. M. Kuik, H. T. Nicolai, M. Lenes, G.-J. A. H. Wetzelaer, M. Lu and P. W. M. Blom, *Appl. Phys. Lett.* **98**, 093301 (2011).
7. G.-J. A. H. Wetzelaer, M. Kuik, H. T. Nicolai and P. W. M. Blom, *Phys. Rev. B* **83**, 165204 (2011).
8. C. W. Tang, S. A. VanSlyke and C. H. Chen, *J. Appl. Phys.* 3610 (1989).
9. M.-H. Lu and J. C. Sturm, *J. Appl. Phys.* **91**, 595 (2002).
10. W. M. V. Wan, N. C. Greenham and R. H. Friend, *J. Appl. Phys.* **87**, 2542 (2000).
11. J.-S. Kim, P. K. H. Ho, N. C. Greenham and R. H. Friend, *J. Appl. Phys.* **88**, 1073 (2000).
12. T. Granlund, L. A. A. Pettersson and O. Inganäs, *J. Appl. Phys.* **89**, 5897 (2001).
13. J. M. Leger, S. A. Carter, B. Ruhstaller, H.-G. Nothofer, U. Sherf, H. Tillman and H.-H. Hörhold, *Phys. Rev. B* **68**, 054209 (2003).
14. H. Kuma, H. Tokairin, K. Fukuoka and C. Hosokawa, *Society for Information Display (SID) Symposium Digest of Technical Papers* **36**, 1276 (2005).
15. M. Roberts, *Proc. of OEC-06* 1 (2006).
16. B. Ruhstaller, T. Flatz, M. Moos, G. Sartoris, M. Kiy, T. Beierlein, R. Kern, C. Winnewisser, R. Pretot, N. Chebotareva, and P. van der Schaaf, *SID Symposium Digest of Technical Papers* **38**, 1686 (2007).
17. M. C. Gather, M. Flämmich, N. Danz, D. Michaelis and K. Meerholz, *Appl. Phys. Lett.* **94**, 263301 (2009).
18. B. Perucco, N. A. Reinke, D. Rezzonico, M. Moos and B. Ruhstaller, *Opt. Expr.* **18**, A246 (2010).
19. Software SETFOS by Fluxim AG, Switzerland, www.fluxim.com
20. S. L. M. van Mensfoort, M. Carvelli, M. Megens, H. Greiner, D. Wehenkel, M. Bartyzel, R. A. J. Janssen and R. Coehoorn, *Nat. Photon.* **4**, 329-335 (2010).

21. A. N. Tikhonov and V. Y. Arsenin, *Solutions of Ill-Posed Problems* (Winston, Washington, DC, 1977).
22. R. C. Aster, B. Borchers and C. Thurber, *Parameter estimation and inverse problems*, (Academic Press, New York, 2004).
23. P. C. Hansen, *Discrete Inverse Problems* (SIAM, Philadelphia, 2010).
24. H. Greiner and O. J. F. Martin, *Proc. of SPIE* **5214**, 249 (2004).
25. Matlab Optimization Toolbox, The MathWorks, Inc.
26. M. Carvelli, R. A. J. Janssen and R. Coehoorn, *Phys. Rev. B* **83**, 075203 (2011).
27. S. Harkema, R. A. H. J. Kicken, B. M. W. Langeveld-Voss, S. L. M. van Mensfoort, M. M. de Kok, R. Coehoorn, *Organ. Electr.* **11**, 755 (2010).

Determination of the exciton singlet : triplet ratio in single-layer organic light-emitting diodes

*The efficiency of fluorescent organic light emitting diodes (OLEDs) is strongly affected by the fraction of singlet excitons formed. While the standard statistical value of the singlet : triplet ratio is 1 : 3, significant deviations have been reported for several materials, in particular for polymers. After having introduced a method to reconstruct the light-emission profile and having shown its resolution limits, we exploit the method to extend an approach first introduced by Segal et al. (Phys. Rev. B **68**, 075211 (2003)) to determine the singlet fraction with high accuracy for organic semiconductors in single-layer OLEDs. The analysis is based on a combination of electroluminescence (EL) and reverse bias photoluminescence (PL) measurements. We carefully determine from a combined experimental and modeling approach the PL and EL emission profiles and light outcoupling efficiencies, which are generally quite different for single layer devices. The approach is demonstrated for the case of OLEDs based on a blue-emitting polyfluorene-based copolymer, for which the singlet fraction is found to be in the range 10-25%, increasing with increasing emitting layer thickness but independent of the applied voltage. The analysis is then extended to devices based on different polyfluorene-copolymers and to poly (phenylene vinylene), in order to investigate the possible limitations of the approach.**

*Part of the work presented in this chapter has been published: M. Carvelli, R. A. J. Janssen and R. Coehoorn, *Phys. Rev. B* **83**, 075203 (2011).

4.1 Determination of the exciton singlet : triplet ratio

In the past decade, various experimental studies have indicated that the singlet exciton formation yield, η_S , in organic light-emitting diodes (OLEDs) can significantly exceed the quantum statistical value of 25%, in particular for polymers.^{1–10} It has been suggested¹¹ that polymer OLEDs based on fluorescent organic semiconductors may therefore become as efficient as phosphorescent OLEDs, within which the otherwise non-radiatively decaying triplet excitons are harvested by making use of heavy-metal containing co-deposited molecules or co-polymerized units. The latter method has made it possible to achieve a near-100% internal quantum efficiency in monochrome small-molecule OLEDs,^{12,13} a factor of four larger than in fluorescent devices with a singlet : triplet ratio equal to 1 : 3. However, the issue of the singlet fraction in polymers is still a matter of debate, based on experimental results showing that it is only around 20% for the archetype poly (phenylene vinylene) (PPV)-based polymer MEH-PPV,⁷ on more general considerations of the observed external quantum efficiency of fluorescent polymer OLEDs,⁷ and on an experimental study which suggests that in a relevant polymer no singlet-triplet interconversion takes place in the exciton precursor (bound polaron pair) states.¹⁴ The occurrence of such interconversion processes is regarded as a crucial condition for obtaining an enhanced singlet fraction.^{15–19}

In Table 4.1 an overview is given of the singlet fractions as measured for selected polymers. The methods used may be classified in the following way. The perhaps most direct method (A) involves a determination of the external electroluminescence (EL) quantum efficiency of a complete OLED, η_{EL} , the electron-

Table 4.1: Overview of measured values of the singlet fraction η_S for selected polymers, and of the methods (see the text) used.

Polymer	η_S [%]	Method	Reference
OC ₁ C ₁₀ – PPV	> 50	B,a,I	1
	> 35 – 45	A,a,I	2
	83 ± 7	D,a,I	5
Green PPV ^a	> 35 – 45	A,a,I	2
MEH-PPV	47	E,d,I	3
	20 ± 4	C,b,I	7
PtOEP	57 ± 4	D,a,II	4
	60	E,d,II	9
polyoctylfluorene (PFO)	57	E,d,I	3
	70	D,c,I	8
polyspirobifluorene	44 ± 4	D,a,I	10
PF-TAA	10 – 25	C,a,I	this chapter

^a 2-alkoxyphenyl-PPV-co-2,5-dialkoxy-PPV

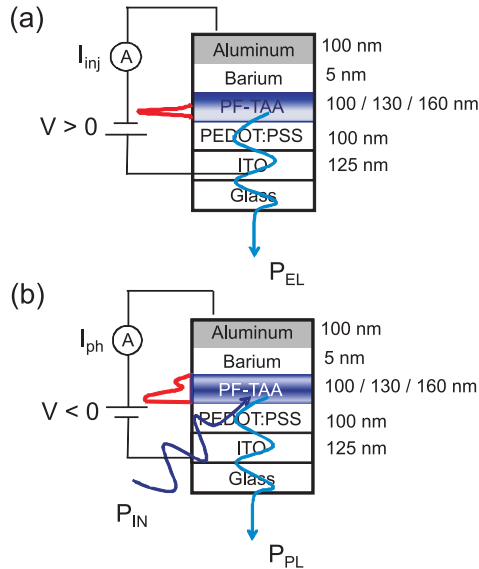


Figure 4.1: Schematic representation of the method employed to determine the exciton singlet : triplet ratio. The same experimental set-up is employed to measure the electroluminescence (a) and photoluminescence (b) at positive and negative voltages, respectively. Combined experimental and modeling approaches are used to calculate the different EL and PL light-emission profiles (shown schematically in the figures), and the resulting different light-outcoupling efficiencies. The layer stack is described in more detail in Section 4.2.

hole recombination efficiency, η_{rec} , the radiative decay efficiency, η_{rad} , and the EL light-outcoupling efficiency, $\eta_{\text{out,EL}}$, using $\eta_{\text{S}} = \eta_{\text{EL}} / (\eta_{\text{rec}} \eta_{\text{rad}} \eta_{\text{out,EL}})$. The photoluminescence (PL) quantum yield of single layers on a supporting substrate may be used to estimate η_{rad} . Other methods involve measurements under forward bias of the EL and PL efficiencies of the same device (B), measurements of the EL efficiency and the voltage dependence of the PL efficiency under reverse bias (C), EL and PL measurements of the singlet and triplet densities and their dynamics (D), and optical probing of the effect on the density of photogenerated polarons of resonant microwave radiation, which equalizes the density of singlet and triplet bound polaron pair states (E). Application of the latter two methods requires measurements at cryogenic temperatures, typically 100 K or below, whereas the other methods are applicable at any temperature. These methods have been applied to complete single layer (a) or multilayer (b) OLEDs, on single layers in between non-injecting electrodes (c), or on single layers on a supporting substrate (d). The materials used were in most cases genuine fluorescent emitters (I), but contained in some studies heavy metal atoms (Pt) in order to enhance the emission from triplet excitons (II).

Deducing η_{S} from the absolute EL quantum efficiency (method A) can lead to a relatively high uncertainty. This source of uncertainty is eliminated in methods

B-D, which are based on the relative EL and PL intensities measured in the same setup. Within method C, a further refinement is introduced, viz. by normalizing the EL intensity by the measured forward current and by normalizing the measured voltage-induced *change* of the PL intensity as measured under reverse bias by the resulting photocurrent. We note that a method for deducing η_S from device-studies involving combined EL and PL measurements was already introduced by Kalinowski and co-workers.^{20–22} However, in that work, on anthracene and tetracene single crystals, no normalization by measured current densities was employed. For the case of OLED structures, the application of methods B-D would (in general) require that a microcavity model is used, as it is possible that the PL and EL light-outcoupling efficiencies are different, resulting from different shapes of the light-absorption and resulting re-emission profile (in PL) and the emission profile (in EL). This issue has been recognized by several authors. In the work of Segal *et al.* (method C),⁷ which for MEH-PPV gives rise to a value of η_S which is quite close to the quantum-statistical value, this uncertainty has been strongly reduced by making use of layered OLEDs containing only a relatively thin emissive layer which is well separated from the electrodes, so that the PL and EL outcoupling efficiencies are almost equal. However, when studying more simple single-layer OLEDs, this issue should be taken into account.

In this chapter, we investigate in detail the difference between the PL and EL emission profiles in single layer OLEDs, making use of a recently developed method for accurately determining the EL emission profile from the angular, wavelength and polarization-resolved emission intensities,²³ and employ this to deduce η_S for single-layer OLEDs using the combined forward bias EL and reverse bias differential PL method introduced by Segal *et al.*⁷ Figure 4.1 shows in a schematic way the method used. In the same setup, a measurement is carried out of the EL intensity P_{EL} (in arbitrary units) per unit of the injected current I_{inj} (figure 4.1(a)), and of the *decrease* of the PL intensity due to field-quenching under reverse bias conditions P_{PL} (in the same arbitrary units) per unit of *increase* of the corresponding photocurrent I_{ph} (figure 4.1(b)). The singlet fraction is expected to be equal to the ratio of these two quantities if the EL and PL light outcoupling efficiencies, $\eta_{out,EL}$ and $\eta_{out,PL}$, respectively, are equal, and if the recombination efficiency is equal to 1. However, in general the first condition is not met due to different shapes of the emission profiles. This is shown schematically in the figure. The singlet fraction is therefore given by

$$\eta_S = \frac{1}{\eta_{rec}} \cdot \frac{\eta_{out,PL}}{\eta_{out,EL}} \times \frac{\frac{P_{EL}}{I_{inj}}}{-\frac{dP_{PL}}{dI_{ph}}} . \quad (4.1)$$

We have employed this expression to determine η_S for a polyfluorene-triarylamine copolymer (PF-TAA, described in detail in Section 4.2), which is present as a single layer in OLEDs of the type shown in figure 4.1. PF-TAA is a relatively efficient blue fluorescent emitter, with a PL efficiency equal to approximately 60 %, ²⁴ and has been used in the 13" full-color OLED-TV display demonstrated by Philips in 2005. ²⁵ The hole and electron transport in this material have been intensively studied. ^{26,28,27} Its choice is furthermore motivated by the availability

of accurate descriptions of the layer thickness and voltage dependent EL emission profiles.²³ The presence of the copolymerized monomer units, in a small concentration, can give rise to an optimized hole-injection and electron-hole mobility balance, as studied in detail for OLEDs based on various fluorene-based co-polymers.^{24,29-32} In PF-TAA, the hole states are expected to be localized on these units.²⁸ The effective conjugation length is therefore expected to be much smaller than in polyfluorene derivatives without copolymerized units, such as poly-dioctylfluorene (PFO), for which a strongly enhanced singlet efficiency has been found (see Table 4.1). Studies for various types of polymers indicate that η_S should decrease with decreasing repeat length,^{4,6,9,33} approaching the quantum-statistical value for systems approaching the monomer limit. For the PF-TAA polymer studied, it is not *a priori* clear whether it could be considered as a material with such a small conjugation length that it would effectively be similar to a small-molecule material, or whether its polymeric character could still give rise to an enhanced singlet fraction. From our results we deduce values η_S in the range 10-25% for PF-TAA, increasing with increasing emitting layer thickness in the 100-160 nm layer thickness range studied.

Sections 4.2 to 4.4 introduce the method and show the results of the application on PF-7.5%TAA copolymer. Section 4.2 contains a detailed description of PF-TAA copolymers, the experimental set-up and the modeling methods employed. In Section 4.3 the experimental and modeling results are presented and analyzed. The results are discussed in Section 4.4. In order to analyze the possible effect of different concentration values of the hole-transporting group, in Section 4.5 the method is applied to PF-0.5%TAA copolymers. Furthermore, we applied the method also to polyphenylene-vinylene-based OLEDs, thus probing a different location of the light-emission profiles.²³ A second motivation for the analysis of PPVs is the possibility to benchmark our method with those already presented in the literature and applied to the same class of materials, see Table 4.1 The results are summarized in Section 4.6. In Section 4.7 the overall conclusions are given.

4.2 Light-emitting polymer and experimental methods

The organic semiconductor studied, PF-TAA, is a blue-emitting polymer from the LumationTM Blue Series supplied by Sumation Co., Ltd. It consists of a polyfluorene (PF) based polymer with randomly copolymerized triarylamine (TAA) monomer units (7.5 mol %). The molecular structure of the polyfluorene and TAA units is shown on figure 4.2(a). The device structure used is shown on figure 4.1. The anode consists of a 100 nm thick poly(3,4-ethylenedioxythiophene):poly(styrenesulfonic acid) (PEDOT:PSS) layer, spin-coated on precleaned glass substrates covered with 120 nm indium tin oxide (ITO). The cathode consists of a 5 nm thick barium and a 100 nm thick aluminum layer, sequentially evaporated in a high-vacuum chamber on top of the PF-TAA. Devices with three different PF-TAA emitting layer thicknesses, 100, 130 and 160 nm, were stu-

died. The use of patterned bottom and top electrodes results in glass | ITO | PEDOT:PSS | PF-TAA | Ba | Al structures with areas of $1 \times 1 \text{ mm}^2$. The energy level diagram for the layer stack studied is shown in figure 4.2(b). The electron transport occurs along PF-derived states,²⁷ while the hole transport takes place via the TAA units.^{26,28}

The current (I) versus voltage (V) measurements are carried out using a Keithley 2400 sourcemeter. The light emitted in the direction orthogonal to the device surface is focused on a cooled Hamamatsu HPD-TA CCD camera. For the PL quenching measurements a defocused UV diode laser (emission wavelength 405 nm) is used. The optical power on the sample is 0.6 mW. The voltage range within which the forward bias EL measurements were carried out (restricted at the lower side by the instrumental sensitivity, and at the higher side by the long-term device stability under steady-state operation) was 8.5-10.5 V, 9.5-11.5 V and 12.5-15.5 V for the 100, 130 and 160 nm devices, respectively. All measurements were carried out at room temperature.

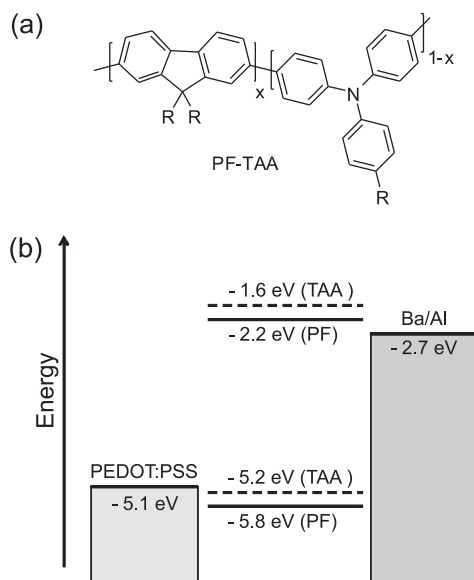


Figure 4.2: (a) Molecular structure of PF-TAA, containing randomly co-polymerized polyfluorene (PF) and triarylamine (TAA) monomer units (7.5 mol %). (b) Energy level diagram of the devices studied, with the energies with respect to the vacuum level.

The light-absorption in a PL experiment is calculated using a thin-film optical microcavity model (software MacLeod, Thin Film Center Inc.). The complex refractive indices of the layers are determined by ellipsometry.²³ We will first assume that the PL light-emission profiles are equal to the absorption profiles. For the devices studied, this is expected to be a fair approximation, as the exciton diffusion length (λ_d) for fluorescent polymers is small, of the order of 5 – 10 nm.³⁴ Subsequently, we will investigate the possible effect of exciton diffusion on

the results of the analysis. The PL outcoupling efficiency is then calculated using a computer simulation tool, LIGHTEX,³⁵ developed at Philips Research Aachen. The dipole orientation in the PF-TAA layer is assumed to be in-plane, as obtained from the analysis of emission experiments in Ref. 23. The microcavity model used treats excitons as radiating dipole emitters, and includes absorption in the layers and the enhancement of the radiative decay rate due to nearby electrodes. All optical modes are considered. A comparison with other models described in the literature is given in Ref. 23.

The layer thickness and voltage dependent EL emission profiles across the active layer have been obtained in a manner as described in Ref. 23, from the EL emission intensity measured as a function of the wavelength with a resolution of 1 nm, as a function of the emission angle in steps of 2° from orthogonal emission to 70°, and as a function of the polarization, using a commercial Melcher Autronic Display Metrology System (DMS) system and using a glass hemisphere on top of the sample in order to enhance the range of internal modes from which emission can be extracted.³⁶ LIGHTEX was used to obtain the EL outcoupling efficiencies from these profiles.

4.3 Experimental results and analysis

In figure 4.3 the experimental results obtained from the EL and PL measurement of a 160 nm thick device are presented. Similar results were obtained for the 100 nm and 130 nm devices.

Figure 4.3(a) shows the dependence of the measured PL quenching ($-\Delta P_{\text{PL}}(V) \equiv P_{\text{PL}}(V) - P_{\text{PL}}(0)$) and the corresponding photocurrent, $I_{\text{ph}}(V)$, on the reverse applied voltage. The voltage dependence of both quantities is essentially equal, so that, as shown in figure 4.3(b), the PL quenching is proportional to the measured photocurrent. The same result was obtained for the 100 and 130 nm devices. The ratio $-dP_{\text{PL}}/dI_{\text{ph}}$ in Eq. (4.1) is thus independent of the applied voltage, as also observed for other materials in Ref. 7, which confirms the validity of the method.

The consistency of the approach may also be investigated by carrying out a more quantitative analysis of the photocurrent and the photoluminescence change. From the optical power used, the angle of incidence (30° with respect to the surface normal; s-polarized light) and a calculation of the light absorption in the emissive layer, the maximum photocurrent is expected to be 116, 148 and 134 μA for the 100, 130 and 160 nm devices, respectively, with an estimated uncertainty of approximately 20%. From the experimental relative value of the slope of $-\Delta P_{\text{PL}}/P_{\text{PL}}(V=0)$ versus I_{ph} , we deduce values of the maximum photocurrent equal to 93 ± 10 , 110 ± 30 and 137 ± 14 μA . Taking the uncertainties of the maximum photocurrents as deduced from both methods into account, we conclude that the experimental results are consistent with the assumption that the PL quenching observed is due to field-induced dissociation of excitons. We note that in all cases the relative PL quenching was at most approximately 40% (by applying a voltage of approximately -18, -24 and -30 V for the 100, 130 and 160

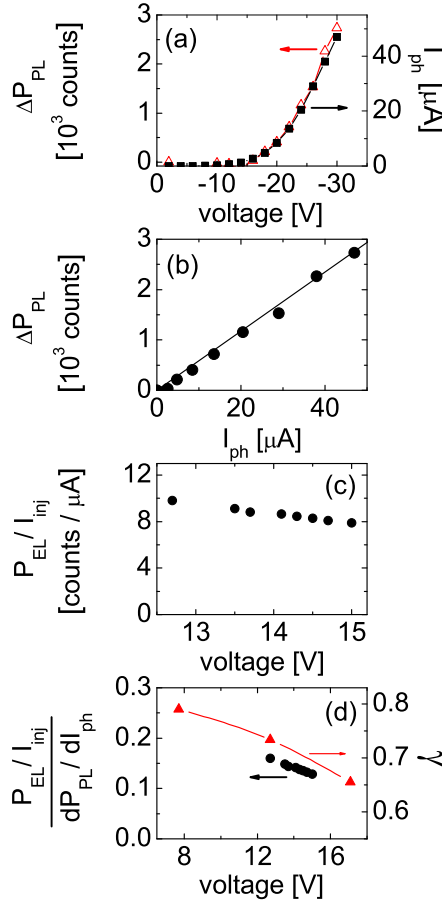


Figure 4.3: (Color online) (a) PL quenching and photocurrent as a function of the voltage. (b) Correlation between the measured PL quenching and the corresponding photocurrent for different values of the voltage (full circles). The line through the origin is a guide to the eye. (c) Voltage dependence of the normalized EL intensity, P_{EL}/I_{inj} . (d) Voltage dependence of the ratios $(P_{EL}/I_{inj})/(-dP_{PL}/dI_{ph})$ and $\gamma \equiv \eta_{out,EL}/\eta_{out,PL}$.

nm devices, respectively), in order to avoid the risk of damaging the devices by the application of a too high reverse field. We also note that in all cases the slope was obtained from the voltage range in which a significant photoluminescence quenching and a significant photocurrent are measured, e.g. from -20 V to -30 V for the 160 nm devices, in order to be able to determine the slope with a high accuracy.

The same experimental set-up is employed to measure the optical power and the injected current in an EL experiment. Figure 4.3(c) shows the measured voltage dependence of the ratio P_{EL}/I_{inj} for 160 nm device, which is proportional

to the external quantum efficiency. A weak although not fully negligible roll-off of the external quantum efficiency as a function of the applied voltage is found, which is a well-known phenomenon in fluorescent OLEDs.^{37,38} As a result, the ratio $(P_{\text{EL}}/I_{\text{inj}})/(dP_{\text{PL}}/dI_{\text{ph}})$ (see Eq. (4.1)) depends on the voltage at which the device is driven under EL performance, as shown in figure 4.3(d). This voltage dependence can be understood as a result of a voltage dependence of the EL light outcoupling efficiency, i.e. of the parameter $\gamma \equiv \eta_{\text{out,EL}}/\eta_{\text{out,PL}}$ which is shown in the same figure. The parameter γ has been obtained from the calculated PL emission profiles for each of the three layer thicknesses, shown in figure 4.4(a-c), and from the EL emission profiles as obtained for the three layer thicknesses at the three different voltages for which the profiles are shown in figure 4.4(d-f). The calculated PL emission profiles, which are taken here equal to the absorption profiles, are clearly not homogeneous through the emitting layer, due to microcavity effects. Furthermore, they show a distinct emitting layer thickness dependence. The EL emission profiles are not only layer thickness dependent, but also slightly voltage dependent. As a result, the parameter γ is found to vary from 1.45 to 1.44 for the 100 nm devices, from 1.30 to 1.15 for the 130 nm devices, and (see figure 4.3(d)) from 0.79 to 0.66 for the 160 nm devices.

The analysis shows that γ can be significantly smaller than 1, e.g. for the 160 nm-thick-emitting layer. This leads to a strong correction on the value of η_{S} that would be obtained if the EL and the PL outcoupling efficiencies were assumed to be equal. Furthermore, the voltage dependence of γ is for all three thicknesses found to be essentially equal to the voltage dependence of the ratio $(P_{\text{EL}}/I_{\text{inj}})/(dP_{\text{PL}}/dI_{\text{ph}})$, as may be seen for the 160 nm devices in figure 4.3(d). It follows from Eq. (4.1) that the value obtained for η_{S} is then essentially voltage-independent, as expected for a material property, if the recombination efficiency is voltage independent. In the next section, we show from numerical studies using a recently developed drift-diffusion device model³⁹ that for all layer thicknesses and voltages η_{rec} is indeed very close to 1. This leads to an essentially voltage-independent value for η_{S} , for all the emitting layer thickness values analyzed. Figure 4.5 gives the values of the singlet fraction which are deduced for the different emitting layer thickness, using the PL and EL emission profiles given in figure 4.4 (circles).

4.4 Discussion - PF-7.5%TAA

The values of the singlet fraction shown in figure 4.5 (circles) are close to the standard statistical value (dashed line), or smaller. In order to analyze these results, we first consider the effects of exciton diffusion on the PL emission profile. We have calculated the PL emission profiles as a function of the exciton diffusion length, assuming as a boundary condition that the electrodes are perfect sinks of excitons, so that the PL emission profile is zero at the electrode interfaces. For realistic values of the diffusion length, up to 10 nm, only a very small and approximately linear variation of the γ parameter is found. In figure 4.5 the values of η_{S} for a diffusion length of 10 nm are shown (triangles). Although the effect is

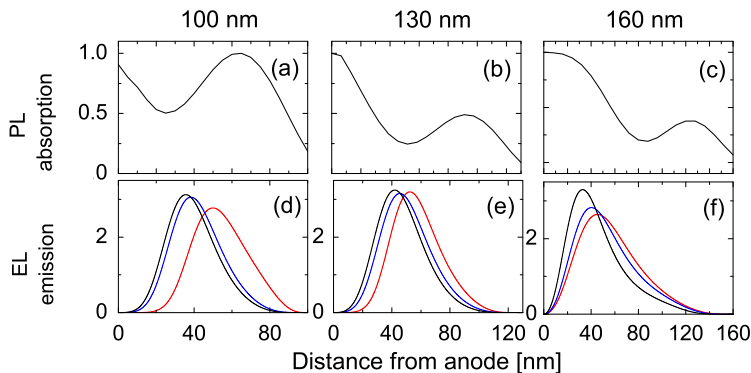


Figure 4.4: (Color online) Calculated normalized layer thickness dependent PL (a-c) and EL (d-f) emission profiles across the active layer. The voltages used in the EL experiments are 5.3 V - 8.7 V - 11.5 V (100 nm), 6.8 V - 9.6 V - 11.8 V (130 nm) and 7.7 V - 12.7 V - 17.1 (160 nm). In all devices, the emission profile shifts towards the anode with increasing voltage.

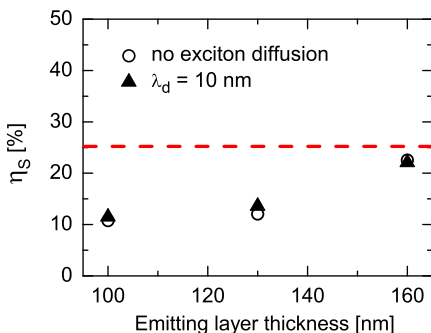


Figure 4.5: (Color online) Calculated singlet fraction in PF-TAA as a function of the emitting layer thickness, neglecting exciton diffusion when modeling the PL emission spectrum (circles) and assuming a $\lambda_d = 10$ nm exciton diffusion length (triangles). The standard-statistical singlet fraction is equal to 25 %, as indicated by the dashed line.

found to be slightly thickness dependent, and largest for the 130 nm device, it is quite small so that it does not explain the observed thickness dependence of η_s .

Secondly, we investigate to what extent the shape of the EL emission profile as shown in figure 4.4 is consistent with the shape which would follow using a drift-diffusion charge transport and recombination simulation. For this purpose, we have used the model presented in Ref. 39, using the experimentally determined hole and electron mobility functions obtained in Refs. 26 and 27, respectively. In Ref. 27, the electron mobility was determined using a LiF/Ca/Al cathode, for which the electron injection barrier was found to be equal $\Phi_e = 0.3 \pm 0.1$ eV.

However, in our present study a Ba/Al cathode is used, for which from a preliminary study Φ_e is estimated to be more close to ~ 0.5 eV.²⁴ We have investigated the consistency between the experimental results and the model predictions by first comparing the experimental voltage dependence of the current density, J , with the prediction as obtained for $\Phi_e = 0.5$ and 0.6 eV. The results are shown in figure 4.6(a), for 160 nm devices. Below ~ 3 V, the current density is determined by the leakage current ($J \propto V$). Near the onset voltage, around 3 V, the electron and hole current densities are found to be strongly unbalanced, so that the recombination takes almost exclusively place close to the cathode. The current density is therefore almost exclusively due to the hole current density, so that it is almost independent of the precise value of the electron injection barrier. This is confirmed by the calculations. The large observed average slope of the $J(V)$ curve at higher voltages, approximately 4, is well predicted by both calculations, although slightly better when assuming $\Phi_e = 0.6$ eV. However, above 10 V, neither of the two curves provides a good description of the slope. From pulsed (AC) measurements (10 Hz at a 1% duty cycle), we have found that in this regime some sample heating occurs. The figure reveals a current density increase up to a factor of ~ 2.5 in the voltage range of 13-15 V for which the analysis presented in the previous section was done. It was found from the simulations that such an effect would correspond to an internal temperature increase of at most ~ 25 K, and that such a temperature change has (in this case) no significant effect on the shape of the calculated recombination profile. A similar estimated temperature increase was found for the 100 and 130 nm devices, and the same conclusion was obtained concerning the effect on the profiles. The profiles calculated for $\Phi_e = 0.5$ and 0.6 eV, and at 15 V, are shown in figure 4.6(b). A comparison with the experimental profiles shown in figure 4.4(f) shows that the 0.5 and 0.6 eV profiles are located more closely to the anode and cathode, respectively, and that both profiles are significantly wider than as found experimentally. We view this as an indication that a more refined model for the recombination process will be required, beyond the standard Langevin model employed. Recently, several refinements have been discussed in the literature, including the effect of carrying out the calculation using so-called “bipolar” mobilities⁴⁰ and including the possible effect of mobility anisotropy.⁴¹ An enhanced recombination rate, resulting from an enhanced lateral mobility, would be expected to give rise to narrower recombination profiles. For the PF-TAA polymers which we studied, the presence of strong in-plane orientation of the emitting dipoles²³ is indicative of a strong in-plane orientation of the polymer chains. A strong anisotropy of the electron mobility, which is due to transport via the LUMO states derived from the PF backbone, may therefore be expected. On the other hand, the hole mobility, which is due to hopping in between the TAA units, is not expected to be strongly anisotropic. In order to investigate the effect on the recombination profile, we adapted the approach for calculating the local recombination rate presented in Ref. 39 by including an enhanced contribution from lateral hops of electrons to nearest neighbor sites at which a hole resides. We varied this enhancement factor, considering it as a free parameter, and found that introducing this enhancement gives indeed rise to narrowing of the profile. For 160 nm devices, we found that

the recombination profiles as calculated and measured at 15 V are quite similar when choosing a mobility anisotropy factor equal to 7, using $\Phi_e = 0.5$ eV and using a slightly (factor 1.5) enhanced electron mobility in order to fine-tune the peak position. The resulting $J(V)$ curve is almost indistinguishable from that shown in figure 4.6(a) for $\Phi_e = 0.5$ eV. The resulting profile is shown in figure 4.6(b) (“optimized”). The anisotropic shape is quite similar to the experimental profiles measured at 12.7 and 17.1 V. In figure 4.6(c), we investigate the voltage and layer thickness dependence of the recombination profiles by carrying out for each thickness calculations at two values of the voltage within the experimental voltage range (see the figure caption). For each case studied, the electron and hole currents are quite well balanced, and the recombination efficiency is found to be essentially equal to 1. The figure shows for all layer thicknesses a predicted shift of the profile towards the anode with increasing voltage. Such a shift is indeed observed, although the experimental shifts are smaller than calculated. Furthermore, the calculations predict for the two thinner devices a peak shift to positions more close to the anode than is actually observed. This might indicate that in these devices close to the anode additional exciton quenching processes take place, on top of the exciton quenching already taken into account in the microcavity model.

A possible explanation of these observations would be a modification of the composition of the PF-TAA near the interface with the PEDOT:PSS layer, giving rise to a reduced radiative lifetime of excitons generated close to the anode. Evidence of proton diffusion at elevated temperatures from the PEDOT:PSS layer into an organic semiconductor deposited on top of that layer has been found by Köhnen *et al.*⁴² The EL efficiency would be already significantly affected by an approximately 20 nm thick zone near the anode with a reduced radiative decay probability. We note that in the emission profiles shown in figure 4.4(d-f) such a possible effect would already be included, so that in its absence the emission intensities near the anode would be larger. As noted above, the maximum thermal loads in our experiments (~ 25 K thermal increase) were quite limited. However, it is not known how the proton diffusion rate into PF-TAA will depend on the temperature.

Another factor which could affect the analysis is polaron or field-induced quenching of singlet excitons,⁷ which could result in a decrease of the EL quantum efficiency with increasing current density. However, we have no experimental evidence for this effect. The EL efficiency has been found to show a weak voltage dependent roll-off, but we have shown that this can be attributed completely to a voltage dependence of the EL outcoupling efficiency. Furthermore, EL-specific losses may occur if electroluminescent excitons form preferentially at certain molecular sites such as charge traps or if excitons preferably recombine at trap sites. As explained by Segal *et al.*,⁷ this should result in an EL quantum efficiency that increases with applied voltage, when the filling of traps approaches saturation. However, after taking the voltage dependence of the light outcoupling efficiency into account, we do not find such an increase of the EL quantum efficiency.

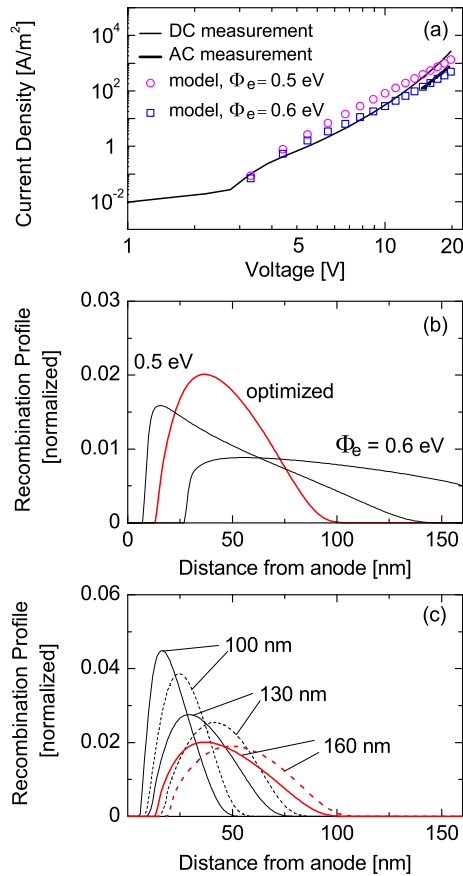


Figure 4.6: (Color online) (a) Measured and calculated current density in 160 nm devices, as explained in the main text, (b) Calculated normalized recombination profile for 160 nm devices at 15 V, as obtained using the experimental electron and hole mobility functions and isotropic recombination with $\Phi_e = 0.5$ and 0.6 eV, and as obtained using an “optimized” approach (see the main text), (c) Normalized recombination profiles calculated using the “optimized” approach at 9 and 11 V (100 nm), 10 and 12 V (130 nm) and 13 and 15 V (160 nm). The full (dashed) curves are for the higher (lower) voltage values.

Finally, it would be of interest to investigate whether within refined models of the exciton formation and radiative recombination process in OLEDs the recombination efficiency will, for the systems studied, still be very close to 1. One may envisage that (i) the filamentary nature of electron and hole current density⁴³ due to the energetic disorder, (ii) the screening of the electron-hole attraction by the electrodes might both affect the recombination efficiency when the emission profile is peaked near one of the electrodes. One may also envisage that the generation

of excitons at a distance from the electrode which is comparable to the exciton diffusion length could result in a lower effective recombination efficiency. Based on the calculated results shown in figure 4.6(c), this effect would be largest for the thinnest (100 nm) device, as the peak in the calculated recombination profile is located at only approximately 15-25 nm. The trend observed in figure 4.5 would then be consistent with a decrease of the effective recombination efficiency with decreasing device thickness as a result of a decrease of the distance of the peak of the EL recombination profile to the anode. The singlet fraction as obtained for the thickest device, which is closer to 25 %, would be least affected. Therefore, it could be considered as more precise. However, further narrowing down the uncertainty interval of the value of the singlet fraction obtained, by the development of a quantitative model for the recombination profile and exciton quenching near electrodes, is beyond the scope of this chapter.

In the absence of a more refined approach from which the observed layer thickness dependence of the singlet fraction can be explained, our present best estimate is $\eta_S = 17 \pm 6$ %. In view of the significantly enhanced singlet fraction observed for the similar polymer material PFO (see Table I), without hole transporting units, this would indicate that the presence of the TAA monomer units on which the holes are known to be mainly localized makes the effective conjugation length in PF-TAA very short. Strong deviations from the standard statistical value, to higher values, are then less likely.^{18,44} We note that a deviation to lower values could be explained within the framework of a model developed by Kalinowski and co-workers,^{21,45} who analyzed the effect on the singlet exciton fraction of the trapping of carriers in rather deep states. This would give rise to an activation barrier for singlet exciton generation, thereby reducing the singlet formation rate and thus the EL intensity.

4.5 Polyfluorene-based devices with 0.5 mol% copolymerized TAA

In this section we extend the analysis of the singlet fraction value in PF-TAA-based OLEDs to different concentrations of the triarylamine hole transporting units. The hole transport characteristics are known to change for copolymers with different TAA concentration. Figure 4.7 shows the hole current density measured in devices where the amine concentration was varied. Three regimes can be distinguished. For an amine concentration smaller than 2.5%, hole transport takes place through the polymer backbone, with the TAA groups acting as hole traps. For amine concentration values much higher than 2.5%, the hole current is due to hopping transport via the TAA units. At TAA concentrations close to 2.5%, an intermediate situation can be expected and hole transport will be characterized by hopping in between the TAA units as well as via the PF backbone. Having analyzed PF-7.5%TAA in the previous sections, we decided to study devices based on two PF-TAA polymers for which the hole transport is in the first and second regime: PF-0.5 mol%TAA and PF-20 mol%TAA, respectively. Dif-

ferent localization extensions of hole states may then lead to a more polymer-like or a more small-molecule like behavior, and thus to a potentially different exciton singlet fraction (see ref. 44).

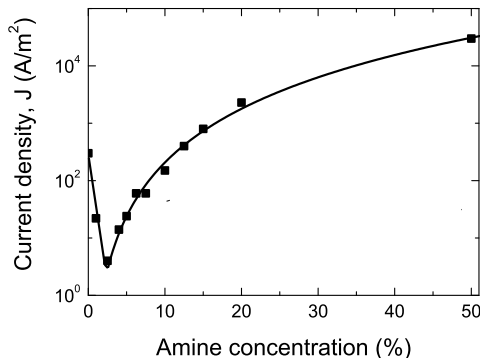


Figure 4.7: Hole current density at 6 V as measured for PF-TAA copolymer-based devices with different amine concentrations, expressed in mol%. After ref. 28.

A complete analysis, presented in this section, was performed on the 0.5% copolymer. For the second copolymer two problems had a negative effect on the reliability of the analysis. First, the reconstructed light-emission profiles were found to be located very close to the cathode, so that due to strong exciton quenching the measured light intensity is very small, and as a consequence the signal-to-noise is too low to reliably extract the light-emission profiles. Probably the e-h recombination happens even closer to the metallic electrode, thus leading to a low measured light intensity. Moreover, a severe encapsulation problem affected the stability of the devices over consecutive measurements. For these reasons, we will only present here the results obtained from the analysis of the PF-0.5 mol%TAA copolymer. For these devices, a similar layer stack as already presented for the PF-7.5mol%TAA devices was employed. Three thickness values for the emitting layer were investigated: 120, 140 and 160 nm.

Figure 4.8 shows the reconstructed light-emission profiles for the different thickness cases. Surprisingly, the emission profiles obtained from the analysis are located at distance from the anode which is comparable to that obtained for the PF-7.5 mol% case. The low triarylamine-unit concentration in the PF-0.5 mol% strongly affects the charge transport in this type of devices. Hole hopping is expected to be more difficult as compared to the PF-7.5 mol% case, due to the increased average distance between hole-transporting groups. The electron-hole recombination profile and, consequently, the light-emission profile are then expected to be located closer to the anode. Possibly, the observed relatively large distance of the profile peak from the anode could be due to PEDOT:PSS diffusion in the polymer emitting layer, as a consequence of the thermal treatment the

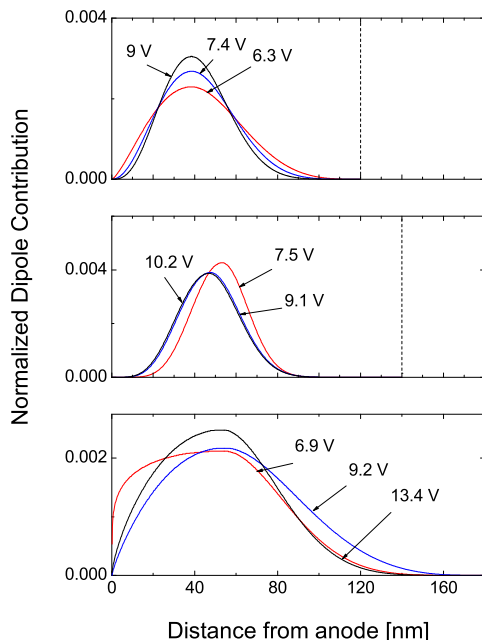


Figure 4.8: Normalized EL emission profiles across the active layer for PF-0.5mol%TAA devices for three values of the layer thickness: 120, 140, 160 nm, from top to bottom. The profiles are presented as a function of the applied voltage. The dashed lines indicate, for the 120 and 140 nm case, the cathode surface.

devices undergo during their preparation (90 °C for 15 minutes, during the encapsulation process). In our optical model we presently assume the absence of any mixed region between the PEDOT-PSS and the PF-TAA layers. The presence of such a “ spacer ” region would increase the distance of the light-emission profile peak from the anode. As for the 7.5%TAA case, only a weak dependence of the profile is observed when the applied voltage is changed. The peak distance from the anode seems to be essentially independent on the device thickness as well.

In figure 4.9, the experimental results obtained from the EL and PL measurement of a 120 nm thick device for the PF-0.5mol%TAA device are shown. Also for this copolymer the PL quenching is found to be proportional to the measured photocurrent, I_{ph} , as shown in the figure. Similar results were obtained for the 140 and 160 nm devices. The ratio $-dP_{\text{EL}}/dI_{\text{ph}}$ is thus independent of the applied voltage, which confirms the validity of the method.

To verify that the experimental analysis is performed in a linear excitation regime, in order to exclude non-linear excitonic processes, we repeated the ex-

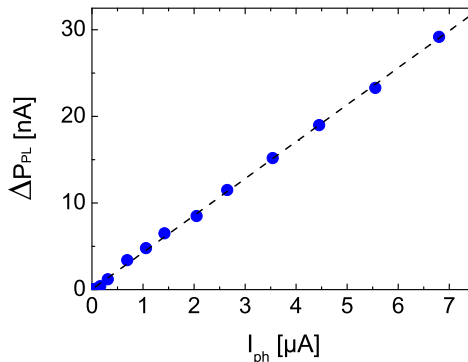


Figure 4.9: Measured PL quenching as a function of the corresponding photocurrent for a 120 nm PF-0.5mol%TAA device, for different values of the voltage (solid circles). The line through the origin is a guide to the eye.

periment for different values of the laser power. For all experiments, ΔP_{PL} was found to be proportional to I_{ph} , with essentially the same proportionality factor.

The consistency of the approach may also be investigated by carrying out a more quantitative analysis of the photocurrent and the photoluminescence change. From the optical power used, the angle of incidence (30° with respect to the surface normal; s-polarized light), and a calculation of the light absorption in the emissive layer, the maximum photocurrent is expected to be 40.7, 40, and 37 μA for the 120-, 140-, and 160-nm devices, respectively, with an estimated uncertainty of approximately 20%. From the experimental relative value of the slope of $\Delta P_{PL}/P_{PL}$ ($V = 0$) versus I_{ph} , we deduce values of the maximum photocurrent equal to 39.7 ± 5 , 33.9 ± 5 , and 35.5 ± 6 μA . Taking the uncertainties of the maximum photocurrents as deduced from both methods into account, we conclude that the experimental results are consistent with the assumption that the PL quenching observed is due to field-induced dissociation of excitons.

For all the devices thicknesses, the ratio P_{EL}/I_{inj} , which is proportional to the external quantum efficiency, shows a voltage dependence. As a result, the ratio $(P_{EL}/I_{inj})/(dP_{PL}/dI_{ph})$ depends on the voltage at which the device is driven, as shown in figure 4.10. In contrast to the results for the 7.5% devices (figure 4.3 (d)), an increase of the ratio with increasing voltage is found.

In order to be able to calculate the singlet fraction η_S using eq. (4.1), the parameter $\gamma = \eta_{out,PL}/\eta_{out,EL}$ was obtained from the modeled PL emission profiles for each of the three layer thicknesses, shown in figure 4.11, and from the EL emission profiles as obtained for the three layer thicknesses at the three different voltages for which the profiles are shown in figure 4.8. The calculated PL emission profiles, which are taken here equal to the absorption profiles, are not

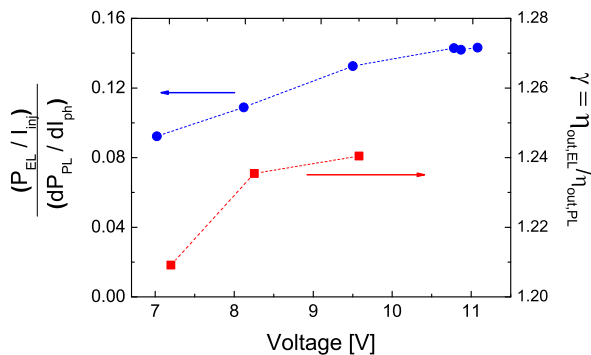


Figure 4.10: Voltage dependence of the ratio $(P_{\text{EL}}/I_{\text{inj}}) / (dP_{\text{PL}}/dI_{\text{ph}})$ (circles) and $\gamma \equiv \eta_{\text{out,EL}}/\eta_{\text{out,PL}}$ (squares), for a 120 nm PF-0.5mol%TAA device.

homogeneous through the emitting layer due to microcavity effects and show an emitting layer thickness dependence.

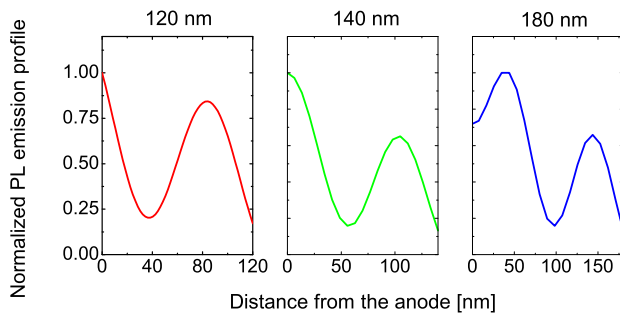


Figure 4.11: Calculated normalized PL emission profiles across the active layer, for three PF-0.5mol%TAA layer thickness values: 120, 140, 160 nm.

The EL emission profiles are not only layer thickness dependent but also slightly voltage dependent, as also found in fig. 4.4 for the 7.5% case. The voltage dependence of γ is found to be essentially equal to the voltage dependence of the ratio $(P_{\text{EL}}/I_{\text{inj}})/(dP_{\text{PL}}/dI_{\text{ph}})$, as shown for the 120 nm devices in figure 4.10. It follows, from eq. (4.1), that the singlet fraction value is then essentially voltage independent, as expected for a material property, if the recombination efficiency is voltage independent. Figure 4.12 gives the values of the singlet fraction that are deduced for the different emitting layer thicknesses, based on the EL and PL emis-

sion profiles given in figures 4.8 and 4.11. The singlet fraction values obtained, in the range 8%-24% independent of the voltage, shown in figure 4.12 in squares, are smaller than the standard statistical value (dashed line). A significant emitting layer-thickness dependence was found, as for the 7.5% device (see figure 4.5). At present, we do not have an explanation for these results.

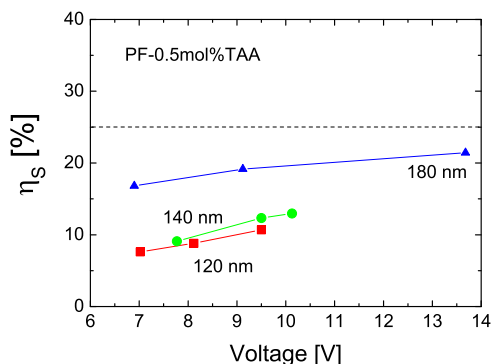


Figure 4.12: Calculated singlet fraction in PF-0.5mol%TAA as a function of voltage for the three emitting layer thicknesses values analyzed: 120 nm (squares), 140 nm (circles) and 180 nm (triangles). The dashed line indicates the standard-statistical singlet fraction (25%).

4.6 Poly(phenylene vinylene)-based devices

The analysis of both 0.5% and 7.5% PF-TAA devices led to an exciton singlet fraction smaller than 25%, and quite layer thickness dependent. It would be of interest to study a case where the shapes of the light-emission profiles are expected to be substantially different. In poly(phenylene vinylene) (PPV) based polymers, for example, the electron-hole recombination profiles are expected to be located closer to the cathode,⁴⁶ thus quite different from the results just shown for PF-TAA OLEDs. Moreover, PPVs are a class of group of materials for which the singlet fraction has been investigated using various techniques. In Table 4.1, results were already presented for poly(2-methoxy-5-(3',7'-dimethyloctyloxy)-p-phenylene vinylene) (OC₁C₁₀-PPV) and poly(2-methoxy-5-(2'-ethylhexyloxy)-p-phenylene vinylene) (MEH-PPV). With the purpose to compare our approach with the results of these previous literature studies, we fabricated two PPV-based types of devices: MEH-PPV and poly(2-methoxy-5-(3',7'-dimethyloctyloxy)-p-phenylene vinylene) poly[4'-(3,7-dimethyloctyloxy)-1,1'-vinylene] (NRS-PPV). In both cases the device structure is the following: glass/ ITO (120 nm) /PEDOT:PSS (100 nm) / PPV / barium (5 nm) / aluminum (100 nm). Already in the initial stage of the study, it became apparent that the method was not

applicable to MEH-PPV devices, as they were quickly degraded by the laser light used for carrying out the PL experiment. In order to investigate the laser wavelength dependence of the degradation, we performed the measurements at two different wavelengths within the absorption region, 408 and 440 nm, at the same optical power, equal to 0.24 mW. The laser-induced degradation effect was present in both cases. By reducing the laser power under a value of 0.18 mW, the damage was not anymore visible by naked eye. However, a more detailed study of the laser effect would be needed to exclude any effect on the device performance. Moreover, even at the lowest laser power we observed a non-constant $\Delta P_{\text{PL}}/I_{\text{ph}}$ ratio as a function of the applied reverse voltage. A similar problem was encountered for MEH-PPV based devices by Segal *et al.*⁷ who related this to the presence of a large dark current. For all these reasons the study of the singlet fraction on this material was not continued.

A full analysis leading to η_{S} was carried out for the NRS-PPV-based OLEDs, for which no laser-induced degradation was observed. The emitting layer thicknesses studied are 60, 90 and 120 nm. The reconstructed light-emission profiles for the NRS-PPV OLEDs are shown in figure 4.13, at three values of applied voltage. It is found that the emission profiles are surprisingly narrow as com-

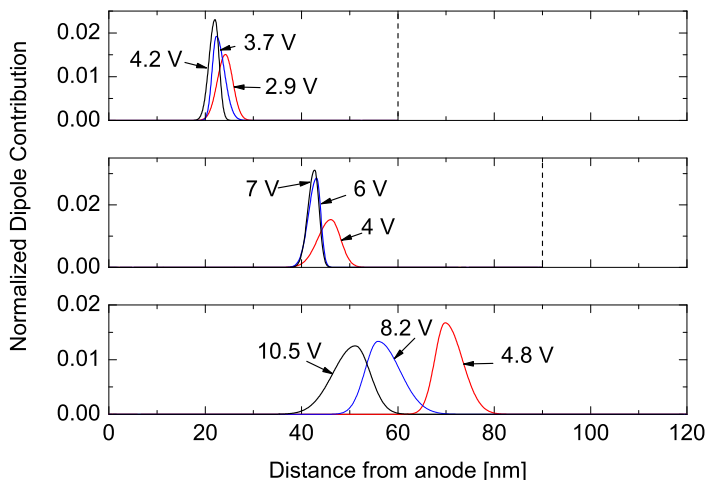


Figure 4.13: Normalized EL emission profiles across the active layer of NRS-PPV based devices thickness for three values of the layer: 120, 140, 160 nm, from top to bottom. The profiles are presented as a function of the applied voltage. The dashed lines indicate, for the 120 and 140 nm case, the cathode interface.

pared to the recombination profiles as published in the literature.⁴⁶ Moreover, the distance of the profile peak from the cathode is in all cases larger than 40 nm.

The narrow emission profiles could be due to anisotropy in the charge mobility functions (charges move faster along the polymer chains, which are predominantly oriented parallel to the layer interface), as previously mentioned for the case of PF-7.5mol% TAA. Exciton diffusion would broaden the emission profile. However this effect is expected to be small, as the singlet exciton diffusion length for fluorescent polymers is generally believed to be only ~ 5 nm, see for example ref. 46. In the absence of injection barriers and electron trap sites, one would in fact expect the hole-electron mobility to be balanced. The recombination should then happen roughly in the middle of the device. Since the presence of electron traps has been demonstrated already for this material,⁴⁶ one possible explanation for the location of the profile in the middle of the emitting layer and not close to the cathode, as predicted,⁴⁶ would consist in assuming the presence of an injection barrier for holes from PEDOT:PSS.

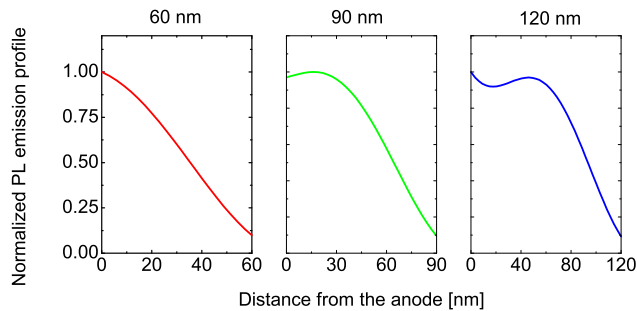


Figure 4.14: Calculated normalized PL emission profiles across the active layer, for three NRS-PPV layer thickness values: 60, 90, 120 nm.

Figure 4.14 shows the calculated PL profiles for NRS-PPV based devices of 60, 90 and 120 nm. The ratio $dP_{\text{PL}}/dI_{\text{ph}}$ is found to be independent of the applied voltage, as shown in figure 4.15. As for the PF- 0.5 mol%TAA devices, also for the NRS-PPV based OLEDs we verified the consistency of the approach by comparing the values of the maximal photocurrent expected from the experimental conditions and set-up and the value of the maximum photocurrent as deduced from the experimental relative value of the slope of $\Delta P_{\text{PL}}/P_{\text{PL}}(V = 0)$ versus I_{ph} . The maximum photocurrent is expected to be 32.24, 31.3, and 34.3 μA for the 60, 90, and 120 nm devices, respectively, with an estimated uncertainty of approximately 20%. We deduce values of the maximum photocurrent equal to 30 ± 6 , 31.5 ± 6 , and 33 ± 6.5 μA . Taking the uncertainties of the maximum photocurrents as deduced from both methods into account, we conclude that the experimental results are consistent with the assumption that the PL quenching observed is due to field-induced dissociation of excitons. The ratio $(P_{\text{EL}}/I_{\text{inj}})/(dP_{\text{PL}}/dI_{\text{ph}})$ varies with the voltage, as shown in figure 4.16. This voltage dependence is also present in the parameter $\gamma = \eta_{\text{out,EL}}/\eta_{\text{out,PL}}$, shown in figure 4.16 for the 90 nm

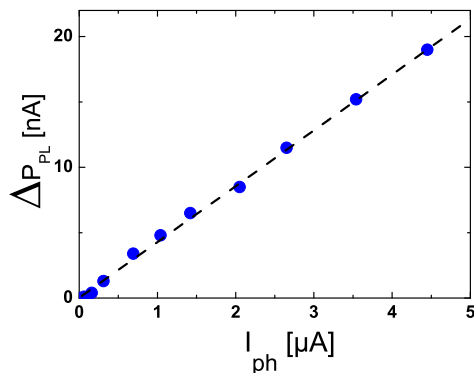


Figure 4.15: Measured PL quenching as a function of the corresponding photocurrent for a 90 nm-thick NRS-PPV device, for different values of the voltage (solid circles). The line through the origin is a guide to the eye.

thickness case. The EL and PL emission profiles from which the γ parameters were obtained are shown in figure 4.13 and 4.14, respectively.

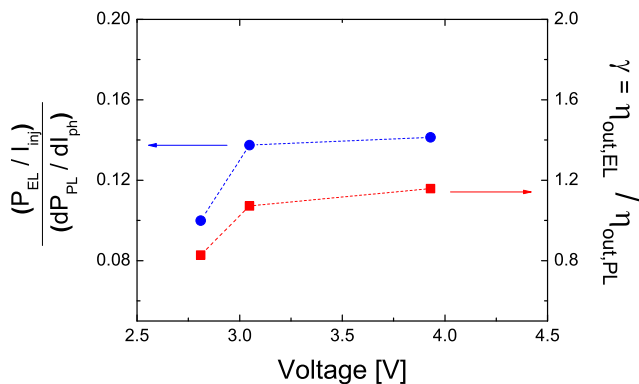


Figure 4.16: Voltage dependence of the ratios $(P_{EL}/I_{inj}) / (dP_{PL}/dI_{ph})$ (circles) and $\gamma \equiv \eta_{out,EL}/\eta_{out,PL}$ (squares), for a 90 nm-thick emitting layer NRS-PPV-based OLED.

The values for the singlet fraction for NRS-PPV as calculated using eq. (4.1) are presented in figure 4.17. The singlet fraction is in the range 8%-14%, almost independent of the experimental conditions but slightly emitting layer-thickness

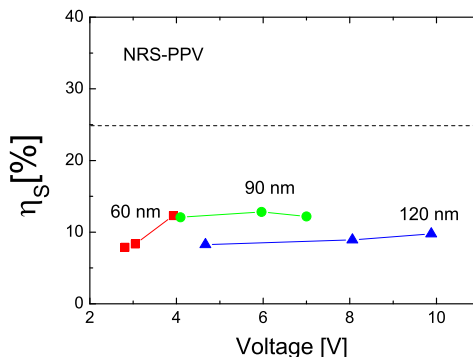


Figure 4.17: Calculated singlet fraction for NRS-PPV as a function of voltage for the three thicknesses: 60 nm (squares), 90 nm (circles) and 120 nm (triangles).

dependent. As for the PF- 0.5 mol%TAA case, the emitting layer thickness dependence of the singlet fraction is presently under investigation. The singlet fraction is smaller than the standard quantum statistical value (dashed line). A similar analysis performed on different, though nominally identical, pixels led to exactly the same value of η_S .

An additional way to test the consistency of the method, which was so far only applied to the NRS-PPV devices, is to compare the external quantum efficiency (EQE) which would follow from the emission profile determined from our studies, as a function of the voltage and the layer thickness, to experimental EQE values as measured in an integrating sphere set-up. The calculated EQE values follow from the equation: $\eta_{EQE} = \eta_{rec} \eta_S \eta_{PL,cavity} \eta_{out,EL}$, where η_{rec} is assumed to be unitary, $\eta_{PL,cavity} \cdot \eta_{out}$ follows from the calculated microcavity effect on the measured photoluminescence quantum efficiency of $\eta_{PL} = 0.25$, and η_{out} is the outcoupling efficiency as calculated by our microcavity model.

Before comparing the measured and calculated EQE values we discuss the possible experimental uncertainties and calculation inaccuracies. In order to avoid collecting light waveguided to the OLEDs' edges, black tape is applied to cover these parts while carrying out integrating sphere measurements. Although a calibration routine is run, the presence of the black tape can introduce experimental uncertainty. Moreover, in order to get a sufficiently large signal-to-noise ratio, long integration times (i.e: 20 scans for 20 seconds: ~ 7 minutes) needed to be applied. This introduces the possibility of non-stable light emission over time. Taking both uncertainty sources into account, we estimate an error margin in the measured EQE values of ~ 10 to 20%. In order to investigate the error margin in the calculated EQE values, we studied the sensitivity of the calculated outcoupling efficiency to small variations on the light-emission profiles. In figure 4.18 the calculated value of the product $\eta_{PL,cavity} \cdot \eta_{out,EL}$ is presented as

a function of the dipole position within a 60 nm-thick emitting layer. The reconstructed light-emission profiles as a function of the applied voltage are also shown in the same figure. Since the emission profiles are located at a steep part of the $\eta_{\text{PL,cavity}} \cdot \eta_{\text{out,EL}}$ curve, a small variation in the dipole position can lead to a relatively large variation in the outcoupling efficiency value. We estimate that the realistic uncertainty in the EQE is approximately 20%.

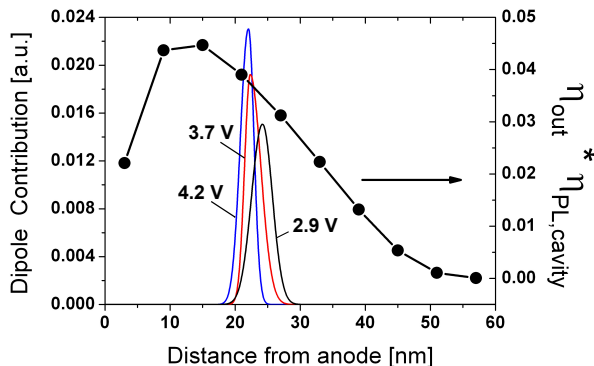


Figure 4.18: Reconstructed light-emission profiles and outcoupling efficiency, $\eta_{\text{PL,cavity}} \cdot \eta_{\text{out,EL}}$, as a function of the dipole position for an NRS-PPV-based OLED with a 60 nm thick emitting layer.

The measured and calculated EQE values are compared in figure 4.19. We find a factor of two difference between the calculated and measured values of external quantum efficiencies. The measured light intensity is larger than than expected from our calculations. The difference is significant even when taking the experimental calculational uncertainty into account. We notice that the experimental values measured are in good agreement with the results published by Tanase and co-workers⁴⁷ for similar 95 nm-thick NRS-PPV devices, although in that study no PEDOT:PSS was employed. In that case η_{EQE} was found to rapidly increase in the range $\sim 0 - 2\%$ for increasing applied voltage, in a comparable voltage range as for our measurements. A possible reason for the mismatch between the calculated and measured EQE values could be related to the specific value of PL quantum efficiency employed in the microcavity calculations. This value, equal to 0.25, was experimentally measured as already described in chapter 2. Measurements of the absolute PLQE for PPVs have been argued⁴⁸ to be possibly affected by the presence of oxidation products, such as the carbonyl group $-\text{C}=\text{O}$. The interaction between an exciton and this electronegative group would generate a charge-transfer state, which is characterized by a much lower radiative decay rate, compared to an exciton.⁴⁸ Although the PLQE measurements were carried out in an integrating sphere with a nitrogen flow, oxidation effects can't be excluded. In contrast, in OLEDs the PPV layer is protected against long-term oxidation effects by the presence of encapsulation layers. For a 90 nm-thick emitting layer device,

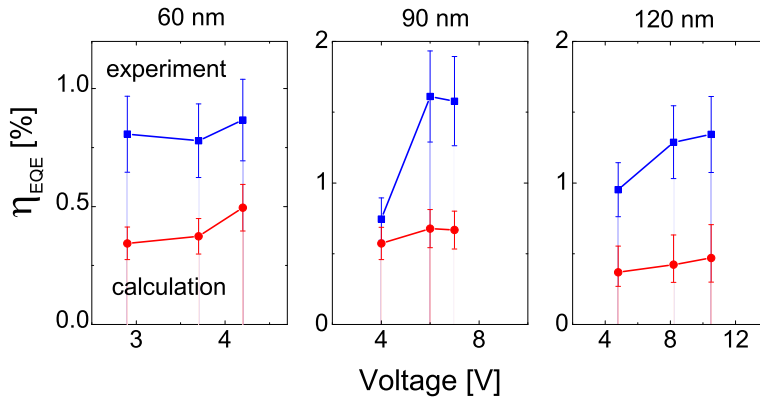


Figure 4.19: Comparison between the experimentally measured (squares) and calculated (circles) external quantum efficiency for NRS-PPV devices with emitting layer thicknesses values indicated on top of each graph, as a function of the applied voltage.

assuming a recombination probability $\eta_{\text{rec}} = 1$, $\eta_{\text{out,EL}} = 0.23$, $\eta_{\text{rad}} = 0.25$ and assuming an average value for the singlet fraction equal to 0.12 (see figure 4.17), an external quantum efficiency equal to 0.0067 is obtained. A factor 2 error in the PLQE estimation would have only a slight effect on the reconstructed light-emission profile, due to the change of the microcavity-dependent radiative decay probability. Furthermore, the change in the calculated singlet fraction is expected to be minor, due to the fact that the EL outcoupling efficiency is “normalized” with the outcoupling efficiency in reverse PL. Therefore the net effect of a factor 2 error in the PLQE estimation on the EQE would be relatively large, viz. a roughly linear change in the calculated EQE value.

4.7 Conclusions

We have extended the method to determine the exciton singlet : triplet ratio in OLEDs introduced by Segal *et al.*⁷ to single layer OLEDs, by taking the difference between the light-outcoupling efficiencies in EL and PL experiments into account. The method used to model the outcoupling efficiency in EL and PL experiments could also be employed to refine the analyses used in previous studies of the singlet fraction.^{1,10,4} E.g., the studies of Cao *et al.*¹ and Wilson *et al.*⁴ for OC₁C₁₀-PPV and PtOEP, respectively, which are both based on ratios of measured EL and PL intensities, give rise to a seemingly layer thickness dependent singlet fraction.

The analysis has been applied to blue-emitting polyfluorene-based copolymer devices containing 0.5 mol% and 7.5 mol% hole-transporting TAA monomer units and red-emitting NRS-PPV-based. The PF-7.5 mol% TAA copolymer is an

application-relevant material in which the TAA units give rise to an optimized hole injection and electron-hole mobility balance. That material, as well as NRS-PPV, has been intensively studied in the literature. Employing the EL emission profile as obtained from the measured angular, wavelength and polarization dependent emission intensity using the method developed in chapter 2, and using the PL emission profile as obtained from optical modeling, it is found that taking the actual EL and PL outcoupling efficiencies into account leads to a singlet fraction which is for all materials in the range 8 – 25%, essentially independent of the applied voltage. In a recent work, Kersten *et al.*¹⁹ have shown that significant deviations (either positive or negative) from the standard-statistical value of singlet exciton fraction could be expected, depending on the frequency of the hyperfine field precession as compared to the rate of singlet exciton formation. Such deviations are generally accompanied by significant magneto-electroluminescence effects.

For PF-TAA-based devices, η_S is found to be quite strongly layer thickness dependent, while for NRS-PPV-based devices no layer thickness dependence is found. For this reason, and in view of the finding that for NRS-PPV devices the EQE as measured directly is approximately a factor of 2 larger than the EQE as calculated from the emission profiles, further refinement of these studies will be needed.

In spite of the uncertainties related to the finding of a thickness dependent value of η_S and concerning the EQE of the devices, the study shows that the maximum attainable internal quantum efficiency of polymer OLEDs based on the materials analyzed is thus severely limited by the unfavorable spin-statistics of the exciton formation process.

4.8 References

1. Y. Cao, I. D. Parker, G. Yu, C. Zhang and A. J. Heeger, *Nature* **397**, 414 (1999).
2. J. S. Kim, P. K. H. Ho, N. C. Greenham and R. H. Friend, *J. Appl. Phys.* **88**, 1073 (2000).
3. M. Wohlgenannt, K. Tandon, S. Mazumdar, S. Ramasesha and Z. V. Vardeny, *Nature* **494**, 409 (2001).
4. J. S. Wilson, A. S. Dhoot, A. J. A. B. Seeley, M. S. Khan, A. Köhler and R. H. Friend, *Nature* **413**, 828 (2001).
5. A. S. Dhoot, D. S. Ginger, D. Beljonne, Z. Shuai and N. C. Greenham, *Chem. Phys. Lett.* **360**, 195 (2002).
6. M. Wohlgenannt, X. M. Jiang, Z. V. Vardeny and R. A. J. Janssen, *Phys. Rev. Lett.* **88**, 197401 (2002).
7. M. Segal, M. A. Baldo, R. J. Holmes, S. R. Forrest and Z. G. Soos, *Phys. Rev. B* **68**, 075211 (2003).
8. T. Virgili, G. Cerullo, C. Gadermaier, L. Lüer, G. Lanzani and D. D. C Bradley, *Phys. Rev. Lett.* **90**, 247402 (2003).
9. C. Yang, Z. V. Vardeny, A. Köhler, M. Wohlgenannt, M. K. Al-Suti and M. S. Khan, *Phys. Rev. B* **70**, 241202(R) (2004).
10. C. Rothe, S. M. King and A. P. Monkman, *Phys. Rev. Lett.* **97**, 076602 (2006).
11. A. P. Monkman, C. Rothe and S. M. King, *Proc. IEEE* **97**, 1597 (2009).
12. C. Adachi, M. A. Baldo, M. E. Thompson and S. R. Forrest, *J. Appl. Phys.* **90**, 5048 (2001).
13. G. He, M. Peiffer, K. Leo, M. Hofmann, J. Birnstock, R. Pudzich and J. Salbeck, *Appl. Phys. Lett.* **85**, 3911 (2004).
14. M. Reufer, M. J. Walter, P. G. Lagoudakis, A. B. Hummel, J. S. Kolb, H. G. Roskos, U. Scherf and J. M. Lupton, *Nat. Mater.* **4**, 340 (2005).
15. Z. Shuai, D. Beljonne, R. J. Silbey and J. L. Brédas, *Phys. Rev. Lett.* **84**, 131 (2000).
16. M. N. Kobrak and E. R. Bittner, *Phys. Rev. B* **62**, 11473 (2000).
17. S. Karabunarliev and E. R. Bittner, *Phys. Rev. Lett.* **90**, 057402 (2003).
18. A. Kadashchuk, A. Vakhnin, I. Blonski, D. Beljonne, Z. Shuai, J.-L. Brédas, V. I. Arkhipov, P. Heremans, E. V. Emelianova and H. Bässler, *Phys. Rev. Lett.* **93**, 066803 (2004).
19. S. P. Kersten, A. J. Schellekens, B. Koopmans and P. A. Bobbert, *Phys. Rev. Lett.* **106**, 197402 (2011).
20. J. Kalinowski, J. Godlewski and J. Glinski, *J. Lumin.* **17**, 467 (1978).

21. J. Glinski, J. Godlewski and J. Kalinowski, *Mol. Cryst. Liq. Cryst.* **48**, 1 (1978).
22. J. Kalinowski, *Synth. Metals* **64**, 123 (1994).
23. S. L. M. van Mensfoort, M. Carvelli, M. Megens, H. Greiner, D. Wehenkel, M. Bartyzel, R. A. J. Janssen and R. Coehoorn, *Nature Photonics* **4**, 329-335 (2010).
24. R. Coehoorn, S. Vulto, S. L. M. van Mensfoort, J. Billen, M. Bartyzel, H. Greiner and R. Assent, *Proc. SPIE* **6192**, 61920O (2006).
25. N. C. Van der Vaart, H. Lifka, F. P. M. Budzelaar, J. E. J. M. Rubingh, J. J. L. Hoppenbrouwers, J. F. Dijkman, R. G. F. A. Verbeek, R. van Woudenberg, F. J. Vossen, M. G. H. Hiddink, J. J. W. M. Rosink, T. N. M. Bernards, A. Giraldo, N. D. Young, D. A. Fish, M. J. Childs, W. A. Steer, D. Lee, D. S. George, *J. Soc. Inf. Disp.* **13**, 9 (2005).
26. S. L. M. van Mensfoort, S. I. E. Vulto, R. A. J. Janssen and R. Coehoorn, *Phys. Rev. B* **78**, 085208 (2008).
27. S. L. M. van Mensfoort, J. Billen, S. I. E. Vulto, R. A. J. Janssen and R. Coehoorn, *Phys. Rev. B* **80**, 033202 (2009).
28. R. J. de Vries, S. L. M. van Mensfoort, V. Shabro, S. I. E. Vulto, R. A. J. Janssen and R. Coehoorn, *Appl. Phys. Lett.* **94**, 1 (2009).
29. L. C. Palilis, D. G. Lidzey, M. Redecker, D. D. C. Bradley, M. Inbasekaran, E. P. Woo and W. W. Wu, *Synth. Met.* **111**, 159 (2000); M. Inbasekaran, E. Woo, W. Wu, M. Bernius and L. Wujkowski, *Synth. Met.* **111**, 397 (2000).
30. S. Doi, T. Yamada, Y. Tsubata and M. Ueda, *Proc. SPIE* **5519**, 161 (2004).
31. D. Poplavskyy, W. Su and F. So, *J. Appl. Phys.* **98**, 014501 (2005) and references therein.
32. S. Harkema, R. A. H. J. Kicken, B. M. W. Langeveld-Voss, S. L. M. van Mensfoort, M. M. de Kok and R. Coehoorn, *Org. Electron.* **11**, 755 (2010).
33. J. Cabanillas-Gonzalez, M. R. Antognazza, T. Virgili, G. Lanzani, C. Gadermaier, M. Sonntag and P. Strohsriegel, *Phys. Rev. B* **71**, 155207 (2005).
34. D. E. Markov and P. W. M. Blom, *Phys. Rev. B* **72**, 161401(R) (2005).
35. H. Greiner and O. J. F. Martin, *Proc. SPIE* **5214**, 249 (2004).
36. It was found after the publication of Ref. 23 that an angular-dependent correction should be applied to the measured EL intensities. The corrected profiles are shown in figure 4.4. For the 100 and 130 nm devices, the emission peak is found to be at a slightly larger distance from the anode, for all three voltages considered, whereas for the 160 nm device the change of the profile is very small.
37. N. C. Giebink and S. R. Forrest, *Phys. Rev. B* **77**, 235215 (2008).
38. E. A. Meulenkaamp, R. van Aar, J. J. A. M. Bastiaansen, A. J. M. van den Biggelaar, H. Börner, K. Brunner, M. Büchel, A. van Dijken, N. M. M. Kiggen, M. Kilitziraki, M. M. de Kok, B. M. W. Langeveld, M. P. H. Ligter, S. I. E. Vulto, P. van de Weijer, S. H. P. M. de Winter, *Proc. SPIE* **5464**, 90 (2004).

39. R. Coehoorn and S. L. M. van Mensfoort, *Phys. Rev. B* **80**, 085302 (2009).
40. J. J. M. van der Holst, F. W. A. van Oost, R. Coehoorn and P. A. Bobbert, *Phys. Rev. B* **80**, 235202 (2009).
41. C. Groves and N. C. Greenham, *Phys. Rev. B* **78**, 155205 (2008).
42. A. Köhnen, N. Riegel, J. H.-W. Kremer, H. Lademann, D. C. Müller and K. Meerholtz, *Adv. Mater.* **21**, 879 (2009).
43. J. J. M. van der Holst, M. A. Uijtewaal, B. Ramachandhran, R. Coehoorn, P. A. Bobbert, G. A. de Wijs and R. A. de Groot, *Phys. Rev. B* **79**, 085203 (2009).
44. D. Beljonne, A. Ye, Z. Shuai and J.-L. Brédas, *Adv. Funct. Mater.* **14**, 684 (2004).
45. J. Kalinowski, *Organic Light Emitting Diodes: Principles, Characteristics and Processes* (Dekker, New York, 2005).
46. D. E. Markov and P. W. M. Blom, *Appl. Phys. Lett.* **87**, 233511 (2005).
47. C. Tanase, J. Wildeman and P. W. M. Blom, *Adv. Funct. Mat.* **15**, 2011 (2005).
48. M. Pope and C. E. Swenberg, *Electronic Processes in Organic Crystals and Polymers*, Oxford University Press, New York (1999).

Exciton formation and light emission near the organic-organic interface in small-molecule based double-layer OLEDs

After having studied single emitting-layer OLEDs via light-emission profile reconstruction, in this chapter the photophysics of organic-organic interfaces is investigated, as a first step towards the analysis of white-light multilayer OLEDs. We analyze the efficiency and emission color of small-molecule based double-layer OLEDs based on 4,4'-bis[1-naphthyl(phenyl)amino]-1,1'-biphenyl (α -NPD) and bis(2-methyl-8-quinolinato)(4-phenylphenolato)aluminum (BALq) by studying the charge transport and photophysics near the organic-organic interface between the emitting layers. For that purpose, the light-emission profile is reconstructed from full angle, wavelength and polarization dependent electroluminescence spectra. By increasing the thickness of the BALq layer from 100 to 300 nm, at a fixed 160 nm α -NPD layer thickness, the emission color is found to vary from deep blue to green, yellow-green, white and back to blue. We demonstrate that this is due to a gradual emission profile shift, in combination with a wavelength and layer thickness dependent light outcoupling efficiency. This shift, from an approximately 20 nm-wide zone on the α -NPD-side of the interface to a narrow zone on the BALq-side of the interface, gives rise to a changing balance between the contributions from BALq excitons, α -NPD excitons and charge-transfer excitons. It also contributes to a pronounced layer thickness dependence of the external quantum efficiency. The shift is explained by a charge transport and recombination model.

5.1 Introduction

Organic light-emitting diodes (OLEDs) are a promising option for energy-efficient solid-state lighting.¹ In particular, multilayer structures composed of emitting layers, charge transport and injection layers are employed as the paradigm for efficient electron-hole pair formation and photon generation.² Therefore, the photophysical processes occurring near organic-organic interfaces have been a subject of intensive investigation.^{3–13} A key process is the generation of charge-transfer (CT) or exciplex states, in which the bound electron-hole state is delocalized over two different molecules at either side of the organic-organic interface. When the nature of the complex is mainly ionic this is called a charge-transfer state, while it is called an exciplex when its nature is mainly covalent.¹⁴ In the remainder of this chapter we will use for simplicity only the term CT state to indicate such a complex. CT states are characterized by a red-shifted emission spectrum as compared to the spectrum resulting from the radiative decay of excitons formed in the bulk of the two layers,¹⁰ and by a longer lifetime.¹³ Light emission from a double-layer OLED can thus in general originate from a superposition of the pure exciton emission from the bulk of the layers at both sides of the interface and emission from CT states.¹⁰ The balance of these three components can strongly affect the device efficiency and emission color-point. It is mainly determined by the electron and hole mobilities at both sides of the interface, the energy barriers at the interface and the diffusion length of excitons generated at either side of the interface. In the case of double-layer OLEDs formed by a blue and a green emitting layer, CT state emission can give rise to an additional red component in the emission spectrum. Under proper conditions white light emission characterized by a high color rendering index (CRI) is then possible.⁵

The photophysics near the interface between a hole-transport layer (HTL) and an electron-transport layer (ETL) has been investigated extensively. Previous studies have focussed mainly on layer structures where large hole and electron energy barriers, Δ_h and Δ_e , are present at the HTL/ETL interface.^{5,8,9} The high concentration of charges and excitons at the interfaces facilitates in this case the formation of CT states. Within a simplified picture, which neglects the effect of energetic disorder, the CT state energy may be calculated as

$$E_{CT} = \frac{E_{g,1} + E_{g,2}}{2} - \frac{\Delta_h + \Delta_e}{2} - E_{CT,b}, \quad (5.1)$$

with $E_{g,1}$ and $E_{g,2}$ the single-particle energy gaps in the hole and electron transport layers, respectively, and $E_{CT,b}$ the CT state binding energy. CT state formation is favorable if E_{CT} is smaller than the exciton energy in both layers, given by $E_{ex,1} = E_{g,1} - E_{b,1}$ and $E_{ex,2} = E_{g,2} - E_{b,2}$, with $E_{b,1}$ and $E_{b,2}$ the exciton binding energies. One may thus expect that CT state formation occurs when the energy barriers are sufficiently high, thereby compensating for the fact that in general $E_{CT,b}$ is smaller than $E_{b,1}$ and $E_{b,2}$. The presence of energetic disorder and thermal activation is expected to give rise to a certain degree of coexistence between excitons and CT states. Consistent with this picture, a systematic analysis⁹ led to the observation that upon increasing the energy barriers at the organic-organic

interface the CT state generation probability studied at similar driving conditions increases only gradually, while at the same time only a gradual decrease of the external quantum efficiency (EQE) was observed.

In the case of small energy barriers at the HTL/ETL interface, exciton formation is not necessarily located near the interface, and CT states may be less stable than excitons. Detailed studies of the electron-hole recombination profile are needed to elucidate the dependence of the EQE on the energy barriers. Such studies were carried out by Matsumoto *et al.*,^{11,13} who investigated systematically CT state formation in OLEDs containing a mixed HTL:Alq₃ emitting layer (where Alq₃ is tris(8-hydroxyquinolino)aluminium) and with Alq₃ as the electron-transporting layer. For a range of HTL materials with similar energy gaps but with varying HOMO energies, a photoluminescence (PL) study for the mixed HTL:Alq₃ layers showed that the CT state formation rate indeed increases with increasing electron and hole energy barriers, as expected from Eq. (1). However, surprisingly large nominal values of Δ_h and Δ_e were found to be required. A boundary case, showing some CT state formation, was found to be a mixed system containing 4,4'-bis[1-naphthyl(phenyl)amino]-1,1'-biphenyl (α -NPD) as the hole transporting molecule, with $\Delta_h = 0.4$ eV and $\Delta_e = 0.7$ eV. Consistent with this finding, the authors found also only little evidence of CT state formation at a pure α -NPD / Alq₃ interface: the EL efficiency of bilayer 20 nm α -NPD/50 nm Alq₃ OLEDs was found to be as expected for the case of emission in the bulk of the Alq₃ layers, approximately 1%, instead of being reduced as a result of inefficient CT state emission.¹¹ This picture was supported by the results of a subsequent study using a thin "sense" layer of rubrene, co-evaporated within the Alq₃ layer, to reconstruct the profile.¹³ The results of this study were interpreted in terms of an exponentially decaying approximately 15 nm wide emission profile in the Alq₃ layer adjacent to the interface. This work suggests that the probability of CT state formation as probed in PL and EL experiments does not follow directly from the nominal HOMO and LUMO energies of the constituent organic semiconductors, and that the availability of a direct method of probing the emission profile can be of great help in elucidating the exciton formation processes near organic-organic interfaces in OLEDs.

In this chapter, we demonstrate the successful application of an alternative technique for studying the photophysical processes near organic-organic interfaces, based on a recently developed method to reconstruct the light-emission profile from the measurement of angle-, wavelength- and polarization-dependent electroluminescence spectra.^{15,16} We investigate emission near the interface between α -NPD and an electron-transporting bis(2-methyl-8-quinolino)(4-phenylphenolato)aluminum (BALq) layer. The OLED structure is:

glass / ITO / HIL / α -NPD / BALq / EIL / Al,

containing an 125 nm indium-tin-oxide (ITO) anode, a 50 nm NHT5:6% NDP2 *p*-doped hole injection layer (HIL), a 50 nm *n*-doped NET5:4% NDN1 electron injection layer (EIL) and a 100 nm aluminium cathode. The thickness of the BALq layer is varied from 100 to 300 nm, whereas the α -NPD layer thickness is kept fixed at 160 nm. The *n*-doped and *p*-doped layer materials are supplied

by Novalde, AG. Both layers function effectively as high-conductivity electrode layers which facilitate charge carrier injection as a result of their relatively high and low Fermi energy with respect to the vacuum level, as compared to that of Al and ITO, respectively (see also section 4). We have chosen BALq as the electron transport layer in this study, instead of the more intensively investigated material Alq₃, as from a recent study in our group a detailed electron transport model for BALq is available, which includes the effects of the structural disorder on the charge carrier density, electric field and temperature dependence of the disorder.¹⁷ We make use of the results of this study within a charge-transport and recombination model which is developed in order to analyze the measured shapes of the emission profile. Developing an analogous experimentally validated electron and hole charge transport model for Alq₃ is expected to be more difficult. Firstly, Alq₃ molecules are known to exhibit two isomeric forms, giving rise to slightly different LUMO energies whose presence would give rise to a rather complicated shape of the density of states. Secondly, Alq₃ films are known to show crystallization, depending on the preparation conditions, possibly affecting the charge transport.¹⁸ In contrast, evaporation deposition at room temperature of films of BALq, which has a lower molecular symmetry, is known to lead to an amorphous structure. As an electron transport and hole-blocking material, BALq is known to allow for high lifetimes. Values on the order of 160000 hours at a brightness of 100 cd/m² have been reported^{19,20}. Previous work on α -NPD/BALq based devices has already suggested that emission can take place at both sides of the interface, based on the observation of emission spectrum variations with the BALq thickness.^{7,12} In particular, it was found that in OLEDs with the layer structure ITO/ α -NPD/BALq/LiF/Al, with comparably thin α -NPD and BALq layers, α -NPD as well as BALq contributions are present in the electroluminescence (EL) spectrum, and that by increasing the BALq thickness the BALq contribution to the EL spectrum becomes dominant. This was qualitatively attributed to a shift of the exciton formation profile. In this chapter we show for the first time that the light-emission profile across an organic-organic interface in a bilayer OLED can be accurately reconstructed from the measured emission, without making use of a sense layer. A shift of the emission region across the interface with increasing thickness of the BALq layer, from the α -NPD side to the BALq side, is also observed in our α -NPD/BALq devices. For specific BALq layer thicknesses, CT state formation and radiative decay is found to play a crucial role, leading to white emission. We also present a quantitative analysis of the BALq layer thickness dependence of the external quantum efficiency (EQE), including the effect of the shifting balance between the emission from α -NPD, CT states and BALq. A comparison is given between the directly measured EQE and the EQE as calculated using the observed emission profiles. We note that a similar comparison between the calculated and measured EQE as a function of thickness of one of the layers in the microcavity has recently been presented by Meerheim *et al.*,²¹ viz. for a multilayer OLED in which the excitons are generated in a well-defined 20 nm-thin emitting layer. The EQE is then tuned by varying the distance of this layer from the metallic cathode by changing the thickness of the (non-emitting) electron transport layer. We now for the first time develop a comparison between the measured and calculated EQE

in a case where the thickness of the one of the (relatively thick) emitting layers is changed. This has the double effect of changing the exciton recombination profile and of changing the distance of the recombination zone to the metallic cathode. Finally, the observed shift is explained from a drift-diffusion charge-transport and recombination model, and a comparison is made between the calculated shapes of the exciton formation profile and the measured shapes of the emission profile.

In section 5.2 experimental and theoretical indications of CT state generation will be presented. In section 5.3 the reconstructed light-emission profiles are presented and analyzed, and a comparison is given between the directly measured EQE and the EQE as calculated using the observed emission profiles. In section 5.4 a charge-transport model is employed to describe the transport physics of the devices and to explain the observed reconstructed light-emission profile shift. A summary and conclusions are given in section 5.5.

5.2 Energy level structure, optical properties and emission color

In this section first the likeliness of CT state generation near the α -NPD/BAlq interface is discussed theoretically from the energy level structure and the calculated shape of the relevant molecular orbitals, and experimentally from the emission spectra obtained from a time-resolved photoluminescence study. Subsequently, strong indications of CT-state formation are provided from emission color-point measurements.

5.2.1 Molecular energy levels and orbital shape

The likeliness of CT state generation can already be judged from the energy level diagram near the α -NPD / BAlq interface, shown in figure 5.1. The highest occupied molecular orbital (HOMO) and the lowest unoccupied molecular orbital (LUMO) levels of the two molecules indicated represent an average of the following literature values: $\sim 5.2 - 5.6$ eV and $\sim 2.3 - 2.7$ eV, respectively, for α -NPD,^{22,23} and ~ 5.9 eV and ~ 2.9 eV,²⁴ respectively, for BAlq. The spread in the HOMO levels reported in the literature about α -NPD is directly reflected into a spread in the LUMO levels, since for both the cited works a substantially equal energy gap is added to the HOMO level to obtain the LUMO level. Due to the approximately 0.5 eV misalignment of the HOMO and LUMO levels of the two molecules, the generation of a bound state between an electron localized on BAlq and a hole localized on α -NPD is expected to be favorable, even when assuming a low binding energy for CT states (~ 0.2 eV or less) as compared to that for excitons (typically ~ 0.4 eV) due to the more delocalized wavefunction. The overall emission from this state is then expected to be significantly red-shifted as compared to that arising from the radiative decay of excitons generated in the bulk of the two layers. In order to further investigate the likeliness of CT state generation, we have performed Density Functional Theory (DFT) calculations of the HOMO and LUMO orbitals for α -NPD and BAlq molecules in vacuum. The DFT calculations

were performed at the B3LYP:TZP level, using the commercial software package Amsterdam Density Functional (ADF) from Scientific Computing & Modelling. As shown in figure 5.1, for both molecules the HOMO and LUMO orbitals are located on different parts of the molecule. This may be expected to favor the generation of a bound CT state formed by a hole on α -NPD and an electron on a BA1q neighbor molecule if their configuration is such that the HOMO of the α -NPD molecule is located more closely to the LUMO of the BA1q molecule than to the LUMO of the α -NPD molecule itself.

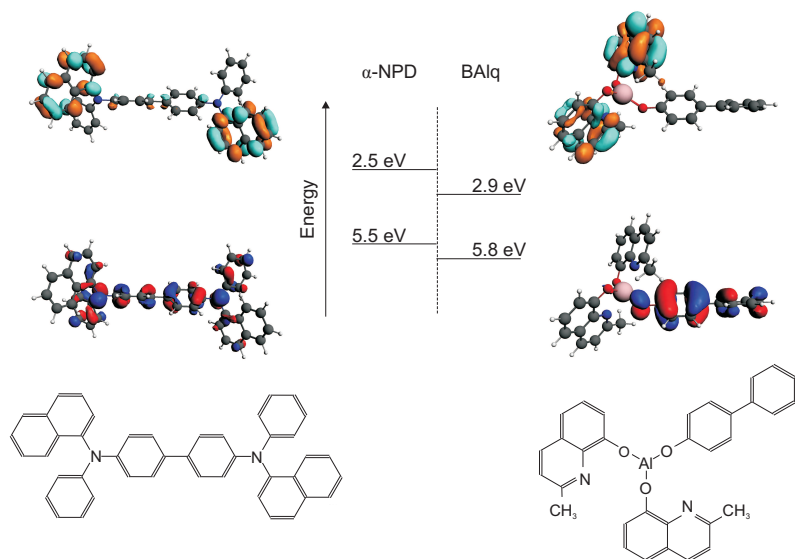


Figure 5.1: HOMO and LUMO energy levels for α -NPD and BA1q as obtained from the literature (see the text for the references), and calculated shape of the HOMO orbitals (bottom figures) and LUMO orbitals (top figures) for both molecules in vacuum, as obtained from DFT calculations (see text). The chemical structures of two molecules are also indicated on the bottom.

5.2.2 Time-resolved photoluminescence measurements

We have also investigated the likeliness of CT state generation at the α -NPD/BA1q interface by performing time-resolved photoluminescence (TRPL) experiments for co-evaporated α -NPD:BA1q (100 nm) layer on glass. The co-evaporation ratio between the two molecules is approximately 1:1. As a reference, also the emission from pure 50 nm α -NPD and BA1q layers on glass was measured. The TRPL measurements were performed employing an Edinburgh Instruments LP920 spectrophotometer equipped with a flash lamp pumped Q-switched Nd:YAG laser (350 nm excitation output). An intensified charge-coupled device (CCD) camera was used to record the emission spectra.

The measured PL spectra are shown in figure 5.2. The spectrum for the mixed layer is red-shifted as compared to that for the two pure layers, and characterized by a more strongly asymmetric tail in the red region. The measured emission-lifetime was found to be significantly longer (40 ns, monoexponential decay) for the emission from the mixed layer than for the emission from the pure α -NPD or BALq layers (≤ 3 ns and 9 ± 2 ns, respectively). These results suggest strongly that, at least in a mixed layer, CT exciton generation occurs.

The long lifetime of the CT state gives rise to an enhanced probability of non-radiative decay, which is expected to result in a relatively low EQE when a large fraction of the recombination events gives rise to CT state formation. The measured EQE provides support to this point of view, as shown in section 5.3.3.

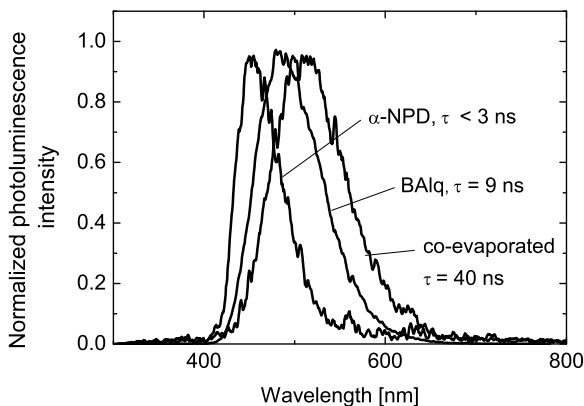


Figure 5.2: Measured photoluminescence spectra for a 50 nm-layer of α -NPD on glass, a 50 nm-layer of BALq on glass and 100 nm 50% α -NPD : 50% BALq co-evaporated layer on glass. The values for the decay times as obtained from the TRPL measurements are also given.

5.2.3 Current density and color-point variation with BALq layer thickness

Figure 5.3 shows the measured current density-voltage curves for the different devices studied. The curves were obtained using continuous or pulsed measurements (at 10 Hz, with a 1% duty-cycle) in order to avoid sample heating. The upper horizontal dashed line gives the current density above which sample heating made it necessary to carry out the pulsed measurements. The electroluminescence (EL) studies reported in this chapter were all carried out at a fixed current density of ~ 40 A/m², indicated by the lower horizontal dashed line. This fixed value is chosen such that sample heating and too long integration times during which

changes in the device performance could take place are avoided. At the fixed current density used, the brightness of the devices is approximately 50 cd/m^2 , slightly BALq-thickness dependent due to a change in the EQE which will be described in section 5.3.3.

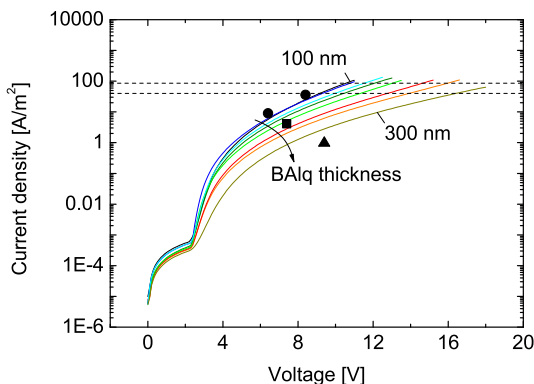


Figure 5.3: Current density - voltage curves measured for the different devices, with BALq thickness values of 100, 120, 140, 160, 180, 210, 240 and 300 nm. The curves were obtained using continuous and pulsed operation, as discussed in the main text. The upper dashed horizontal line gives the approximate current density below which no significant sample heating occurs during continuous operation, and the lower dashed line gives the current density at which the EL studies reported in this chapter were carried out. Below approximately 2.5 V, a small leakage current density, proportional to V, is obtained. The full symbols indicate the current density-voltage points as deduced from charge transport and recombination modelling, for the case of a 100 nm (circles), 160 nm (square) and 300 nm (triangle) BALq layer (see section 5.4).

In figure 5.4(a) the EL emission color-point as measured in the direction orthogonal to the device surface is presented (open spheres) in a CIE 1931 chromaticity diagram.²⁵ Different BALq layer thicknesses are found to give rise to different color points. Following the direction of the arrows, the BALq layer thickness varies as follows: 100, 120, 140, 160, 180, 210, 240 and 300 nm. The corresponding normalized EL spectra for three representative cases are shown in figure 5.4(b). The emission color varies from blue to sky-blue, yellowish green, cold white and blue again for the thickest sample. In devices where the α -NPD thickness was varied, the color point shift was almost negligible. The PL emission color of pure α -NPD and BALq and of 1:1 mixed α -NPD:BALq, for which the spectra were shown in figure 5.2, is blue, sky-blue and greenish, respectively. The closed spheres in figure 5.4(a) show the corresponding color points. It follows that the large red contribution observed in the electroluminescence for the devices with a 210 and 240 nm-thick BALq layer therefore can not be simply understood as a result of a superposition of the PL spectra from the two pure layers or from the pure layers

and CT-emission from the interface. We will show that the large red-shift may be understood as the combined effect of emission from CT states generated at the interface between the two organic emitting layers and a microcavity effect on the wavelength dependence of the light-outcoupling probability.

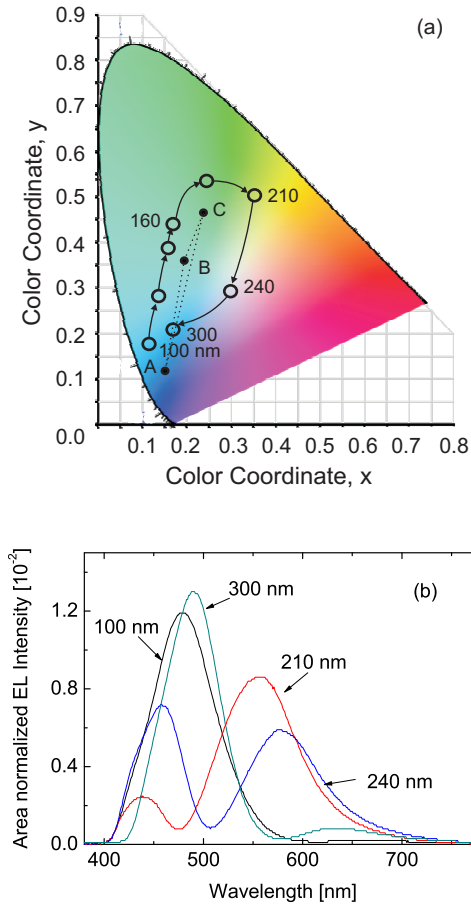


Figure 5.4: (a) CIE-1931 chromaticity diagram²⁵ showing the color coordinates (open circles) as measured for normal emission at $\sim 40 \text{ A/m}^2$ as a function of the BAQ device thickness (100, 120, 140, 160, 180, 210, 240 and 300 nm, increasing in the direction of the arrows). Full circles indicate the emission color points as derived from the photoluminescence spectra of α -NPD (A), BAQ (B) and CT excitons (C) shown in figure 5.2. (b) Normalized electroluminescence (EL) spectral intensity measured under normal emission direction for four selected BAQ layer thicknesses.

5.3 Light-emission profiles and external quantum efficiency

In this section an overview is given of the BALq thickness dependence of the reconstructed emission profiles. Subsequently, the reconstructed profiles are used to calculate the EQE of the devices, which is compared to the EQE as measured using an integrating sphere spectrometer.

5.3.1 Method

In order to reconstruct the light-emission profile across the organic-organic interface we have developed an extension of an approach we already introduced for a single emitting-layer device, presented in ref. 15. It involves a least-squares minimization of a weighed difference between the experimental spectra, measured as a function of the angle and the polarization, and modeled emission spectra. The experimental and modeled spectra are both normalized over the sum of the intensities, in order to enhance the sensitivity to the lower-intensity tails of the spectrum.¹⁵ The OLED stack is modeled as an optical microcavity, using a computer simulation tool, LIGHTEX, developed at Philips Research Aachen.²⁶ The simulations include optical absorption in the emitting layer (“self-absorption”) and the microcavity effect on the ratio of the radiative and non-radiative decay rates, as described in ref. 15. Self-absorption is taken into account by assuming that the dipoles are located in a very thin, 2 nm-wide, emissive and non-absorbing layer, surrounded by two absorbing layers characterized by the same complex refractive index as the emissive layer.

The calculated emission spectra are derived from incoherently oscillating dipoles. Three emitting sources are considered, described by different separately normalized “source spectra” and by a different radiative decay probability: emission from the α -NPD layer, emission from the BALq layer and CT state emission. The source spectra are assumed to be equal to the photoluminescence (PL) spectra shown in figure 2, which we measured on samples of pure α -NPD, BALq and on a co-evaporated 1:1 mixed layer on glass. For α -NPD and BALq the radiative decay probability in layers of infinite thickness (i.e. before correcting their values for the presence in a microcavity,²⁷ η_{rad}) is assumed to be equal to the photoluminescence quantum yield (PLQE, η_{PL}) as obtained by Kawamura *et al.*,²⁸ viz. 0.29 and 0.42, respectively. The orientation of the oscillating dipoles is assumed to be random within each layer. Support for this assumption was obtained from ellipsometry measurements, using a Woollam Variable Angle Spectroscopic Ellipsometer (VASE), which for both materials revealed an essentially isotropic complex refractive index. For each material, the measurement was performed on three samples, made by evaporating a 80, 100 and 120 nm thick organic layer on quartz. The resulting dispersion curves, presented in appendix A, are a best fit to the data obtained for the three thickness values. Little is known about the PL quantum yield from CT states. CT states are characterized by a longer lifetime, so that the radiative decay rate is reduced and non-radiative decay processes will become more effective. When analyzing the emission profiles, we somewhat arbi-

trarily have assumed that this value is 0.1, smaller than the smallest of the PLQE values of α -NPD and BA1q. The consequences for the reconstructed profiles will be examined in more detail in the next session. Furthermore, the value of the PLQE efficiency of the CT states affects the EQE that is calculated from the emission profiles, as discussed in section 5.3.3.

The wavelength, angle and polarization dependent radiance of the light emitted from the OLEDs is measured (in units $\text{Wm}^{-2}\text{nm}^{-1}\text{sr}^{-1}$) using a Melcher Autronic Display Metrology System (DMS). The use of a glass hemisphere placed on the glass side of the OLED allows us to detect external light emission up to angles of 70° , in steps of 2° . This makes it possible to detect internal emission under angles that would otherwise give rise to total internal reflection. An index-matching fluid is applied in between the hemisphere and the OLED, with the same refractive index as the glass substrate, in order to make proper optical contact. The emission is measured in 5 nm steps in the 450 to 600 nm wavelength (λ) range, and for s and p polarization. The emission is described as a superposition of three functions: a single-peaked function on both sides of the interface and a delta-function describing the contribution from the CT states. The shape of the single-peaked functions which describe the emission from the α -NPD and BA1q layers is parameterized in a manner introduced in ref. 15, viz. by three parameters which control the peak position, width and asymmetry.

5.3.2 Reconstructed light-emission profiles

Figure 5.5 shows the BA1q layer thickness dependent reconstructed light-emission profiles across the α -NPD/BA1q interface. The figure shows that the emission originates in all cases from positions close to the organic-organic interface, at a maximum distance of 50 nm. For thin BA1q layers the emission originates predominantly from the α -NPD side of the interface, giving rise to a peaked profile centered at 20 nm from the interface, with only a relatively small CT state emission contribution originating from the interface. As the BA1q layer thickness increases, the light-emission profile shifts gradually to the interface until for BA1q layer thicknesses in the range 160 to 240 nm the light originates predominantly from emission at the interface. If the BA1q layer thickness is further increased, to 300 nm, the light is generated at the interface and at the BA1q side of the interface. Since a CT state contribution is almost absent in the 100-140 nm range and is (almost) the only contribution in the range 160-210 nm, a change in the PLQE of the CT states will in these cases have no effect on the reconstructed profiles. For the 240 and 300 nm thick case, where we found a finite contribution from the CT states, a small change of the CT PLQE value around the assumed value of 10% will to a good approximation result in an inversely proportional change in the CT state contribution.

The fit-profile approach used to reconstruct the emission profile in the bulk of the two layers can provide at least a fair description of its shape. First, one may expect from the physics of the charge transport, exciton generation and diffusion process that the emission profile in the bulk of each layer is indeed single-peaked. Second, the profile assumed makes it possible to optimize the

first three moments of the distribution, viz. the average, variance and skewness. Nevertheless, one may ask whether sufficient freedom has been allowed. In order to investigate this, we have also calculated reconstructed profiles using a least-squares optimization method with as degrees of freedom the dipole intensities on a dense (typically 5 to 10 nm) grid in each layer, and with as the only constraint that the dipole weights must be non-negative. The details of the method have been discussed in ref. 16. The general trend as observed from this approach is equal to that shown in figure 5.5, viz. emission from regions with the same widths at either side of the interface and a shift of the light-emission profile from the α -NPD side to the BALq side of the interface. Also, a similar changing balance is obtained between the three contributions. However, the profiles obtained are spiky, instead of single-peaked. We regard this as an artifact which is due to the too high number of degrees of freedom. The emission intensity from neighboring grid points is to a large extent linearly related, so that already a low level of realistic experimental noise makes it impossible to resolve their contributions. The resulting limitations of unconstrained methods may be mathematically analysed by studying the condition number of the matrix which expresses the emission intensities originating from each dipole position.¹⁵ It is possible to improve the smoothness of the profile obtained by making use of more advanced approaches, such as the Tikhonov method.¹⁶ However, this can give rise to an overestimation of the width of the profile.¹⁶ Therefore, we regard for the systems studied the fit profile method used as more suitable.

The major factors affecting the uncertainty in the shape of the reconstructed profiles are the accuracy with which the complex refractive index for each material and the thickness of each layer are known. In order to reduce the uncertainty related to possible errors in these quantities, we have carried out the analyses using the thickness of each layer as obtained from a least-squares fit to the measured EL intensities. In ref. 15 (figure 2 in the Supplementary Information) the application of such a procedure was demonstrated. For all devices, we find for the BALq layer thickness a 40 nm discrepancy between the nominal and optimized thickness. Transmission Electron Microscopy (TEM) analysis of test samples produced in the same deposition system confirmed such a discrepancy. Some uncertainty in the profiles is also due to the approximate treatment of the effect of self-absorption as discussed in section 3.1 and to the assumptions made on the PL quantum efficiency and on the shape of the “source spectrum” of each layer.

As a second consistency check we compared the emission color point as measured in an integrating-sphere set-up to the color-point of angle-integrated emission as calculated from the light-emission profiles reconstructed. The calculated color-point variation was found to be similar to the measured one, although more extreme, as could be expected by the rather extreme reconstructed change in the emission profile: from emission only from the α -NPD layer for the thinnest devices, to emission only from CT states, finally to a mix of CT state and BALq exciton emission for the thickest devices.

Figure 5.6 shows the integrated contributions from emission from α -NPD excitons, BALq excitons and CT states. The analysis reveals a quite distinct transition from the BALq thickness range 100-140 nm for which α -NPD emission is domi-

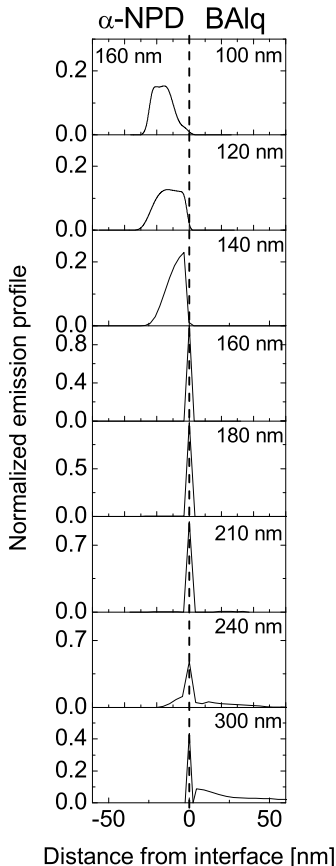


Figure 5.5: Reconstructed light-emission profiles as a function of the distance from the interface, for different values of the BA1q thickness. The α -NPD layer is located at negative distances from the interface, the BA1q layer at positive values. The BA1q thickness varies as indicated in the figure, while the α -NPD thickness is in all cases 160 nm. CT state emission is located exactly at the interface and it is indicated in the figure as a triangular region with a 4 nm-basis.

nant, to the thickness range 160-240 nm where CT state emission is dominant. For to the thickest BA1q case (300 nm) approximately half of the emission is due to CT states and half to BA1q excitons. We conclude that by increasing the BA1q thickness, the balance between the three contributions changes significantly. The above mentioned analysis of the color point variation as a function of the BA1q thickness may suggests that the change in exciton and CT state contribution as

a function of the BAQ thickness is actually slightly smoother than obtained from the light-emission profiles.

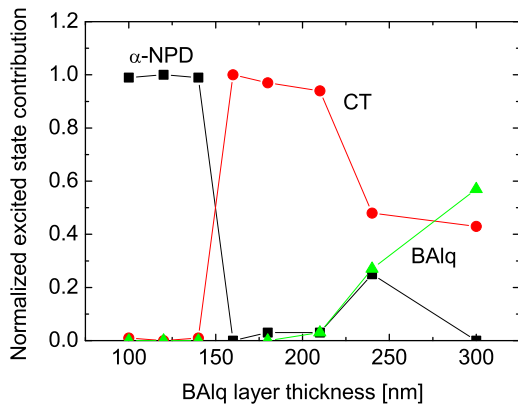


Figure 5.6: Excited state contributions to the measured EL spectra from α -NPD excitons (squares), BAQ excitons (triangles) and CT states (full circles), as determined from the analysis of the light-emission profiles.

5.3.3 External quantum efficiency

Figure 5.7 (full dots) shows the BAQ thickness dependence of the EQE, measured in an integrating sphere spectrometer. The experiment was carried out using a LabSphere LMS-200 20 inch Light Measurement Integrating Sphere system with integrated calibration lamp and electrode-addressing contacts. The error bars show the uncertainty as derived from measurements on four nominally identical devices. In the same figure, the open triangles and squares indicate the calculated value of the EQE as obtained in the following way from the measured emission profile. We express the EQE as $\eta_{\text{EQE}} = \eta_{\text{rec}}\eta_{\text{S}}\eta_{\text{rad}}\eta_{\text{out}}$, i.e. as a product of the electron-hole recombination efficiency η_{rec} , the singlet fraction η_{S} , the radiative decay probability η_{rad} , and the light-outcoupling efficiency η_{out} . From drift-diffusion recombination modeling (see next section) we find that $\eta_{\text{rec}} = 1$. We assume $\eta_{\text{S}} = 0.25$, the quantum-statistical value. For emission from the α -NPD and BAQ layers the product $\eta_{\text{rad}}\eta_{\text{out}}$ is calculated in a manner already discussed in section 5.3.1. The calculation is somewhat simplified by assuming that α -NPD and BAQ emission originates from a single dipole at 10 and 20 nm from the interface, respectively, instead of from the entire distribution. Moreover, for BAQ thickness values in the range 100 to 140 nm all emission is assumed to originate from the α -NPD layer, for BAQ thicknesses in the range 160 to 210 nm all emission is assumed to be generated by CT states located at the interface, while for the 240 and 300 nm case the detailed contributions as shown in figure

5.6 are assumed. The triangles and squares refer to calculations where the radiative decay probability of CT states ($\eta_{\text{rad,CT}}$) is assumed to be equal to 0.1 or 0.3, respectively.

The figure shows that the calculated and measured EQE values fall in the same range (0.5 to 1.5%), but that the detailed BALq thickness dependence is different. For $\eta_{\text{rad,CT}} = 0.1$, the calculated EQE values clearly underestimate the measured EQE in the range 160-210 nm, dominated by CT emission. As already mentioned, a small change of $\eta_{\text{rad,CT}}$ would have a minor effect on the reconstructed profiles but a large effect on the EQE. If $\eta_{\text{rad,CT}} = 0.3$ is assumed, the calculated EQE curve better reproduces the BALq thickness dependence observed in the measured curve, but the absolute values are larger. The discrepancy would then indicate that either η_{S} is smaller than 0.25 or that there is an additional quenching mechanism not taken into account so far.

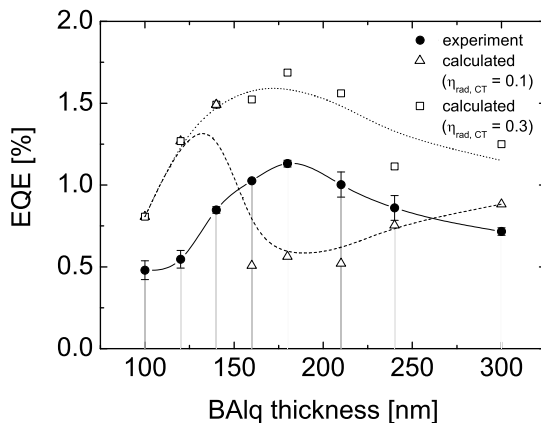


Figure 5.7: Measured BALq layer thickness dependence of the external quantum efficiency (full circles, with error bars as derived from measurements for four nominally identical devices), and of the external quantum efficiency as calculated using the measured shape of the emission profile and a CT state PLQE ($\eta_{\text{rad,CT}}$) equal to 0.1 (empty triangles) or 0.3 (empty squares). The details of the calculation are discussed in the main text.

5.4 Comparison with results from a charge recombination model

From the BALq layer thickness dependence of the reconstructed light-emission profiles and the EQE, presented in the previous section, the following picture on the exciton formation and light generation processes emerges. The observation of emission from the α -NPD and BALq layers indicates that the hole and electron

energy barriers at the interface do not completely block electron and hole transport across the interface. A certain fraction of the carriers can pass the interface, and give rise to exciton formation at a small distance from the interface, of the order of 10 to 20 nm and depending on the BALq layer thickness. Those excitons which diffuse towards the interface before decaying radiatively are with a high probability converted in CT states which only with a small probability give rise to emission. The bulk exciton emission from the region very close to the interface is therefore expected to be small. On the other hand, for excitons diffusing away from the interface such quenching processes are less probable. As a result, the bulk exciton emission is expected to be somewhat detached from the interface, as is indeed observed. In figure 5.8, a schematic picture of the resulting exciton generation and light-emission profiles is given for three α -NPD/BALq layer thickness combinations. In all cases, the majority of the excitons is generated close to the interface. For relatively thin BALq layers (fig. 5.8(a)), the recombination profile is slightly asymmetric towards the α -NPD side, due to electron transport across the interface. For thick BALq layers (fig. 5.8(c)), the transport of holes from the α -NPD side into the BALq side leads to an asymmetric tail in the BALq layer. In the intermediate case (fig. 5.8(b)) the device is most balanced, leading to a symmetric exciton formation profile. Excitons which diffuse to the interface are trapped at the interface as CT states, so that the light-emission profile is expected to be as sketched as in figures 5.8(d-f).

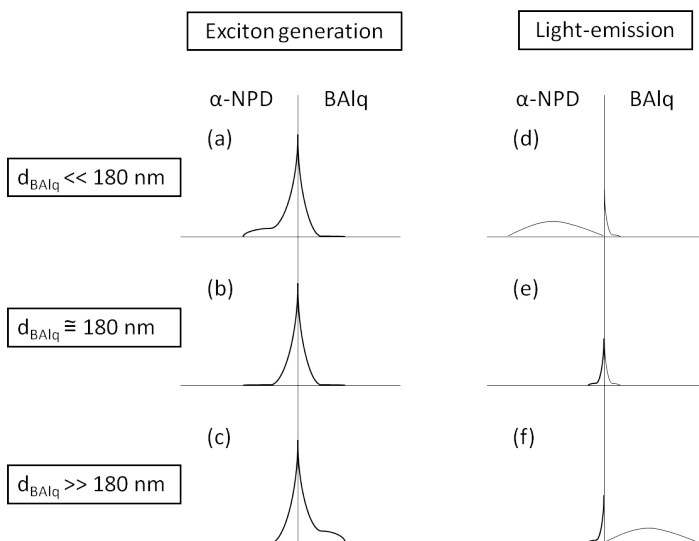


Figure 5.8: Schematic image sketching the different recombination profiles (a-c) and consequent light-emission profiles (d-f) (after exciton-exciton quenching and exciton diffusion) for three different scenarios: BALq layer thickness, d_{BALq} , smaller, equal or larger than 180 nm.

In order to investigate whether the BALq layer thickness dependent exciton generation scenario sketched above could be realistic, we have calculated the shape of the exciton generation profile using a drift-diffusion-recombination model which takes the energetically disordered nature of HOMO and LUMO states in both materials into account. From studies of the hole mobility in α -NPD²⁹ and the electron mobility in BALq¹⁷ it is known that in both cases the charge-density, field and temperature dependent mobility is well described using the Extended Correlated Disorder Model (ECDM).³⁰ Within this model a Gaussian density of states is assumed and the energy levels on nearby molecules are assumed to be spatially correlated. The correlated energy level landscape is obtained by assuming that the energetic disorder results from randomly oriented molecular dipole moments. We note that the physical origin of the spatial correlation is still a subject of debate and that correlated disorder could also arise from the electrostatic field due to the molecular quadrupole moments or from a certain degree of local structural ordering. Within the ECDM, the mobility at a certain temperature is fully described by the mobility in the zero field and zero carrier density limit, μ_0 , the width of the Gaussian density of states, σ , and the volume density of hopping sites, N_t .

We focus on the possible effects of a systematic variation of the BALq layer thickness and consider a simplified bilayer system within which all transport parameter values are symmetric, as shown in figure 5.9. The values of μ_0 for the majority carrier mobilities in both materials (holes in α -NPD and electrons in BALq, indicated as μ_1 in the figure) are taken equal and close to the experimental results obtained in refs. 29 and 17, viz. $5 \times 10^{-10} \text{ m}^2\text{V}^{-1}\text{s}^{-1}$. The values for the minority carrier μ_0 mobility values (electrons in α -NPD and holes in BALq, indicated as μ_2 in the figure), which are not known from experiment, were taken a factor of five smaller. For electron and hole transport in both layers we take $\sigma = 0.1 \text{ eV}$ and $N_t = 3 \times 10^{27} \text{ m}^{-3}$, values which realistically describe the DOS. From a study of the electron transport in BALq, it has been found that the total DOS is a superposition of a Gaussian DOS and a small exponential trap DOS, described by a parameter N_{trap} characterizing the volume density of trap states, and a parameter T_0 characterizing the width $k_B T_0$ of the trap DOS, where k_B is the Boltzmann constant. The total DOS is then, for energies $E < 0$, given by

$$\rho(E) = \frac{N_t}{\sqrt{2\pi\sigma^2}} \exp\left(-\frac{E^2}{2\sigma^2}\right) + \frac{N_{\text{trap}}}{k_B T_0} \exp\left(-\frac{E}{k_B T_0}\right). \quad (5.2)$$

We have included the effect of traps for electron transport in BALq, and, in order to keep the devices symmetric, also for hole transport in α -NPD, using $N_{\text{trap}} = 1 \times 10^{25} \text{ m}^{-3}$ and $T_0 = 1200 \text{ K}$. It is important to have a symmetric device in order to investigate the possibility to have exciton generation profiles whose asymmetry is only due to the different thickness values of the α -NPD and BALq layers. Equal 0.3 eV electron and hole injection barriers (Φ , defined as the distance between the top of the Gaussian DOS and the electrode Fermi level) were used. For the case of electron transport this is consistent with the injection barrier obtained for the interface between BALq and the n -doped injection layer in ref. 17, with a -2.9 eV LUMO energy for BALq and a value of -3.2 eV for the

Fermi level energy in the n -doped layer. For the case of hole transport this is consistent with the value for the -5.4 eV HOMO energy for α -NPD and the -5.1 eV Fermi level energy measured for the p -doped layer.³¹ Using these values for the Fermi-level energies in the electrode layers, the built-in voltage was taken equal to 1.9 V. Equal electron and hole energy barriers, Δ , were assumed at the organic-organic interface. The transport across the interface was treated as a dynamic (non-equilibrium) process, in a manner identical to that described within the framework of one-dimensional Master Equation modeling of the transport in a system with a spatially uncorrelated Gaussian DOS.³² The hole and electron current densities across the interface are each a sum of contributions due to forward and backward hops, with hop rates which are calculated in the following way. They are proportional to the hop rates expected in the zero carrier density and zero field limit, multiplied by the ECDM charge density dependent mobility enhancement factor (determined by the carrier concentration at the side of the interface at which the hop starts), and multiplied by exponential factors of the form $\exp[(\pm qaF \mp \Delta)/(2k_B T)]$ for hops parallel or antiparallel to the local field direction, in order to properly take the field-dependence of the hop rate across the interface into account. Here q is the charge of the carrier, F the local electrostatic field and T the temperature. The carrier densities at both sides of the interface are calculated in a self-consistent manner, making use of the condition of a uniform current density. We thus do not impose the more often used boundary condition that the quasi-Fermi level is continuous, as that condition is only valid in equilibrium, at $V = 0$. The diffusion coefficient is obtained from the ECDM mobility functions using the generalized Einstein relation. Recombination is treated as a bimolecular process, described by the Langevin formula. In as far as we know, this is the first application of the ECDM within a multilayer OLED device simulation.

Three calculations were carried out, viz. for BALq layer thicknesses equal to 100, 160 and 300 nm, in all cases with an α -NPD thickness equal to 160 nm, at voltages equal to 6.4, 7.4 and 9.8 V, respectively. For these values the average electrostatic field across the device, $(V - V_{bi})/L$ (with L the total bilayer thickness), is equal in all cases. Initial calculations with values of Δ equal to a few tenths of an eV, which would be consistent with the energy level diagram sketched in figure 5.1, were found to lead to recombination which is confined to a very narrow region, a few nanometers wide, around the interface. A wider recombination zone was obtained when reducing Δ to 0.1 eV. This value was used in the calculations discussed in this chapter, if not otherwise indicated. The calculated current densities are as indicated by filled circles in figure 5.3. The voltages for which these calculations were performed are somewhat smaller than the voltages for which the experiments were carried out. However, we emphasize that it has been our only purpose to investigate trends when increasing the BALq layer thickness, and not to develop an experimentally validated device model. Nevertheless, it may be seen that for the three cases considered the calculated and experimental current densities are quite close. The calculated electron-hole recombination profiles for the three thickness combinations are presented in figure 5.10. The electron-hole recombination efficiency is found to be in all cases close to 100%.

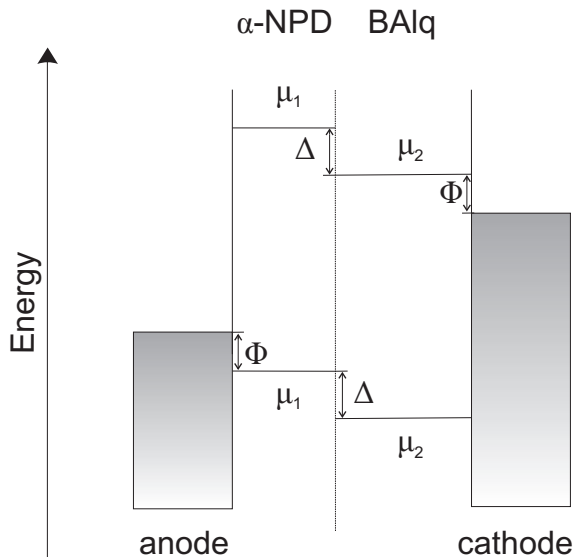


Figure 5.9: Schematic representation of the energy landscape describing the α -NPD/BAlq interface. The main parameters involved in the charge transport and recombination model are here indicated: the energy barrier Δ at the organic-organic interface, assumed to be equal for holes and electrons, the energy barrier Φ at the electrode-organic interface, assumed to be equal for holes and electrons, and the mobility of the majority and minority carriers in the limit of zero field and zero carrier density, μ_1 and μ_2 , respectively.

For each system considered, the calculated recombination profile is found to be peaked at the interface. For the 100 nm-BAlq case (figure 5.10(a)) a recombination plateau is observed on the α -NPD-side of the interface. For the completely symmetric case with equal α -NPD and BAlq thickness (figure 5.10(b)) two equally extended plateaus are predicted on the α -NPD and the BAlq side of the interface. For the 300 nm BAlq case a plateau is located only on the BAlq side (figure 5.10(c)). For relatively thin BAlq layers the electrons can thus reach and subsequently cross the interface and form excitons in the α -NPD layer, while when the BAlq layer is thicker than the α -NPD layer the opposite effect occurs: a non-negligible amount of electrons cannot reach the interface from the cathode, while a certain fraction of the holes can cross the interface and form excitons in the BAlq layer. Qualitatively, the picture on the BAlq layer thickness dependence of the exciton generation profile as obtained from the calculations is thus in good agreement with the simplified picture sketched in figure 5.8.

In order to investigate the sensitivity of the results to the parameter values chosen, we have carried out various additional calculations for the 100 nm-BAlq case. Table 5.1 summarizes the results obtained in each case. The first row corresponds to the profile plot shown in figure 5.10(a). Subsequently, the applied voltage is increased to 8.5 V (second row), in order to get closer to the value used

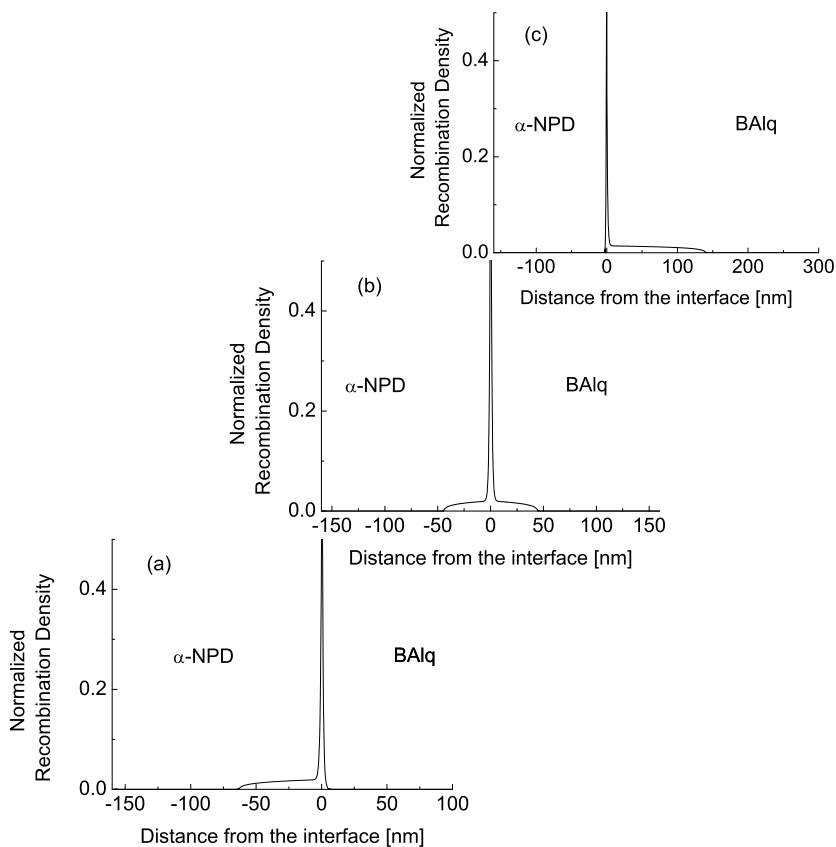


Figure 5.10: Calculated electron-hole recombination profiles, as discussed in the main text. The profiles are normalized on the peak and are presented as a function of the distance from the interface: the α -NPD layer is located on the left of the interface, while the BALq layer is on the right. Three possible layer thickness values are considered for BALq: 100 nm (a), 160 nm (b) and 300 nm (c). In all cases the α -NPD layer thickness is 160 nm.

in the electroluminescence experiments. The calculated current density, 36 A/m^2 , is indeed very close to the experimental value (see figure 5.3). The width of the recombination plateau on the α -NPD side of the interface, $w_{\alpha\text{-NPD}}$, is comparable to that calculated at 6.4 V, but at the BALq side of the interface an additional 16 nm wide recombination plateau is now present. We furthermore find that the width of the recombination plateau at the α -NPD side increases with increasing N_{trap} (not shown) and when increasing the ratio μ_2/μ_1 . For $\mu_2 = \mu_1$ at 6.4 V, the case shown in the third row of table 5.1, the plateau widths at the α -NPD and BALq sides are approximately 96 and 32 nm, respectively. The ratio R between

the exciton formation rate integrated over a ± 5 nm region around the interface and the total exciton formation rate is in this case 0.26, i.e. most of the charges recombine not at the interface, opposite to the previous two cases. These results are very sensitive to the barrier Δ , as shown by the fourth row in the table. When Δ is increased to 0.3 eV, recombination happens exclusively at the interface.

The possibility of having electrons and holes which cross the α -NPD/BAlq interface was already mentioned by Mori *et al.*¹² as an explanation for the observed experimental change in the emission spectra with varying BAlq layer thickness. Interestingly, our calculations suggest that such an effect is only expected if the energy barrier (assumed to be equal for electrons and holes) is significantly smaller than the value of approximately 0.4 eV which would follow from the bulk HOMO and LUMO levels of the molecules, shown in figure 5.1. A possible cause for a reduced energy barrier would be the growth of one of the layers with a net perpendicular orientation of the molecular dipole moment. For thin layers of Alq₃, experimental evidence of such an effect was obtained by Ishii *et al.* from a Kelvin probe study.³³

By combining light-emission profile measurements and charge-transport and recombination models we could thus deduce crucial information about organic-organic interface physics, such as an indication that the energetic barrier is smaller than as expected from the bulk HOMO/LUMO levels of the separate layers.

5.5 Conclusions

The exciton formation and light emission near organic-organic interfaces in OLEDs has been for the first time investigated by reconstructing the light-emission profile across the interface between α -NPD and BAlq in a double-emitting layer device. For that purpose a light-emission profile reconstruction method recently applied to single-layer OLEDs¹⁵ was extended to bilayer devices. The light emission was found to shift from the α -NPD side to the BAlq side of the interface as the BAlq

Table 5.1: Overview of the calculated recombination profiles for a 100 nm-thick BAlq layer device, in terms of the plateau width in the α -NPD layer, $w_{\alpha\text{-NPD}}$, the plateau width in the BAlq layer, w_{BAlq} and the ratio R between the total exciton formation rate in a ± 5 nm region around the interface and the total exciton formation rate. The calculations were performed as a function of the energy barrier at the organic-organic interface, Δ (equal for both electrons and holes), the ratio between minority and majority carrier mobility, at zero carrier density and field, μ_2/μ_1 , and the voltage, V .

Δ [eV]	μ_2/μ_1	Voltage [V]	$w_{\alpha\text{-NPD}}$ [nm]	w_{BAlq} [nm]	R
0.1	0.2	6.4	65	6	0.63
0.1	0.2	8.5	65	16	0.61
0.1	1	6.4	96	32	0.26
0.3	1	8.5	0	0	1

thickness was varied from 100 to 300 nm, while the α -NPD thickness was fixed to 160 nm. A corresponding variation in the emission color point and EQE was also measured and compared to calculated predictions. From the observed emission color point changes, strong evidence was found of charge-transfer (CT) state generation, confirmed by the results of time-resolved photoluminescence measurements on molecularly mixed layers.

Qualitatively, the observed emission profile shift across the interface could be explained well using a state-of-the-art charge-transport and recombination model. However, the calculations suggest that the actual HOMO and LUMO energy barrier at the interface is significantly smaller (~ 0.1 eV) than the approximately 0.4 eV barriers which would be expected from the bulk HOMO and LUMO energies of the two layers. It follows that quantitatively predictive device modeling of multilayer OLEDs, such as used for white lighting or display applications, is only possible if such deviations are taken into account. For that purpose, dedicated studies should be carried out of the effect of deposition conditions on the formation of a net perpendicular dipole moment of the constituent layers.

5.6 Appendix A

Complex refractive index

Figure 5.11 shows the measured complex refractive index dispersion curves for α -NPD and BA1q. As discussed in the text, in both cases the curves are the result of an analysis of ellipsometry data obtained for three organic layers evaporated on quartz, with organic layer thicknesses equal to 80, 100, and 120 nm.

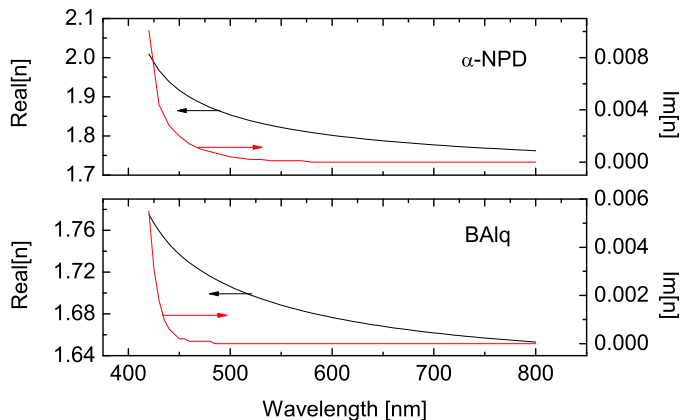


Figure 5.11: Complex refractive index, n , curves as measured by ellipsometry on α -NPD (top) and BA1q (bottom) layers evaporated on quartz.

5.7 Appendix B

Analysis method

The shape of the emission profile is obtained in the following way using a least-mean-squares fitting method. As a first step, the experimental s and p polarized emission intensities $I_{s(p)}^{\text{expt}}(\lambda, \theta)$, measured at M values of the wavelength λ and N values of the emission angle θ , are normalized using the expression

$$I_{\text{norm},s(p)}^{\text{expt}}(\lambda, \theta) = \frac{I_{s(p)}^{\text{expt}}(\lambda, \theta)}{S_{s(p)}^{\text{expt}}(\lambda)}, \quad (5.3)$$

with

$$S_{s(p)}^{\text{expt}}(\lambda) \equiv \frac{1}{N} \sum_{j=1}^N I_{s(p)}^{\text{expt}}(\lambda, \theta_j) \quad (5.4)$$

angle-averaged experimental spectral intensities. As a second step, trial spectral intensities are calculated in the following way. A (fixed) normalized source spectrum, $S_k^{\text{source}}(\lambda)$, and a trial emission profile $P_k(\delta)$, and a trial dipole orientation θ_d are assumed. In the presence of k emitting layers, the emission profile is normalized in the following manner:

$$w_k = \int_k P_k(\delta) d\delta \quad (5.5)$$

is the relative contribution to each layer, so that

$$\sum_{k=1}^{k_{\text{max}}} w_k = 1 \quad (5.6)$$

The trial calculated intensity is then:

$$I_{s(p)}^{\text{calc,trial}}(\lambda, \theta) = \sum_{k=1}^{k_{\text{max}}} \int_k P_k(\delta) S_k^{\text{source}}(\lambda) I_{s(p)}^{\text{calc}}(\lambda, \theta, \delta, \theta_d) d\delta. \quad (5.7)$$

The intensity includes all effects, i.e. also the reduction due to the finite value of η_{rad} in one or more layers, and it includes the local η_{rad} enhancement due to microcavity effects. Subsequently, the trial intensity is normalized:

$$I_{\text{norm},s(p)}^{\text{calc,trial}}(\lambda, \theta) = \frac{I_{s(p)}^{\text{calc,trial}}(\lambda, \theta)}{\frac{1}{N} \sum_{j=1}^N I_{s(p)}^{\text{calc,trial}}(\lambda, \theta_j)}, \quad (5.8)$$

Finally, the optimal emission profile and dipole orientation are found by iteratively minimizing the quantity

$$\chi^2 \equiv \sum_{i=1}^M \sum_{j=1}^N \sum_{s,p} \{I_{\text{norm},s(p)}^{\text{calc,trial}}(\lambda_i, \theta_j) - I_{\text{norm},s(p)}^{\text{expt}}(\lambda_i, \theta_j)\}^2. \quad (5.9)$$

5.8 References

1. *Nat. Photon. Technology Focus* **3**, 8 (2009).
2. S. Reineke, F. Lindner, G. Schwartz, N. Seidler, K. Walzer, B. Lüssem and K. Leo, *Nature* **459**, 234 (2009).
3. J. F. Wang, Y. Kawabe, S. E. Shaheen, M. M. E. Morrell, G. Jabbour, P. A Lee, J. Anderson, N. R. Armstrong, B. Kippelen, E. A. Mash, N. Peyghambarian, *Adv. Mater.* **10**, 230 (1998).
4. T. Noda, H. Ogawa, Y. Shirota *Adv. Mater.* **11**, 283 (1999).
5. M. Cocchi, D. Virgili, G. Giro, V. Fattori, P. Di Marco, J. Kalinowski, Y. Shirota *Appl. Phys. Lett.* **80**, 2401 (2002).
6. Y. Iwama, T. Itoh, T. Mori and T. Mizutani, *Thin Sol. Films* **499**, 364 (2006).
7. T. Itoh, T. Mizutani and T. Mori, *Colloids and Surfaces A: Physicochem. Eng. Aspects* **284-285**, 594 (2006).
8. K. Itano, H. Ogawa and Y. Shirota *Appl. Phys. Lett.* **72**, 636 (1998).
9. W. M. Su, W. L. Li, Q. Xin, Z. S. Su, B. Chu, D. F. Bi, H. He and J. H. Niu *Appl. Phys. Lett.* **91**, 043508 (2007).
10. M. Castellani and D. Berner, *J. Appl. Phys.* **102**, 024509 (2007).
11. N. Matsumoto, M. Nishiyama and C. Adachi, *J. Phys. Chem. C* **112**, 7735 (2008).
12. T. Mori and T. Itoh, *J. Photopolym. Sc. Tech.* **22**, 515 (2009).
13. N. Matsumoto and C. Adachi, *J. Phys. Chem. C* **114**, 4652 (2010).
14. A. Köhler and H. Bässler, *Materials Science and Engineering R* **66**, 71 (2009).
15. S. L. M. van Mensfoort, M. Carvelli, M. Megens, H. Greiner, D. Wehenkel, M. Bartyzel, R. A. J. Janssen and R. Coehoorn, *Nat. Photon.* **4**, 329-335 (2010).
16. M. Carvelli, R. A. J. Janssen and R. Coehoorn, *J. Appl. Phys.*, accepted (2011).
17. S. L. M. van Mensfoort, R. J. de Vries, V. Shabro, H. P. Loebel, R. A. J. Janssen and R. Coehoorn *Org. Electron.* (11), 1408 (2010).
18. M. Brinkmann, G. Gadret, M. Muccini, C. Taliani, N. Maciocchi and A. Sironi, *J. Am. Chem. Soc.* **122**, 5147 (2000).
19. B. Ruhstaller, S. A. Carter, S. Barth, H. Riel, W. Riess and J. C. Scott, *J. Appl. Phys.* **89**, 4575 (2001).
20. T.-Y. Chu, Y.-S. Wu, J.-F. Chen and C. H. Chen, *Chem. Phys. Lett.* **404**, 121 (2005).
21. R. Meerheim, M. Furno, S. Hofmann, B. Lüssem and K. Leo, *Appl. Phys. Lett.* **97**, 253305 (2010).
22. Y.-J. Cheng, M. S. Liu, Y. Zhang, Y. Niu, F. Huang, J.-W. Ka, H.-L. Yip, Y. Tian and A. K.-Y. Jen, *Chem. Mater.* **20**, 413 (2008).

23. A. Wan, J. Hwang, F. Amy and A. Kahn, *Org. Electr.* **6**, 47 (2005).
24. J.-W Kang, D.-S Lee, H.-D Park, J. W. M. Kim, W.I Jeong, Y.-S Park, S.-H. Lee, K. Gob, J.-S Lee and J.-J Kim= J. Hwang, F. Amy and A. Kahn, *Org. Electr.* **9**, 452 (2008).
25. *Commission internationale de l'Eclairage proceedings, 1931*, Cambridge University Press, Cambridge (1932).
26. H. Greiner and O. J. F. Martin, *Proc. of SPIE* **5214**, 249 (2004).
27. K. J. Neyts, *Opt. Soc. Am. A* **15**, 962 (1998).
28. Y. Kawamura, H. Sasabe and C. Adachi, *Jap. J. Appl. Phys.* **43**, 7729 (2004).
29. S. L. M. van Mensfoort, V. Shabro, R. J. de Vries, R. A. J. Janssen and R. Coehoorn *J. Appl. Phys.* (107), 113710 (2010).
30. M. Bouhassoune, S. L. M. van Mensfoort, P. A. Bobbert and R. Coehoorn, *Org. Electron.* (10), 437 (2009).
31. G. Schwartz, K. Walzer, M. Pfeiffer and K. Leo, *Proc. of SPIE*, Vol.6192, 61920Q (2006).
32. R. Coehoorn and S. L. M. van Mensfoort, *Phys. Rev. B* (80), 085302 (2009).
33. H. Ishii, N. Hayashi, E. Ito, Y. Washizu, K. Sugi, Y. Kimura, M. Niwano, O. Ouchi and K. Seki. *Physics of Organic Semiconductors, chapter 3*, Ed. W. Brütting, Wiley-VCH (2005).

6

Light-emission profile reconstruction for white-light emitting multilayer OLEDs

In the previous chapter we applied the light-emission profile reconstruction method to a double-emitting layer OLED, containing rather thick ($\sim 100 - 300$ nm) emitting layers. When varying the thickness of one of the layers, an emission profile shift across the interface was measured. In this chapter, we reconstruct for the first time the emission profile in hybrid white-light emitting OLEDs, where the total thickness of the emitting region is less than 50 nm. This region is composed of blue, green and red emitting layers and an exciton blocking layer. It is shown how a reconstruction of the emission profile, in combination with the analysis of the emission color point and external quantum efficiency, can elucidate the functioning of the device and in particular can clarify the role of the exciton blocking interlayer.

6.1 Introduction

In the Introduction of this thesis an overview of the most successful approaches to the fabrication of white-light emitting OLEDs has been presented. In this chapter we will analyze the emission profile of white-light emitting devices investigated within the European 7th framework Project AEVIOM¹ (Advanced Experimentally Validated Integrated OLED Modelling, 2008-2011). The aim of the project was the development of a predictive model to describe the charge transport and recombination physics of a white-emitting OLED stack. We will present here the

application of the light-emission profile reconstruction method presented in chapter 2 to white multilayer OLEDs, and discuss the information derived about the photophysics of the layer stack. The devices were fabricated at the Institut für Angewandte Photophysik, Technische Universität Dresden (Germany). The layer stack is sketched in figure 6.1.

Aluminum	100 nm
NET5:NDN1	40 nm
NET5	10 nm
Spiro-DPVBi	10 nm
TCTA:TPBi	3-5 nm
TCTA:Ir(ppy) ₃	3-5 nm
α-NPD:Ir(MDQ) ₂ acac	20 nm
α-NPD	10 nm
NHT5:NDP2	40 nm
ITO	90 nm
Glass	1.5 mm

Figure 6.1: Schematic representation of the OLED stack investigated within the European 7th framework Project AEVIOM.¹

Electrons are injected from the aluminum cathode into the blue emitting fluorescent layer 2,2',7,7'-tetrakis(2,2-diphenylvinyl)spiro-9,9'-bifluorene, Spiro-DPVBi, via the sequence of an *n*-doped electron injection layer NET5-4%NDN1² and an electron-transporting and hole-blocking layer NET5.² Holes are injected from the indium tin oxide, ITO, anode into the red emitting phosphorescent α-NPD:5mol% Ir(MDQ)₂(acac) containing an N,N'-di(naphthalen-1-yl)-N,N'-diphenyl-benzidine (α-NPD) host matrix and an (acetylacetonate)bis(2-methyldibenzo [f,h]quinoxinalate) iridium (Ir(MDQ)₂(acac)) guest, via the *p*-doped hole injection NHT5: 4mol% NDP2 layer² and α-NPD layer. A green emitting TCTA:8mol% Ir(ppy)₃ layer with a 4,4',4''-tris(N-carbazoyl)-triphenylamine (TCTA) host and a fac-tris(2-phenylpyridyl) iridium (Ir(ppy)₃) guest and exciton-blocking TCTA:33mol% TPBi (1,3,5-tris(N-phenylbenzimidazol-2-yl)benzene) interlayer complete the layer stack.

The layer stack is an example of a “hybrid” fluorescent-phosphorescent OLED. The concept of a hybrid OLED was already presented in chapter 1. The device studied in this chapter is similar to the one analyzed by Schwartz and co-workers in ref. 3. In the following discussion about the functioning principle of the OLED it will be useful to refer to figure 6.2, where the HOMO and LUMO energy levels of the central emitting layers and exciton blocking layers (a), together with the singlet and triplet energy levels for the emitting layers (b) are shown. The energy values presented have been retrieved from the recent literature.³⁻⁶

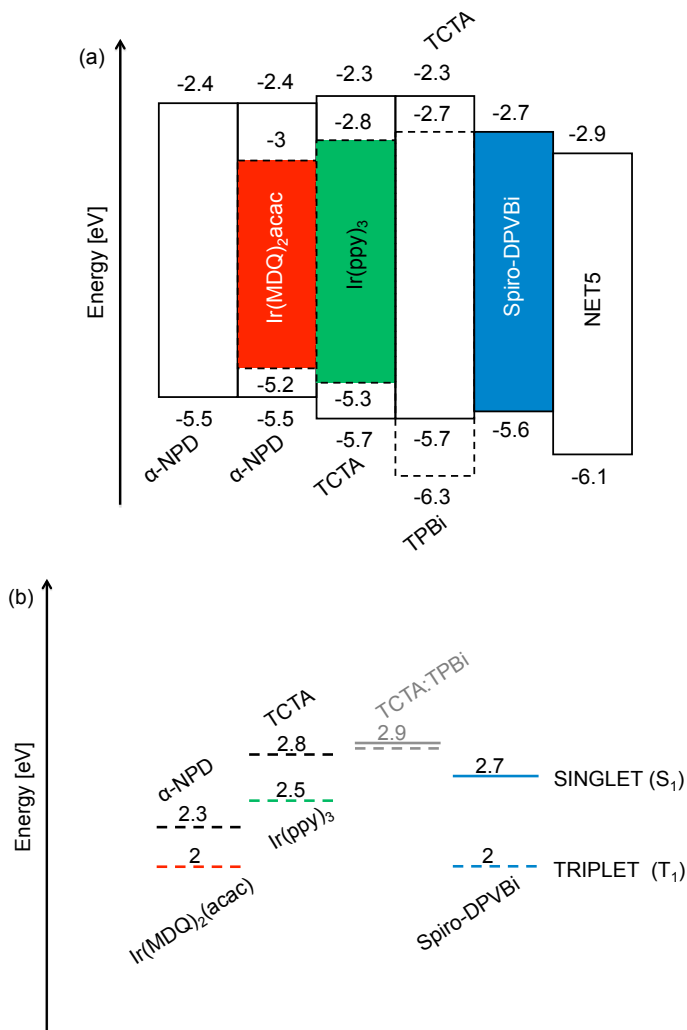


Figure 6.2: Energy diagram of the HOMO and LUMO levels of the emitting and excitons blocking layers (a), and corresponding singlet (solid line) and triplet (dashed line) exciton energy levels (b). In the absence of information from the literature about charge-transfer state singlet and triplet energy levels in TCTA:33mol%TPBi, the values indicated are deduced from the HOMO and LUMO levels in TCTA and TPBi as described in the main text.

At the start of our study, a tentative view on the functioning of these devices, yet to be supported by additional experiments, was the following. Electrons and holes are injected and transported with minor energy loss to the region surrounding the ambipolar TCTA:TPBi interlayer. Here they meet and generate excitons at both the Spiro-DPVBi-side and the TCTA:Ir(ppy)₃-side of the interface. The balance between the recombination events at the two sides of the interface will determine the ratio between the blue and green component in the electroluminescence emission spectrum. In order to have exciton generation both in the blue and in the green layer, the interlayer should be an equally good hole and electron conductor, ideally. This is achieved by employing a host-guest system, with a TCTA matrix where holes will supposedly be conducted, and a TPBi guest (33mol%), which should act as an electron transporter. It follows from figure 6.2(a) that the energy level alignment between the Spiro-DPVBi and TPBi LUMO levels is excellent; moreover, the green emitting layer and the interlayer share the same matrix, through which hole conduction takes place. The interlayer is for the following reason inserted between the green and the blue layer. In the absence of an interlayer, singlet excitons generated in the blue layer could diffuse to the blue-green interface and part of them could here be converted into green triplets, as this conversion is favorable (downward) in energy, see figure 6.2(b). This would lead to unwanted loss of the amount of blue singlets contributing to the blue part of the spectrum. Moreover, part of the green triplets diffusing to the interface with the blue layer could be converted into blue triplets: also this step is favorable in energy, as can be observed in figure 6.2(b). Blue triplets are non-emissive, since Spiro-DPVBi is a fluorescent molecule. These excitons would then be lost, thus contributing to a reduction of the total device efficiency. An interlayer characterized by a high singlet and triplet energy level would prevent both singlet exciton diffusion from the blue to the green layer and triplet exciton diffusion from the green to the blue layer. In our case a TCTA:TPBi host-guest system is employed. Since electrons and holes are supposed to be localized on molecules of different type, charge-transfer (CT) states will likely be formed. We have at present no information about the singlet and triplet energy levels for CT states in the specific mixed interlayer analyzed. Schwartz and co-workers found evidence of CT state emission (centered at ~ 465 nm, i.e. ~ 2.7 eV) from the interface between TCTA and TPBi layers.⁷ Considering that CT states are generally characterized by a low binding energy (~ 0.1 eV, see chapter 5) and that the singlet-triplet gap is generally low, due to the low exchange interaction,⁸ from the analysis of the HOMO and LUMO levels of TCTA and TPBi it is safe to assume that the singlet and triplet interlayer CT states energy levels are higher than the singlet and triplet exciton energy levels, respectively, of the adjacent layers. A rough indication is given as grey lines in figure 6.2(b) (singlet and triplet, assumed to be almost degenerate) in case a 0.1 eV binding energy is assumed. The interlayer thickness is quite a critical parameter in the layer stack: it needs to be thick enough to assure a homogeneous coverage of the bottom layer, thus avoiding direct contact between the green and blue layers, but a too large thickness is expected to be detrimental for the electron-hole balance throughout the device. Even a small difference in the hole and electron mobility in the interlayer would in fact

be “blown-up” in case of a large thickness. A similar effect was already observed in chapter 5 where upon increasing the thickness of the electron-transport layer the electron-hole balance was found to be changed. The red component of the emission spectrum is supposed to be due in part to phosphorescent emission from Ir(MDQ)₂(acac) molecules generated by energy transfer from the green phosphorescent excitons after diffusion to the green-red layer interface. A second possible process for exciton generation in Ir(MDQ)₂(acac) is the penetration of electrons from the green layer to the red layer: the electron mobility in the red layer is supposed to be low, so that recombination with holes is expected to be located close to the green layer interface.

In order to investigate the validity of this picture, four OLEDs were analyzed with different thickness combinations of interlayer and green emitting layer: TCTA:Ir(ppy)₃ (3 nm) / TCTA:TPBi (3 nm), TCTA:Ir(ppy)₃ (3 nm) / TCTA:TPBi (5 nm), TCTA:Ir(ppy)₃ (5 nm) / TCTA:TPBi (3 nm), TCTA:Ir(ppy)₃ (5 nm) / TCTA:TPBi (5 nm).

6.2 Emission color point and external quantum efficiency

Although the changes in the microcavity structure of the four OLEDs analyzed are minimal (the interlayer and green layer thicknesses change from 3 to 5 nm only), large differences in emission color point are measured. An integrating sphere set-up is used following a procedure already described in chapter 5. The results are summarized in figure 6.3. External quantum efficiency (EQE) measurements were performed in the same set-up. The results are presented in table 6.1.

Table 6.1: Experimentally measured external quantum efficiency for the different OLED types analyzed.

	TCTA:TPBi (3 nm)	TCTA:TPBi (5 nm)
TCTA:Ir(ppy) ₃ (3 nm)	5 ± 1% (A)	3 ± 1% (B)
TCTA:Ir(ppy) ₃ (5 nm)	4 ± 1% (C)	3 ± 1% (D)

The thinnest layer-thickness combination (device A) shows warm white emission, almost yellowish. By fixing the green layer thickness and increasing the interlayer thickness, i.e. going from device A to device B and from C to D, the color-point shows a blue-shift. A comparable blue-shift was observed by Schwartz and co-workers³ in similar layer-stacks when the interlayer thickness was increased, in that case from 2 to 4 nm. By increasing the green layer thickness, at a fixed interlayer thickness (from A to C and from B to D) a shift to a more greenish color point is observed. A second interesting effect is the influence of the interlayer thickness on the measured external quantum efficiency. Although the spread in the measured EQE value range is quite limited, increasing the interlayer thickness

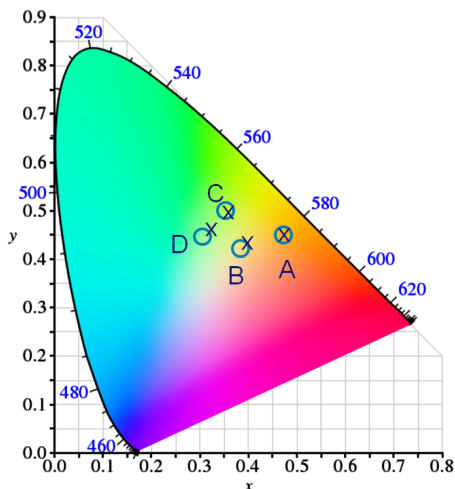


Figure 6.3: Measured (circles) and calculated (crosses) CIE 1931 color coordinates integrated over all angles in air, for the different layer stacks analyzed: (A) TCTA:Ir(ppy)₃ (3 nm) / TCTA:TPBi (3 nm), (B) TCTA:Ir(ppy)₃ (3 nm) / TCTA:TPBi (5 nm), (C) TCTA:Ir(ppy)₃ (5 nm) / TCTA:TPBi (3 nm) and (D) TCTA:Ir(ppy)₃ (5 nm) / TCTA:TPBi (5 nm)

corresponds to a drop of the measured EQE, more significant for the 3 nm-green device.

Both effects cannot be simply explained in terms of a change of the light-outcoupling efficiency due to a modification of the optical microcavity since, as already mentioned, the change in the layer thickness values is almost negligible from an optical point of view. The effects must be related to a change in the charge transport/recombination physics and photophysics of the devices. In order to investigate that, we have reconstructed the light-emission profiles in the different OLEDs.

6.3 Light-emission profile reconstruction

In this chapter, the light-emission reconstruction technique presented in this thesis is for the first time employed to white-light emitting OLEDs with emitting layers which are only a few nanometers thick. Two main changes were applied with respect to the approach already presented in the previous chapters. Since the angular-dependence of the emission from these OLEDs was found to be similar in all four cases, employing a normalization routine such as the one described in the appendix of chapter 2, i.e. over the sum over the angles, would not be very useful. It would lead to similar normalized experimental spectra for all four cases since information would be lost about the main spectral characteristics of the device; this is a consequence of the very small difference of the microcavity properties of

the four layer stacks. In order to better exploit the variation in the main spectral components we chose to normalize the measured and calculated emission spectra on the emission maximum over the entire wavelength and angular range, separately for the two polarizations (see the appendix A of this chapter). The second change concerns the treatment of self-absorption in each of the emitting layers, which is in this case not taken into account, given the small thickness of the layers involved. Absorption in the other emissive layers and in the non-emissive layers is included. The same optical microcavity model as described in the previous chapters is used also in this case. The orientation of the oscillating dipoles is assumed to be random. No assumption is made on the shape of the light-emission profile, i.e. we use a χ^2 minimization approach where the weight of each dipole, located at 1 nm distances, constitutes a degree of freedom, with the only constraint that the dipole weight is non-negative. The method is thus similar to the Tikhonov approach, with $\alpha = 0$, presented in chapter 3. The complex refractive index dispersion curves and photoluminescence spectra (describing the “source spectra” for the red, green and blue excitons) have been measured at Philips Research Aachen or were available in the material library of SETFOS, a commercial software program distributed by Fluxim AG, Switzerland. The radiative decay probability characteristic of the different emitters has been assumed equal to 0.35 for Spiro-DPVBi, after ref. 4, 0.84 for Ir(MDQ)₂(acac) in α -NPD, after ref. 9 (in that paper a 10mol% Ir(MDQ)₂ in α -NPD was analyzed) and 0.76 for Ir(ppy)₃ in TCTA (exactly the same concentration in TCTA as in the stack we analyze), after a similar analysis as in ref. 9, not yet published at the moment this thesis is written and privately communicated by Dr. M. Furno from the Institut für Angewandte Photophysik, Technische Universität Dresden, Germany.

The reconstructed profiles, corresponding to the four layer stack combinations, are presented in figure 6.4. The discretization step is 1 nm and the sum of all contributions is normalized. No emission is assumed at organic-organic interfaces and within the interlayer. The profiles have been reconstructed for a current density of ~ 200 A/m², equal for all devices, corresponding to an applied voltage in the range 3.1-3.6 V, increasing for increasing device thickness. A similar analysis performed at ~ 40 A/m² led to essentially similar profiles, within the resolution limits of the technique (see chapter 3). The sensitivity of the reconstructed profiles to experimental uncertainties within the emission intensity has been analyzed and the results are presented in appendix B. The results hereafter presented are essentially confirmed.

As may be observed, in all cases the main contributions to the light emission are located within the green and the red layer. In the red layer light is generated close to the interface with the green layer. The high concentration of excitons close to the green interface confirms the picture presented in section 7.1: it can be due in part to the energy transfer of green excitons to red excitons and in part to electron penetration in the red layer. A significant change in the reconstructed profiles is observed when the interlayer and green layer thickness values are changed. An enhancement of the green emission and, to a less extent, of the blue emission is observed when the green layer thickness is increased, while the red contribution diminishes. Increasing the interlayer thickness, a significant

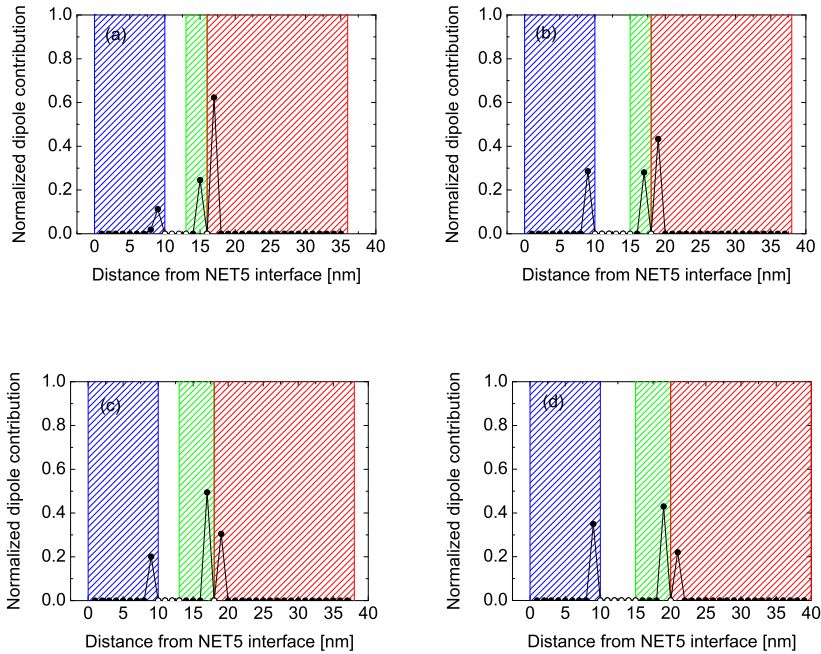


Figure 6.4: Reconstructed light-emission profile for hybrid OLEDs (A-D), defined in section 7.1 with different layer stacks, characterized by: (a) TCTA:Ir(ppy)₃ (3 nm) / TCTA:TPBi (3 nm), (b) TCTA:Ir(ppy)₃ (3 nm) / TCTA:TPBi (5 nm), (c) TCTA:Ir(ppy)₃ (5 nm) / TCTA:TPBi (3 nm) and (d) TCTA:Ir(ppy)₃ (5 nm) / TCTA:TPBi (5 nm). Empty dots indicate positions from where we assumed no dipole contribution.

enhancement of the blue exciton contribution is found, while the green and red components are reduced (the green component for the 3 nm green layer cases is almost not affected). Hereafter we will discuss possible explanations for the observed profile changes. First, the effect of thickness changes on the exciton-generation profile is considered. If by increasing the green layer thickness a larger amount of excitons is generated in the green layer, this would lead to a larger green contribution to the spectrum. Moreover, if the electron transport properties of the interlayer are worse than the hole transport properties, increasing the interlayer thickness would lead to a lower probability of electron penetration into the green and red layer, while the penetration of holes in the blue layer would be unaffected. This would lead to a relative increase of the blue contribution as the interlayer thickness is increased. Nevertheless, preliminary Monte Carlo studies of the exciton-generation profiles in this type of devices¹⁰ suggest that a change of the interlayer and green layer thickness does not lead to such a strong variation of the exciton generation profile as we observed for the light-emission profile. This could indicate that the experimentally observed changes are not due to the combined effects of the charge transport and recombination on the exciton-generation profile. Alternatively, a thickness non-uniformity of the 3 nm green layer, leading to the formation of islands, could explain the higher chance for exciton generation in the red layer as a result of both electron penetration directly in the red layer from the interlayer and energy transfer from charge-transfer states formed in the interlayer. A thicker green layer would lead to a lower chance of direct contact between the interlayer and the red layer, and thus to a higher chance of exciton generation in the green layer. Following a similar rationale, a 3 nm thin interlayer might not block exciton energy transfer from the blue to the green layer as efficiently as a 5 nm layer would do. This would lead to a higher amount of blue excitons in the 5 nm interlayer case.

The reconstructed profiles can be used to predict the color point shift which would be observed in an integrating sphere measurement. For that purpose, we calculate the light emission in air by using the information derived from our analysis of the light emission in glass. In figure 6.3 the predicted color points are presented together with the corresponding measured points. The agreement between predictions and measurement is good, apart from the thickest samples, for which the blue contribution to the calculated spectrum is somewhat too small as compared to the measured one.

We have also used the reconstructed light-emission profiles to obtain a rough estimate of the external quantum efficiency. First the internal exciton generation contributions for the different emitting species are deduced from the determined light-emission contributions shown in figure 6.4. The difference between the two is due to is assumed to be the radiative decay efficiency, the light outcoupling efficiency and the finite blue exciton singlet fraction (assumed to be equal to 25%). Losses due to exciton-exciton and exciton-polaron interaction are neglected, as well as losses due to the possible generation of CT states in the interlayer. The determined internal exciton generation contributions are presented in table 6.2 for the different interlayer and green layer thickness combinations analyzed, indicated as A-D following the definition already given in the previous sections. It may be

noticed that the highest exciton contribution is in all cases the blue one. The small singlet fraction and the finite radiative decay and light-outcoupling efficiency finally lead to light-emission spectra where the red and green components are more dominant.

Table 6.2: Normalized internal exciton generation contributions as deduced from the determined light-emission contributions shown in figure 6.4, for different interlayer and green layer thickness combinations, indicated as A to D following the same definition as given in table 6.1.

	Blue [%]	Green [%]	Red [%]
A	57.9	12.7	29.4
B	78.7	8.8	12.5
C	69.1	19.9	11.0
D	82.9	11.8	5.3

In order to calculate the external quantum efficiency for the different interlayer and green layer thickness combinations, we used the calculated internal exciton generation contributions and proceeded as follows. The electron-hole recombination efficiency is assumed to be close to unity due to the excellent injection properties and the use of electron- and hole-blocking layers. Consistently with the assumptions used to obtain the normalized contributions given in table 6.2, the losses due to exciton-exciton or exciton-polaron interaction are neglected, as well as losses due to the possible generation of CT states in the interlayer, which are probably characterized by a low radiative decay efficiency. The EQE is then limited by the radiative decay efficiency, η_{rad} , of the different emitting species (see section 6.1), by the light-outcoupling efficiency and by the singlet exciton fraction of the blue layer (this is the only fluorescent layer). We investigated the separate influence of these factors on the calculated EQE. The results are given in table 6.3.

The experimentally measured EQE, already presented in table 6.1, is also shown for comparison in the first column. In the second column we give the EQE values as calculated assuming that the radiative recombination efficiency in all emitting layers is equal to 1, and that the blue exciton singlet fraction is also equal to 1. The EQE is in this case only limited by the light-outcoupling efficiency, which is found to be for all cases 19 – 20%. Already by assuming a standard-statistical value for the blue exciton singlet fraction of 25%, the calculated EQE drops by at least 50% and the spread in the EQE values for the different interlayer and green-layer thickness combinations increases, as shown in the third column. If the realistic radiative decay probability values as presented in section 6.1 are used ($\eta_{\text{rad}} = \text{real}$), the calculated EQE varies in the range $\sim 9 - 12\%$, as shown in the fourth column. The calculated product $\eta_{\text{rad}} \cdot \eta_{\text{out}}$ is $\sim 8\%$ for the blue component, $\sim 17\%$ for the green component and $\sim 19\%$ for the red component, substantially equal for all devices. The fifth column presents the most complete EQE calculation in which both realistic values for the radiative decay probability of the different emitting species are used, and the standard-statistical value (25%)

Table 6.3: Experimentally measured and calculated external quantum efficiency for the different OLED types analyzed (indicated by the letters A to D, see table 6.1). The influence of the radiative decay efficiency, η_{rad} , and blue singlet exciton fraction, η_{S} , on the calculated EQE is presented by assuming different combinations of the values for the two parameters η_{rad} and η_{S} , as indicated in the table. In the case of $\eta_{\text{rad}} = \text{real}$, the radiative decay probability for the different materials as published in the literature and given in the main text are used. In the case of $\eta_{\text{rad}} = 1$ the radiative decay probability is assumed to be unitary for all emitting materials.

	$\eta_{\text{EQE,meas}}$ [%]	$\eta_{\text{EQE,calc}}$ [%] $\eta_{\text{rad}} = 1$ $\eta_{\text{S,blue}} = 1$	$\eta_{\text{EQE,calc}}$ [%] $\eta_{\text{rad}} = 1$ $\eta_{\text{S,blue}} = 0.25$	$\eta_{\text{EQE,calc}}$ [%] $\eta_{\text{rad}} = \text{real}$ $\eta_{\text{S,blue}} = 1$	$\eta_{\text{EQE,calc}}$ [%] $\eta_{\text{rad}} = \text{real}$ $\eta_{\text{S,blue}} = 0.25$
A	5 ± 1	19.8	11.7	12.4	8.9
B	3 ± 1	19.3	8.4	10.3	5.6
C	4 ± 1	19.4	9.8	11.1	6.9
D	3 ± 1	19.0	7.5	9.7	4.7

is assumed for the blue exciton singlet fraction. In table 6.4 the separate color contributions to the EQE for this last case are presented.

Table 6.4: Calculated contribution to the external quantum efficiency for the different emission colors and for the different OLED types analyzed (indicated by the letters A to D, see table 6.1). The radiative decay probability for the different materials as published in the literature and given in the main text are used. The exciton singlet fraction for the blue emitter is assumed to be equal to 25%.

	Blue [%]	Green [%]	Red [%]	Total EQE [%]
A	1.1	2.2	5.6	8.9
B	1.6	1.6	2.4	5.6
C	1.4	3.4	2.1	6.9
D	1.7	2.0	1.0	4.7

It may be noticed from tables 6.3 that the calculated EQE values are somewhat larger than the experimental values. Several processes could contribute to explain this difference: (i) the presence of CT states in the interlayer, giving rise to a low radiative decay probability (ii) exciton quenching due to exciton-exciton and exciton-polaron interactions, (iii) uncertainties in the values assumed for the radiative decay probability of the different emitting species, (iv) a possible thickness non-uniformity of the interlayer, leading to the formation of islands, which could enhance the probability of green triplet quenching by energy transfer to non-emitting blue triplets (v) uncertainties in the radiative decay probability and the blue exciton singlet fraction. From table 6.4, which gives the calculated contribution to the external quantum efficiency for the different emission colors and for the different OLED types analyzed, it may be seen how the EQE is influenced by these uncertainties.

Although there is a discrepancy in the absolute values, a similar variation of the calculated EQE values as compared to the measured ones is observed, in particular if the interlayer thickness is increased, i.e. from case A to case B and from case C to case D. Such a variation could be attributed to the large contribution of blue excitons for the thick-interlayer cases: only the singlets are emissive and they are characterized by a lower radiative decay probability compared to the green and the red emitters, see section 6.1. Hence, for devices B and D the EQE is expected to be smaller than for devices A and C, in agreement with the experimental results.

6.4 Conclusions

We have applied the light-emission profile extraction method to hybrid white-light emitting OLEDs. Nanometer-scale variations in the profile have been observed for slightly different layer stacks with different exciton blocking layer and green-emitting layer thicknesses. The analysis of the reconstructed profiles, together with the comparison of the predicted and measured color-point and external quantum efficiency variations, allowed us to deduce crucial information about the charge carrier transport and recombination and the photophysics of the OLEDs studied. In particular, indications of CT state generation within the exciton blocking layer have been presented, leading to efficiency losses. Moreover, the observation of strong variation in the light-emission profile provides information about the electron-hole balance in the layer stack (in particular in the interlayer) and the exciton photophysics close to the organic-organic layer interfaces. Coupling the results here presented to advanced Monte Carlo charge transport and recombination models would provide important insight in the physical and photophysical processes which characterize the functioning of multilayer OLEDs.

6.5 Appendix A

The shape of the emission profile is obtained in the following way using a least-mean-squares fitting method, in a manner which is slightly different from the approach used in chapter 5, as motivated in section 6.3. As a first step, the experimental s and p polarized emission intensities $I_{s(p)}^{\text{expt}}(\lambda, \theta)$, measured at M values of the wavelength λ and N values of the emission angle θ , are normalized using the expression

$$I_{\text{norm},s(p)}^{\text{expt}}(\lambda, \theta) = \frac{I_{s(p)}^{\text{expt}}(\lambda, \theta)}{S_{s(p)}^{\text{expt}}(\lambda)}, \quad (6.1)$$

with

$$S_{s(p)}^{\text{expt}}(\lambda) \equiv \max(I_{s(p)}^{\text{expt}}(\lambda, \theta)) \quad (6.2)$$

The maximum $\max(I_{s(p)}^{\text{expt}}(\lambda, \theta))$ is calculated over the entire λ and θ space, separately for s - and p -polarized light.

As a second step, trial intensity functions are calculated. A normalized source spectrum (fixed), $S_k^{\text{source}}(\lambda)$, a trial layer (k) and position (δ , in 1 nm step) dependent emission profile $P_{k,\delta}$, and a trial dipole orientation θ_d are assumed. The emission profile is normalized such that:

$$\sum_{k=1}^{k_{\text{max}}} \sum_{\delta} P_{k,\delta} = 1. \quad (6.3)$$

The trial calculated intensity is then:

$$I_{s(p)}^{\text{calc,trial}}(\lambda, \theta) = \sum_{k=1}^{k_{\text{max}}} \sum_{\delta} P_{k,\delta} S_k^{\text{source}}(\lambda) I_{s(p)}^{\text{calc}}(\lambda, \theta, k, \delta, \theta_d). \quad (6.4)$$

The intensity due to emission from a single dipole at position δ in layer k , $I_{s(p)}^{\text{calc}}(\lambda, \theta, k, \delta, \theta_d)$, includes all effects, i.e. also the reduction due to the finite value of η_{rad} in layer k , and it includes the local η_{rad} enhancement due to microcavity effects. Subsequently, the trial intensity is normalized:

$$I_{\text{norm},s(p)}^{\text{calc,trial}}(\lambda, \theta) = \frac{I_{s(p)}^{\text{calc,trial}}(\lambda, \theta)}{\max(I_{s(p)}^{\text{calc,trial}}(\lambda, \theta))}, \quad (6.5)$$

The maximum $\max(I_{s(p)}^{\text{calc,trial}}(\lambda, \theta))$ is calculated over the entire λ and θ space, separately for s - and p -polarized light. As a final step, the optimal emission profile and dipole orientation are determined by iteratively minimizing the quantity

$$\chi^2 \equiv \sum_{i=1}^M \sum_{j=1}^N \sum_{s,p} \{I_{\text{norm},s(p)}^{\text{calc,trial}}(\lambda_i, \theta_j) - I_{\text{norm},s(p)}^{\text{expt}}(\lambda_i, \theta_j)\}^2. \quad (6.6)$$

6.6 Appendix B

In order to analyze the sensitivity of the reconstructed light-emission profiles to experimental uncertainties in the emission intensities, we followed the same procedure as presented in chapter 3: we added 5% Gaussian noise to the experimental data. This noise value is considered a conservative estimation of the real noise of the set-up, from the discussions in chapter 3. We reconstructed the light-emission profile for 1000 noise configurations: the profiles obtained for each case are presented in figure 6.5.

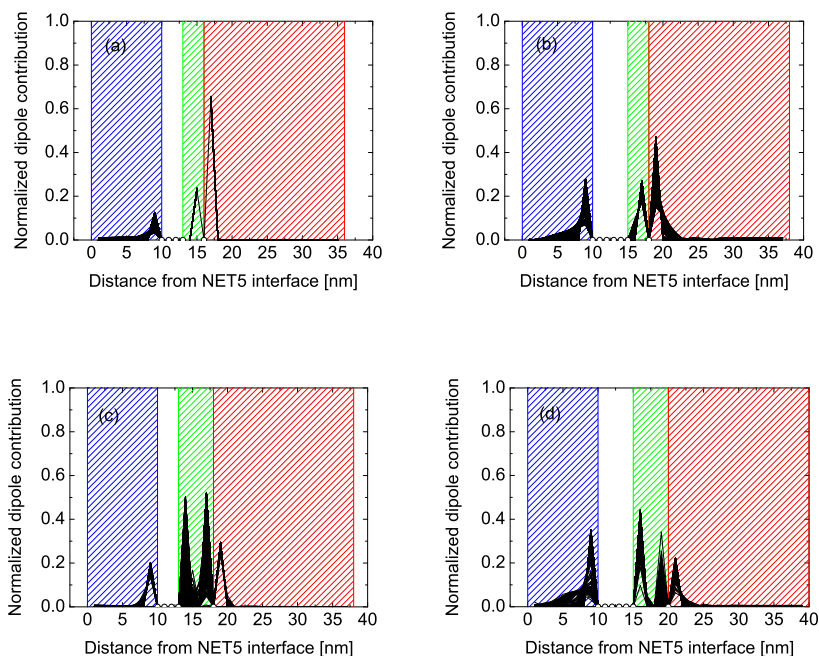


Figure 6.5: Reconstructed light-emission profile for 1000 noise configurations, following the procedure presented in chapter 3; a 5% Gaussian noise level is assumed. Different layer stacks are analyzed: (a) TCTA:Ir(ppy)₃ (3 nm) / TCTA:TPBi (3 nm), (b) TCTA:Ir(ppy)₃ (3 nm) / TCTA:TPBi (5 nm), (c) TCTA:Ir(ppy)₃ (5 nm) / TCTA:TPBi (3 nm) and (d) TCTA:Ir(ppy)₃ (5 nm) / TCTA:TPBi (5 nm). Empty dots indicate positions from where we assumed no dipole contribution.

In all cases, the main profile characteristics and the color contribution balance analyzed in this chapter are confirmed. The effect of the noise is mainly that of broadening the emission region close to the red/green and blue/interlayer interfaces up to ~ 5 nm. Since the profile in the green layer is peaked in some cases close to the red interface and in other cases close to the interlayer, distinguishing the two shapes is beyond the resolution limits.

6.7 References

1. www.aeviom.eu
2. Material supplied by Novaled, AG.
3. G. Schwartz, K. Fehse, M. Pfeiffer, K. Walzer and K. Leo, *Appl. Phys. Lett* **89**, 083509 (2006).
4. G. Li, C. H. Kim, Z. Zhou, J. Shinar, K. Okumoto and Y. Shirota, *Appl. Phys. Lett* **88**, 253505 (2006).
5. G. Schwartz, S. Reineke, T. C. Rosenow, K. Walzer and K. Leo, *Adv. Funct. Mater.* **19**, 1319 (2009).
6. S. Reineke, G. Schwartz, K. Walzer and K. Leo, *Phys. Status Solidi RRL* **3**, 67 (2009).
7. S. Reineke, G. Schwartz, K. Walzer and K. Leo, *Appl. Phys. Lett.* **91**, 123508 (2007).
8. S. Difley, D. Beljonne and T. van Voorhis, *J. Am. Chem. Soc.* **130**, 3420 (2008).
9. R. Meerheim, M. Furno, S. Hofmann, B. Lüssem and Karl Leo, *Appl. Phys. Lett.* **97**, 253305 (2010)
10. M. Mesta and P. A. Bobbert, unpublished

Outlook: implications and future applications

In this Outlook chapter implications of the results of our studies and various possible directions for future applications of the light-emission profile reconstruction method are discussed. First, it will be discussed how measurements of the emission profile may be used to experimentally validate state-of-the-art charge-transport and recombination models. Subsequently we discuss the possible application of our method to other types of optical microcavity devices: light-emitting electrochemical cells (LECs) and organic light-emitting transistors (OLETs). In the final section of this chapter recently reported steps made towards the development of electrically pumped organic lasers with a sandwiched-type layer structure such as that of OLEDs are discussed. Also for this case, suggestions are given about how the application of our method could improve the understanding of the functioning and application potential.

7.1 Introduction

In this thesis we have introduced a method for reconstructing the light-emission profile in OLEDs with nanometer-scale resolution. Three applications of the method have been presented. In single-emitting-layer devices the method was used to measure the exciton singlet fraction; in double-emitting layer devices we could analyze the organic-organic interface photophysics, while in white-emitting multilayer OLEDs we could develop deeper insight in the role of the exciton blocking interlayer and the electron-hole balance throughout the OLEDs.

Hereafter we will discuss possible future applications of our method. In section 7.2 we will describe how the measurement of the emission profile can be used to validate charge transport and recombination models. Subsequently we will focus on the application of our method to other microcavity structures, such as light-emitting electrochemical cells (section 7.3) and organic light-emitting transistors

(section 7.4). A final example will follow in section 7.5, concerning recently reported steps made towards the development of electrically pumped organic lasers with an OLED-like structure. In all cases examples taken from the recent literature are discussed, where the information deduced from a measurement of the light-emission reconstruction profile may have a high impact. Possible foreseen challenges in the application of the method to these types of devices are also analyzed.

7.2 Experimental validation of electron-hole recombination models

In chapter 4 we have presented a comparison between the experimentally reconstructed light-emission profiles for a blue-emitting (PF-7.5%TAA) single layer OLED and the electron-hole recombination profiles, as calculated via a drift-diffusion 1D model. For that purpose, we used the model presented in ref. 1, using the experimentally determined hole and electron mobility functions obtained in refs. 2 and 3, respectively. From the comparison of the profiles (see figure 4.6(b) in chapter 4) we deduced that the calculated profiles are significantly wider than as found experimentally. We considered that as an indication that a more refined model for the recombination process is required, beyond the standard Langevin model employed. Recently, several refinements have been discussed in the literature, including the effect of carrying out the calculation using so-called “bipolar mobilities”⁴ and including the possible effect of mobility anisotropy.⁵ An enhanced recombination rate, resulting from an enhanced lateral mobility, would be expected to give rise to narrower recombination profiles. For the PF-TAA polymers which we studied, the observed presence of a strong in-plane orientation of the emitting dipoles (see chapter 2) is indicative of a strong in-plane orientation of the polymer chains. A strong anisotropy of the electron mobility, which is due to transport via the LUMO states derived from the PF backbone, may therefore be expected. On the other hand, the hole mobility, which is due to hopping in between the TAA units, is not expected to be strongly anisotropic. In order to investigate the effect on the recombination profile, we adapted in chapter 4 the approach for calculating the local recombination rate presented in ref. 1 by including an enhanced contribution from lateral hops of electrons to nearest neighbor sites at which a hole resides. We varied this enhancement factor, considering it as a free parameter, and found that introducing this enhancement gives indeed rise to narrowing of the profile. For 160 nm-thick emitting layer devices, we found that the recombination profiles as calculated and measured at 15 V are quite similar when choosing a mobility anisotropy factor equal to 7 and using a slightly (factor 1.5) enhanced electron mobility in order to fine-tune the peak position (see figure 4.6(c) in chapter 4).

One possible way to investigate the validity of the above mentioned assumptions would be to calculate the electron-hole recombination profile using a 3D Monte Carlo (MC) approach and to compare it to the experimentally reconstructed light-emission profiles using the method we presented throughout this

thesis. This would make it possible to verify the influence of anisotropy, implemented in a MC calculation as a higher hopping rate of charges in the plane parallel to the organic-organic interfaces, thus incorporating the basic physics of the device without the need for a translation to a 1D model. Moreover, it would be automatically possible to verify the possible influence of bipolar mobility on the recombination profile. Concerning this issue, it was predicted by van der Holst and co-workers⁴ that a “reduction in the carrier mobilities in and behind the recombination zone should occur by the increased effective disorder due to the random Coulomb field of the carriers of the opposite sign. This should lead to a further reduction of the calculated width of the recombination zone.” Finally, the effect of charge carrier relaxation would automatically be included, and could then for the first time be studied in a double carrier device. The influence on hole-transport in similar polyfluorene-based devices has recently been shown by Germs and co-workers.⁶ In particular for electrons, relaxation effects are expected to play an important role, due to the high influence of traps on the electron transport. The first 3D MC calculations of the electron-hole recombination profile in blue emitting OLEDs such as those analyzed in chapter 4 were ongoing at the moment this thesis was written.⁷

7.3 Sandwich-type light-emitting electrochemical cells

In its simplest form, sandwich-type light-emitting electrochemical cells (LECs) consist of a single active layer composed of an ionic organo-transition-metal complex, located in between a cathode and an anode (see figure 7.1). The thickness of the active layer is typically a few hundreds of nanometers.

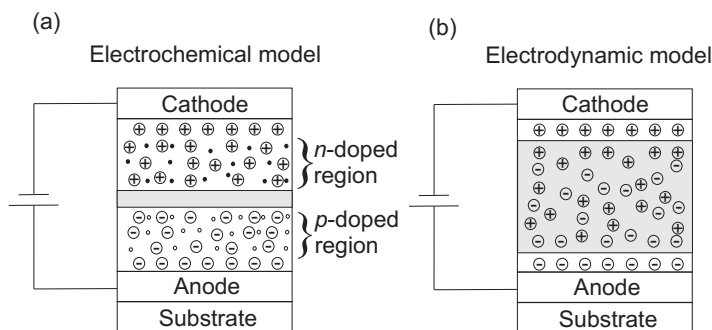


Figure 7.1: Schematic representation of the functioning of light-emitting electrochemical cells according to the electrochemical model (a) or the electrodynamic model (b). ⊕ and ⊖ indicate positive and negative ions, respectively, while empty and full dots indicate holes and electrons, respectively. In grey the light-emission region is indicated.

The main potential advantages of this type of device over OLEDs are the efficient carrier injection due to the presence of ions close to the electrodes, which

reduces possible injection barriers (so that more air-stable electrodes can be used) and the simplified stack, as there is no need for charge injection/charge transport layers.⁸ The most important drawbacks are the long turn-on times and (so far) the low efficiency and the short lifetime. Two models have been developed to describe the functioning of LECs: the electrochemical model⁹ and the electrodynamic model.¹⁰ The electrochemical model (see figure 7.1 (a)) assumes that charge injection is promoted by the doping of the material adjacent to the electrodes, due to the presence of ions, whereas the electrodynamic model (see figure 7.1 (b)) assumes a strong decrease in the injection barrier by the accumulation of ions at the interface. According to the first model light emission occurs within the relatively narrow intrinsic region between the p - and n -doped regions. The electrodynamic model predicts that the entire electric field drops over a thin electrical double layer at the electrode interfaces, and light emission occurs in the much wider intrinsic region which can extend through the entire device. Van Reenen and co-workers¹² have recently demonstrated that the two models are in fact essentially limits of one master model, characterized by different rates of carrier injection. For ohmic nonlimited injection, a p - n junction is formed upon switching on the applied voltage, which is absent in injection-limited devices. The unification is demonstrated by both numerical calculations and measured surface potentials as well as light emission and doping profiles in operational planar devices. The use of planar devices is essential to be able to measure the potential profile through the active layer by means of scanning Kelvin probe techniques. This approach has recently been employed to make a distinction between electrochemical model-like and electrodynamic model-like behavior in planar LECs.¹³ Such a technique is not applicable to sandwiched devices. Lenes and co-workers⁸ have recently proposed an analysis of sandwiched devices using fast current-density and luminance versus voltage scans and impedance spectroscopy, both as a function of operation time. The authors show a transition from an injection-limited regime to a space-charge limited regime in which good and balanced injection occurs. After this transition a further increase in current occurs, which implies a reduction in the thickness of the neutral region due to a continuous growth of the doped layers. An investigation of this type of devices using the light-emission profile reconstruction method presented in this thesis would provide direct evidence for the type of regime (injection limited or space-charge limited) at which the device is operating. In fact, the electrochemical model would result in a rather narrow recombination region located far from the electrodes, within the intrinsic (undoped) region; the electrodynamic model would, on the contrary, predict a very broad light-emission profile, uniformly spread across the emitting layer. It would also be possible to follow the evolution of the profile in time with a nanometer-scale resolution, thus being able to infer the growth of the doping fronts in a sandwiched device. The major difficulty which can be foreseen in applying the profile reconstruction method to LECs is the need for measuring the refractive index and extinction coefficient for the emitting layer as a function of the doping concentration, i.e. over time. One possible strategy to tackle this problem consists in performing spatially-resolved ellipsometry measurements in equivalent planar devices, in order to obtain the optical properties of the doped layers. This challenging approach relies on the

physical equivalence of a planar and a sandwich-type device configuration. In a pioneering study of the comparison between the physics of planar and sandwich-type devices, Leger and co-workers¹⁴ proved in fact that a similar behavior of the doping fronts could be deduced in both configurations. The study of sandwich-type devices proceeded in that case by a somewhat simplified light-emission profile reconstruction approach as compared to the one we propose in this thesis.

7.4 High-efficiency organic light-emitting transistors

Organic field-effect transistors (OFETs) are planar devices, i.e. the charge carriers move in the plane within a single organic layer between a source electrode and a drain electrode, as shown in figure 7.2 (a). In OFETs the charge mobility can be a few orders of magnitude higher than in OLEDs, due to the accumulation of a high density of charges, often enhanced by the higher degree of crystallinity. In balanced ambipolar devices electron-hole pair formation can occur in a narrow region far from the source and drain electrodes. A relatively high light-outcoupling efficiency may be then expected, in view of the relatively large distance to the metallic electrodes. A further improvement as compared to OLEDs, from an the external quantum efficiency point of view, is the possibility to physically separate the exciton generation region from the charge accumulation channels, thus avoiding exciton-charge quenching. This would moreover pave the way to the development of electrically-injected organic lasers, as exciton-charge interaction is considered to be the main obstacle¹⁵ in building-up sufficient population inversion for amplified spontaneous emission to occur. One strategy to obtain spatial separation between charges and excitons has recently been demonstrated by Capelli and co-workers¹⁶ with a trilayer heterostructure Organic Light-Emitting Transistor (OLETs). Excitons are in this case generated within an emitting layer sandwiched in between a hole-conducting and an electron-conducting layer. An EQE of 5% has in fact been demonstrated in this case. This is the highest EQE value published so far for an OLET.¹⁶ The layer structure and energy level diagram characterizing the device are shown in figure 7.2(a) and (b), respectively. The trilayer structure consists of an Alq₃:DCM emitting layer, sandwiched in between an *n*-doped layer (DFH-4T) and a *p*-doped layer (DH-4T). The functioning principle of the device, as sketched by the authors, is as follows. Electrons are preferentially conducted via the DFH-4T layer, while hole transport is predominant in the DH-4T layer. In the recombination zone, holes and electrons are expected to accumulate in the two doped layers. The electric field generated by charge accumulation enables the percolation of charges within the emitting layer where excitons are generated. The spatial separation of the exciton generation region from the charge flow channels (*p*- or *n*-doped layer) would thus enable high external quantum efficiency for this device.

Developing a detailed charge-transport and recombination model for such a device would be essential for understanding the recombination physics and consequently the real potential of the trilayer structure. Since the HOMO levels of

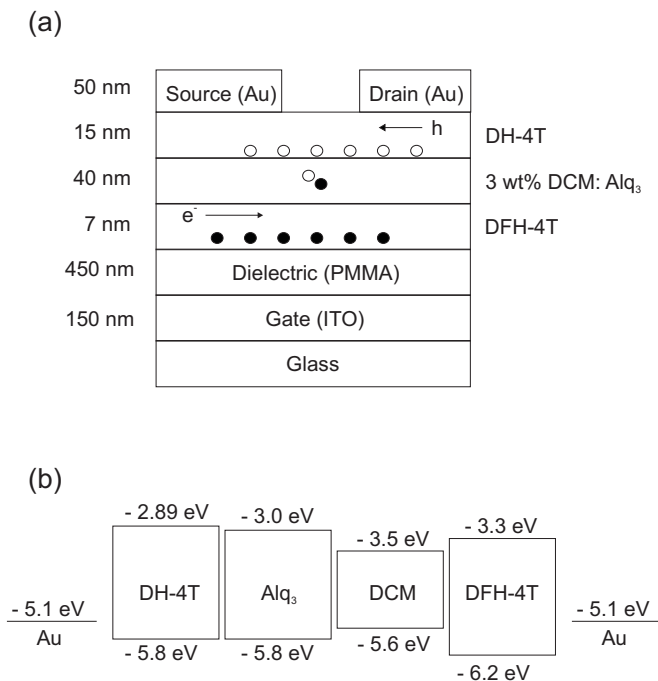


Figure 7.2: Organic light-emitting transistor based on a trilayer heterointerface, as presented by Capelli and co-workers in ref.16. The device structure and energy level diagram of the layer stack are shown in part (a) and (b), respectively.

DH-4T and Alq₃ are very close to each other (see figure 7.2), it is presently not yet clear why holes from the DH-4T layer are not efficiently injected into the DCM:Alq₃ layer, thus leading to hole transport through the DCM:Alq₃ layer, with DCM acting as hole-trapping sites. This type of behavior would result in a broad emission region located close to the drain and to a lower efficiency of the device, due to the interaction between excitons and holes. A first step towards the understanding of the device physics could be a light-emission profile reconstruction analysis. This would reveal whether excitons are uniformly generated throughout the 40-nm-thick emitting layer or whether they prevalently concentrate at one interface, thus providing useful information about the carrier balance and transport, for example as a function of the driving voltage scheme. One may envisage the following issue in applying the light-emission profile reconstruction method to this type of OLETs: the optical microcavity is here determined by the ITO anode (at a quite large distance, ~ 450 nm, from the emitting layer) on one side and air on the other, so one should investigate whether the microcavity effect on the emission from an oscillating dipole is strong enough to still obtain a nanometer-scale resolution on the emission profile.

7.5 Towards electrically-pumped organic organic laser diodes

We conclude this outlook chapter with a note on an interesting fluorescent OLED structure recently presented by Setoguchi *et al.*,¹⁷ whose interesting characteristic is the high current density threshold before external quantum efficiency roll-off occurs, thus proving to be a potential candidate for organic electrically-pumped lasers.¹⁷ In figure 7.3 the energy level diagram of the device is presented. Holes and electrons are injected from the ITO and the aluminum cathode, respectively, into the fluorescent BSB-Cz layer. Doped layers are used for hole and electron injection, with BSB-Cz as a common matrix and with 20wt% MoO₃ and Cs as dopants, respectively.

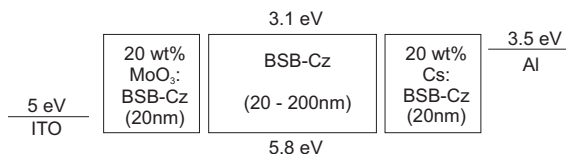


Figure 7.3: Organic Light-Emitting Diodes characterized by a high current density threshold for efficiency roll-off. The device is presented and analyzed in ref.17. The energy level diagram of the layer stack is presented.

The authors identify singlet-polaron annihilation (SPA) as the major cause for the efficiency roll-off of fluorescent OLEDs at high current densities. Assuming that SPA is mainly caused by space charges accumulating at the organic/organic heterointerface, due to the presence of energy barriers, they are able to sensibly increase the roll-off threshold current density by avoiding organic heterointerfaces. This could lead to building-up a high concentration of excitons, which could give rise to amplified spontaneous emission.

The authors measure a value of the current density threshold at which roll-off occurs which increases by about three orders of magnitude, compared to a corresponding OLED with organic heterointerfaces, characterized by the following layer stack: ITO/ MoO₃ (hole-injection layer, 30 nm) / mCP (electron-blocking layer, 10 nm) / BSB-Cz (light-emitting layer, 20 nm) / BCP (hole-blocking layer, 10 nm) / Cs: POPy₂ (electron-injection layer, 30 nm) / aluminum. In order to achieve Amplified Spontaneous Emission (ASE) centered at ~ 470 nm and laser action, an exciton generation rate of $10^{32} \text{ m}^{-3}\text{s}^{-1}$ is needed, as was demonstrated via optical excitation of the same devices. The authors attempt to generate ASE by electrically pumping the device but could not reach the ASE threshold. They estimated the highest exciton generation rate (in units [$\text{m}^{-3}\text{s}^{-1}$]) reachable via electrical excitation as follows:

$$r_{\text{exciton}} = (J/e) \cdot (1/4) \cdot (1/L_{\text{exciton}}), \quad (7.1)$$

where J is the current density, e is the electron charge and L_{exciton} is the exciton generation profile width. The factor $1/4$ is the standard statistical value of the

singlet exciton fraction. For a 200 nm-thick-emitting-layer device, the authors show a linear increase of r_{exciton} until a roll-off current density value threshold of $\sim 10^5$ A/m², corresponding to an exciton generation rate of about 10^{30} m⁻³s⁻¹. For higher current density singlet-polaron annihilation starts to affect even these optimized devices at such a high current regime.

Two approximations affect the exciton generation rate estimation: a standard statistical value for the singlet fraction and the assumption of an exciton generation profile as wide as the whole emitting layer ($L_{\text{exciton}} = 200$ nm). Both approximations could be re-examined exploiting the light-emission profile reconstruction and singlet fraction determination methods we presented within this thesis, in particular in chapters 2 and 4. In general, the exciton generation profile can be significantly narrower than the entire emitting layer, as shown in chapter 2. In particular in case the electron and hole injection into the emitting layer is not affected by energetic barriers, the actual width and shape of the light-emission profile can greatly vary with the detailed e-h mobility balance and with the energetic disorder.¹⁸ This could lead to a higher estimation for the exciton generation rate reachable in the devices proposed by Setoguchi *et al.*; the ASE threshold may thus be closer than previously estimated. It would therefore be of interest to measure the light-emission profile in the proposed devices with high accuracy.

7.6 Conclusions

In this outlook chapter we have shown different possible future applications of the light-emission profile reconstruction method we have presented in this thesis. We have discussed in section 7.2 the possibility to experimentally validate charge transport and recombination models making use of the measured light-emission profiles. In particular, we focused on the possibility to exploit the reconstructed profiles to analyze the importance of mobility anisotropy and charge carrier relaxation. Subsequently we investigated the possible application of the method to other types of optical microcavities: light-emitting electrochemical cells (LECs) and organic light-emitting transistors (OLETs), with a final discussion concerning recently reported steps made towards the development of electrically-pumped organic lasers with an OLED-like structure. In the case of LECs (section 7.3), we presented the possibility to make use of the light-emission profile reconstruction to distinguish between an electrochemical model-like⁹ and an electrodynamic model-like¹⁰ behavior of the cells, an issue of intensive debate in the recent literature. Information about the light-emission profile may moreover help to understand the functioning and application potential of a recently presented high-efficiency OLET structure,¹⁶ as discussed in section 7.4. In section 7.5 the application potential to an interesting fluorescent OLED structure characterized by high efficiency roll-off threshold, presented in ref. 17, is analyzed. The device is a promising option for electrically-pumped organic lasers and the application of both our light-emission profile reconstruction method and our singlet fraction determination method may provide a more accurate estimation of the exciton generation rate threshold needed for ASE, as compared to the value proposed by the authors in ref. 17.

7.7 References

1. R. Coehoorn and S. L. M. van Mensfoort, *Phys. Rev. B* **80**, 085302 (2009).
2. S. L. M. van Mensfoort, S. I. E. Vulto, R. A. J. Janssen and R. Coehoorn, *Phys. Rev. B* **78**, 085208 (2008).
3. S. L. M. van Mensfoort, J. Billen, S. I. E. Vulto, R. A. J. Janssen and R. Coehoorn, *Phys. Rev. B* **80**, 033202 (2009).
4. J. J. M. van der Holst, F. W. A. van Oost, R. Coehoorn and P. A. Bobbert, *Phys. Rev. B* **80**, 235202 (2009).
5. C. Groves and N. C. Greenham, *Phys. Rev. B* **78**, 155205 (2008).
6. W. Chr. Germs, J. J. M. van der Holst, S. L. M. van Mensfoort, P. A. Bobbert and R. Coehoorn, *Phys. Rev. B* **84**, 165210 (2011).
7. H. van Eersel, M. Carvelli, M. Mesta, P. A. Bobbert, R. A. J. Janssen and R. Coehoorn, *unpublished*.
8. M. Lenes, G. Garcia-Belmonte, D. Tordera, A. Pertegás, J. Bisquert and Henk J. Bolink, *Adv. Fun. Mater.* **21**, 15811586 (2011).
9. Q. Pei, G. Yu, C. Zhang, Y. Yang, A. J. Heeger *Science* **269**, 1086 (1995).
10. J. C. deMello, N. Tessler, S. C. Graham, R. H. Friend, *Phys. Rev. B* **57**, 12951 (1998).
11. S. Welter, K. Brunner, J. W. Hofstraat and L. De Cola *Nature* **421**, 54 (2004).
12. S. van Reenen, P. Matyba, A. Dzwilewski, R. A. J. Janssen, L. Edman and M. Kemerink, *J. Am. Chem. Soc.* **132**, 13776 (2010).
13. P. Matyba, K. Maturova, M. Kemerink, N. D. Robinson and L. Edman, *Nat. Mater.* **8**, 672 - 676 (2009).
14. J. M. Leger, S. A. Carter and B. Ruhstaller, *J. Appl. Phys.* **98**, 124907 (2005).
15. M. Muccini *Nat. Mater.* **5**, 605 (2006).
16. R. Capelli, S. Toffanin, G. Generali, H. Usta, A. Facchetti and M. Muccini *Nat. Mater.* **9**, 496 (2010).
17. Y. Setoguchi and C. Adachi, *J. Appl. Phys.* **108**, 064516 (2010).
18. S. L. M. van Mensfoort, J. Billen, M. Carvelli, S. I. E. Vulto, R. A. J. Janssen and R. Coehoorn, *J. Appl. Phys.* **109**, 064502 (2011).

Summary

Study of photophysical processes in organic light-emitting diodes based on light-emission profile reconstruction

Organic light-emitting diodes (OLEDs) are emerging as a promising option for energy-efficient, flexible light sources. A key factor that needs to be measured and controlled is the shape of the emission profile, i.e. the spatial distribution of the emitting excitons across the active layer thickness. Being able to accurately measure the emission profile makes it possible to understand the fundamental (photo)physical processes involved in the device operation, providing a basis for further improving the efficiency. In order to investigate state-of-the-art devices, containing 10-20 nm thick emitting layers, emission profile measurements should provide nanometer-scale resolution.

In this thesis, a method is presented and applied to **reconstruct the light-emission profile**, with nanometer resolution, from the measurement of wavelength, angle and polarization-dependent electroluminescence spectra. The method is introduced in chapter 2 and it is used to investigate the photophysics of OLEDs. It uses a “fit-profile” approach within which the shape of the profile is constrained by making use of our understanding of the recombination process, while still allowing more freedom than in previous studies. The method is first applied to blue-emitting and orange/red-emitting single-layer polymer-based devices. We show that a 5 nm shift of the emission profile within the emissive layer from the cathode-side to the anode-side by increasing the applied voltage can be resolved, and provide a formalism within which the resolution limits can be analyzed. Subsequently, in chapter 3 the **resolution** is compared to that of a more standard inverse-problem solving approach and analyzed for single-layer, double-layer and multilayer OLEDs. In all cases, the resolution is found to be in the range 1-10 nm.

As a next step, in chapter 4 this method is used to **determine the singlet exciton fraction in OLEDs**. From standard statistical physics considerations a value of 25% is expected. Since in fluorescent materials only singlet excitons can decay radiatively, this fraction limits the maximum achievable efficiency of fluorescent OLEDs. In recent years several studies have indicated that deviations from this value may occur, in particular for polymers. The development of an accurate method for determining the singlet exciton fraction has thus become a topic of intensive discussion and great interest in the literature. We have extended a method presented by Segal *et al.* (2003) by exploiting the possibility to reconstruct the light-emission profile in OLEDs, and show that for the specific case of intensively

studied polyfluorene-based copolymers and for a polyphenylene-vinylene-based polymer the singlet fraction is only 8 – 25%. The light-emission profiles obtained for the polyfluorene-based copolymers were further used to investigate the validity of charge transport and recombination models. This investigation indicates that the mobility is strongly anisotropic.

A study of the **emission profile in more complex double-layer small-molecule-based fluorescent OLEDs** (chapter 5) is shown to provide novel insights in the photophysical processes near organic-organic interfaces. Increasing the thickness of one of the two layers is found to give rise to an emission profile shift from one side of the interface to the other, and to the occurrence of charge-transfer exciton emission. A delicate balance is shown to govern the exciton emission at both sides of the interface and the charge-transfer exciton emission from the interface itself. Since the corresponding three emission spectra are different, controlling the light-emission profile by varying one of the layer thicknesses results in the possibility to tune the emission color.

As a final step, in chapter 6 an analysis is presented of the emission profile in a **multilayer white-emitting OLED**, investigated within the framework of the European project AEVIOM. The light-emission profile obtained provides a measure of the balance between the generation of excitons in the three emissive layers (red, green and blue). It furthermore enables making an accurate assessment of the validity of the charge transport and recombination models developed in the project, and it is shown to provide deeper insight in the role of exciton transfer processes within and between the emitting layers.

The method presented in this thesis is expected to be a fundamental tool for the experimental validation of device models and for designing OLEDs with increased efficiency. The possibility to apply the method as a tool to validate state-of-the-art charge-transport and recombination models (both one-dimensional drift-diffusion models and three-dimensional Monte Carlo models) is discussed in chapter 4 and in the **outlook** of the thesis (chapter 7). The results presented are not only important for OLEDs, but may also be applied to other organic optoelectronic devices containing disordered organic semiconductors, such as light-emitting electrochemical cells and light-emitting field-effect transistors, as discussed in chapter 7.

Samenvatting

Studie van fotofysische processen in organische licht-emitterende diodes door reconstructie van het lichtemissieprofiel

Organische licht-emitterende diodes (OLEDs) zijn in opkomst als een veelbelovende optie voor energie-efficiënte, flexibele lichtbronnen. Een belangrijke factor om te meten en te beheersen is de vorm van het emissieprofiel, dat is de ruimtelijke verdeling van de emitterende excitonen over de actieve laagdikte. Een nauwkeurige bepaling van het emissieprofiel maakt het mogelijk inzicht te krijgen in de fundamentele (foto)fysische processen die een rol spelen in de werking van de diode, hetgeen een basis vormt voor de verdere verbetering van de efficiëntie. Om de meest geavanceerde systemen te kunnen onderzoeken, met emitterende lagen van ongeveer 10 tot 20 nm dik, moet het emissieprofiel gemeten kunnen worden met nanometerschaal resolutie.

In dit proefschrift wordt een methode zowel gepresenteerd als toegepast om, met nanometerresolutie, het **lichtemissieprofiel** te **reconstrueren** uit golf-lengte-, hoek- en polarisatieafhankelijke elektroluminescentiespectra. De methode, geïntroduceerd in hoofdstuk 2, is gebruikt om de fotofysica in OLEDs te onderzoeken. Er is een “fitprofiel” aanpak gebruikt waarin weliswaar de vorm van het profiel beperkt wordt, gebaseerd op onze kennis van het recombinatieproces, maar waarin deze nog steeds meer vrijheid heeft dan in eerdere studies. De methode is eerst toegepast op blauw-emitterende en oranje/rood emitterende op een polymeer gebaseerde enkellaags OLEDs. We laten zien dat bij verhoging van de spanning een 5 nm verschuiving van het emissieprofiel binnen de emitterende laag, vanaf de kathode naar de anode, onderscheiden kan worden en geven een formalisme dat het mogelijk maakt de resolutiegrenzen te analyseren. Vervolgens wordt, in hoofdstuk 3, deze **resolutie** vergeleken met meer gangbare oplossingsmethoden voor inverse problemen en geanalyseerd voor enkellaags, dubbellaags en multilaags OLEDs. In alle gevallen is de resolutie tussen de 1 en 10 nm.

Als volgende stap, in hoofdstuk 4, is deze methode toegepast om de singlet-excitonfractie te bepalen. De veelal verwachte waarde is 25%, uitgaande van de standaard quantum-statistische fysica. Aangezien in fluorescente materialen alleen singletexcitonen stralend kunnen vervallen, beperkt deze fractie de maximale efficiëntie van fluorescente OLEDs. In de afgelopen jaren zijn er verschillende studies geweest die een afwijking van deze waarde aangaven, in het bijzonder voor polymeren. De ontwikkeling van nauwkeurige methoden om de singletfractie te bepalen is dus het onderwerp van een intensieve discussie en grote interesse in

de literatuur. Wij hebben een methode van Segal *et al.* (2003) uitgebreid door gebruik te maken van de mogelijkheid om het lichtemissieprofiel van OLEDs te reconstrueren en laten zien dat voor het specifieke geval van de intensief bestudeerde polyfluoreengebaseerde copolymeren en van een polyfenyleenvinyleengebaseerd polymeer de singletfractie slechts 8-25% is. Voorts zijn de lichtemissieprofielen, verkregen voor de polyfluoreengebaseerde copolymeren, gebruikt om de geldigheid van ladingstransport- en recombinatiemodellen te onderzoeken. Uit dit onderzoek blijkt dat de mobiliteit sterk anisotroop is.

De analyse van de **emissieprofielen in meer complexe op kleine moleculen gebaseerde fluorescente dubbellaags OLEDs** (hoofdstuk 5) heeft geleid tot nieuwe inzichten in de fotofysische processen rondom het grensvlak van twee organische lagen. Het verdikken van één van de twee lagen leidt tot een verschuiving van het emissieprofiel van de ene naar de andere zijde van het grensvlak en tevens tot de vorming van ladingsgescheiden toestanden. Het blijkt dat de excitonemissie aan beide zijden van het grensvlak en de emissie uit de ladingsgescheiden toestanden aan het grensvlak zelf beheerst wordt door een delicaat evenwicht. Aangezien de drie corresponderende emissiespectra verschillend zijn, is het mogelijk de kleur van de emissie af te stemmen door één van de drie laagdiktes te variëren.

Als laatste stap wordt in hoofdstuk 6 een analyse gepresenteerd van het emissieprofiel in een **wit-licht-emitterende multilaags OLED**, onderzocht in het kader van het Europese project AEVIOM. Het lichtemissieprofiel weerspiegelt het evenwicht tussen de vorming van excitonen in de drie emitterende lagen (rood, groen en blauw). Bovendien stelt het ons in staat om de geldigheid van de ladingstransport- en recombinatiemodellen, ontworpen in het project, nauwkeurig te beoordelen en biedt het meer inzicht in de rol van excitonoverdrachtsprocessen binnen en tussen de emitterende lagen.

Naar verwachting zal de methode gepresenteerd in dit proefschrift een fundamenteel instrument vormen voor de experimentele validatie van OLED modellen en voor het ontwerp van efficiëntere OLEDs. De mogelijkheid om de methode toe te passen als instrument om de meest geavanceerde ladingsoverdracht- en recombinatiemodellen (zowel ééndimensionale drift-diffusie modellen als driedimensionale Monte Carlo modellen) wordt besproken in hoofdstuk 4 en in de **voorblik** van het proefschrift (hoofdstuk 7). De gepresenteerde resultaten zijn niet alleen voor OLEDs van belang, maar ook voor andere organische opto-elektronische systemen met wanordelijke organische halfgeleiders, zoals licht-emitterende elektrochemische cellen en licht-emitterende veld-effecttransistoren.

List of publications

1. *Measuring the light emission profile in organic light-emitting diodes with nanometre spatial resolution*,
S. L. M. van Mensfoort, M. Carvelli, M. Megens, D. Wehenkel, M. Bartyzel, H. Greiner, R. A. J. Janssen and R. Coehoorn, *Nature Photonics* **4**, 329 (2010).
2. *Predictive modeling of the current density and radiative recombination in blue polymer-based light-emitting diodes*,
S. L. M. van Mensfoort, J. Billen, M. Carvelli, S. I. E. Vulto, R. A. J. Janssen and R. Coehoorn, *Journal of Applied Physics* **109**, 064502 (2011).
3. *Determination of the exciton singlet-to-triplet ratio in single-layer organic light-emitting diodes*,
M. Carvelli, R. A. J. Janssen and R. Coehoorn, *Physical Review B* **83**, 075203 (2011).
4. *Spatial resolution of methods for measuring the light-emission profile in organic light-emitting diodes*,
M. Carvelli, R. A. J. Janssen and R. Coehoorn, *Journal of Applied Physics* **110**, 084512 (2011).
5. *Exciton formation and light emission near the organic-organic interface in small-molecule based double-layer OLEDs*,
M. Carvelli, A. van Reenen, R. A. J. Janssen, H. P. Löbl and R. Coehoorn, submitted to *Organic Electronics* (2011).

Curriculum vitae



Marco Carvelli was born in Rho (MI), Italy, on August 26, 1983. He spent most of his childhood and youth in Saronno (VA), Italy. After obtaining his high school degree from liceo scientifico “G. B. Grassi” in Saronno (VA) he studied physics engineering at Politecnico di Milano, Italy, with major in nano-optics and photonics. He obtained his bachelor degree in July 2005 with a thesis on *in vivo* absorption and scattering spectroscopy of human tissues, after an internship in the department of physics of Politecnico di Milano. He received his master degree in December 2007; his master thesis project consisted of the manufacturing and development of organic distributed-feedback lasers. The project was carried out in the department of physics of Politecnico di Milano, under the supervision of prof. dr. Guglielmo Lanzani. The main results of that work were published as part of a book chapter in “Ultrafast dynamics and laser action of organic semiconductors”, Z. V. Vardeny ed., Taylor and Francis Group (USA). In January 2008 he moved to Eindhoven, The Netherlands, where he started his PhD research in the group Molecular Materials and Nanosystems, led by prof. dr. ir. René Janssen. He performed his research on the photophysics of organic light-emitting diodes at Philips Research Eindhoven, under the supervision of prof. dr. Reinder Coehoorn. The project was part of the research program of the Dutch Polymer Institute (DPI). The results of that research are discussed in this thesis. Some of these results were presented at national symposia and international conferences in Eindhoven, Bruxelles (Belgium), Winterthur (Switzerland), Ann Arbor (USA), Copenhagen (Denmark), Barcelona (Spain). From February 2008 to February 2011 he collaborated intensively with groups participating in the European 7th framework project AEVIOM. He has been referee for top scientific journals: Nature Photonics, Organic Electronics and Journal of Applied Physics. During his PhD research period he guided one student during his internship and one student during her master thesis project.

Acknowledgements

Aristotle once said “man is by nature a social animal” (Aristotle, *Politics*, ca. 350 B. C.). We are immersed in a specific environment which shapes our lives. This is the reason why I consider it difficult to come up with a complete list of people I shall thank for having helped me through my PhD. I will try.

The first ones to be mentioned are my parents. They are the ones who made it possible for me to have an education, which is a *condicio sine qua non* I could start this adventure in the Netherlands in 2008. *Mi siete sempre stati vicini, addirittura pronti a prendere un aereo poco dopo una telefonata, qualche mese fa. A voi così come ai nonni, che con la costanza delle loro telefonate domenicali mi hanno tenuto compagnia, va un grazie di cuore.*

I am sincerely grateful to my supervisors, Reinder Coehoorn and René Janssen. Reinder, you have really been a mentor for me, someone who taught me to constantly challenge every idea, someone who motivated me to tackle difficulties and definitely improved my precision and rigorousness. It has been a real pleasure to discuss with you about science, politics and economics (among the hundreds of other topics) during these four years. René, as the head of the group Molecular Materials and Nanosystems you could only guide me from a certain distance, nevertheless you have always been able to give the right suggestion at the right moment, with a fresh view on every problem.

I also want to thank Prof. dr. Karl Leo, Prof. dr. Guglielmo Lanzani, dr. Peter Bobbert, Prof. dr. Maria Antonietta Loi and dr. Stefan Meskers for having accepted to be part of my thesis defence committee and for judging my thesis on scientific value. Guglielmo, I think a special acknowledgement goes to you, for having introduced me to the organic semiconductors world back in March 2007, during my master thesis project in Milan.

I shall certainly be thankful also to my colleagues from Philips Research Eindhoven/Aachen, from the Eindhoven University of Technology and all the partners of the AEVIOM consortium and the Dutch Polymer Institute. Thank you for the many discussions we had during our meetings or simply at the SMO-M2N dinners or during the coffee-breaks. In particular I am thankful to Peter Löbl and Ton van den Biggelaar for having fabricated most of the devices we analyzed, and to

Horst Greiner for having developed the optical microcavity model we used.

It is difficult to imagine the past four years without the contributions of Siebe van Mensfoort, Rein de Vries and Harm van Eersel, my PhD colleagues at Philips Research. Siebe, you were finalizing your PhD when I just started mine, nevertheless you found the time to help me and give me suggestions, I really appreciated it. Rein, we have started our PhD almost at the same time, it has been a pleasure to go through such an experience together. Harm, you have started working in our group less than one year ago but your help has been really impressive so far, not only from the scientific point of view but also in solving all sorts of “IT”-problems during the writing of this thesis. Harm is also the person I have to thank for the *Samenvatting* you have just read.

A special mention is deserved by the two students I guided during my PhD and who contributed to part of the work I presented: Alexander van Reenen (chapter 5) and Rossella Porrazzo (chapter 4). Alex, you have been the first student I ever guided but I have to admit that your extreme intelligence made the task much less difficult for me. Rossella, we have been working together for nine months and I will never thank you enough for your dedication and for the optimism you brought into the project.

Coming back to the concept of man as a social animal. Four years far from your friends and family can be quite tough, if you aren't lucky enough to find new friends and build-up a new network you can count on. That is why I would like to thank all the people I encountered along the way during these years. From every continent, from any religion, with any political view. I have learnt so much from all of you. A special mention goes to the little Italy we built-up, year after year, in Nieuwstraat. Nico, you have always been there, since the “Introduction day for international PhD students” almost four years ago. Incredible. Ciccio, Agnese, Ginny, Dani, Peppe, Christian, Rocco, Alberto, Daniel, each of you had a special role in our small family, a warm environment where to spend our evenings after work and our week-ends. Thank you for the laughter and the debates. And then comes Serena. Or first comes Serena. *Sei stata Baricco e De André. Sei stata estati ed invernati. Sei stata, sarai, “decisamente tu”*.

Grazie

Marco